Azimuthal Anisotropy of Strange and Charm Hadrons

Measured in Pb–Pb Collisions at 2.76 TeV

Azimuthale anisotropie van vreemde en charm hadronen

Gemeten in Pb–Pb botsingen bij 2.76 TeV
(met een samenvatting in het Nederlands)

Proefschrift

ter verkrijging van de graad van doctor aan de Universiteit Utrecht op gezag van de rector magnificus, prof.dr. G.J van der Zwaan, ingevolge het besluit van het college voor promoties in het openbaar te verdedigen op donderdag 27 augustus 2015 des ochtends te 10.30 uur

door

Carlos Eugenio Pérez Lara

geboren op 9 juli 1981 te Lima, Peru

Promotor: Prof. dr. T. Peitzmann
Copromotor: Dr. P.G. Kuijer

This research was financially supported by the Netherlands Organisation for Scientific Research (NWO) via the Fundamenteel Onderzoek der Materie (FOM).

Contents

List of Figures

Preface

I started the phD before the first Pb–Pb collisions were registered at ALICE. The framework for the analysis of flow of decaying particles was not there, although studies had been carried out already in the Netherlands. The approach proposed by Paul, my advisor, was to build the framework side to side with another ongoing project: the "flow" package. Few weeks after that, I coupled my new methods to the flow package and went to CERN to work in person with Paul.

What a nice period it was! I was sharing the office with two great officemates Naomi and Marta and working together with Cristian, Pavel, Ilya, Yasuto and Panos in the analysis of K^0_s and Λ v_2. Our early results were presented in QuarkMatter 2011: my first QM.

Later that year, I began a collaboration for the analysis of D^0 v_2 with Chiara, Giacomo, Robert, Kai and Francesco. Together we were not only reconstructing the D^0 particle but also creating the infrastructure to analyse its flow. We diverged in the methodology and implemented several ways to measure flow. All our measurements agreed quite well. We made two publications: one short letter and one long paper comparing the methods and establishing an astonishing result: directly reconstructed open charm particles flow! I presented the work in the ICHEP2012 held in Australia: my first talk. In the same conference, DayaBay and RENO announced the measurement of a large mixing angle θ_{13} 9° and CERN declared the discovery of a new particle at 125 GeV - very compatible with the Higgs.

When I came back, Paul offer me to write a thesis solely on D^0 v_2, but I refused in order to finish the K^0_s and Λ too. Now, thinking about this three years later, I am glad I chose that route because it was a pretty nice experience that help me understand how some colleagues operate. I picked up the K^0_s and Λ v_2 analysis from where it was left and began the computation of systematics. In parallel I was working on more accurate methods to compute these observables. I ended up spending two additional years to pull out the final measurements with the new methods and organise the summary of my results and six other people's results into one single publication. It was a great pleasure to work with those guys: Andrea, Francesco, Ionut, Panos, Redmer, You, ZhongBao and, in the last few months, Alexandru. I did not always agree with some of their methodologies, but this is were the enriched experience comes from.

I am very thankful to the people that make this whole project work and those who accompany me at CERN, Nikhef and UU: Adinda, AlbertoC, AlbertoG, AlbertoJ, Alessandro, Alexandru, Alicia, Alis, Annalisa, Andre, AndreaDa, AndreaDu, AndreaR, Andreas, Angélica, Ante, Antonio, Arturo, Astrid, Betti, Betty, Bruno, CarlosS, Carnita, ChiaraB, ChiaraO, ChiaraZ, Cristian, Christine, Daniel, DavideC, DavideL, Deepa, Dominique, Eugenio, Ed, Eleonora, Emilia, Ermes, Fabrizio, FrancescoN, FrancescoP, Gabriel, Grazia, Geart Jan, Gerardo, GiacomoC, GiacomoO, GiacomoV, Giorgios, Guy, Harry, Hongyan, Ilya, Ionut, Isabel, Javier, Jhon, Jorge, Katya, Karina, Leo, Luis, Lydia, Marek, Marco, Mariella, Mario, Marta, Martijn, Merijn, Michael, Michiel, Michelle, Mike, Mikolaj, Misha, Nadja, Naghmeh, Naomi, Paul, Panos, Pepe, Peter, Pili, Pilarín, Raoul, Raimond, Ramon, Redmer, René, Robert, Roberta, Rose, Rosella, Sandro, Sarah, Sumit, Thomas, Ulla, Yasuto, Yolanda, Yota, You, Verónica, Virginia, and Zaida.

I want to thank also the reading committee of this manuscript: Nicolo de Groot, Panos Christakoglou, Paul Kooijman, Paul Kuijer, Raimond Snellings, Stan Bentvelsen and Thomas Peitzman for the extenuating work of reviewing and polishing this document. Special thanks to Marco Van Leeuwen and Paul Kuijer for translating the summary into Dutch.

I want to thank Alis and Naghmeh for the valuable help during the preparation of the defence.

Finally, I want thank the love of my life: Alicia, Bruno and Verónica who have encourage me during the whole PhD and still do. They have the magic to do wonderful things with me with just one smile.

Introduction

1

Apart from gravitation, most of the phenomena found in nature can be explained by the Standard Model. The *Standard Model* (SM) combines the electromagnetic, weak and strong nuclear interactions into one single description. The fundamental fields involved in the SM are 18 - twelve spin 1/2 fermions and six bosons whose main properties are summarised in table 1.1. The fermions can be divided into quarks (the top six in the table) and leptons (the middle six). The bosons (at the bottom of the table) are the mediators of the three fundamental forces of the Standard Model [2]. Charged fields interact electromagnetically via photon γ exchange. Fields which present weak isospin interact weakly through $W^{\pm}$ and Z exchange. Fields with colour charge interact via the strong force by the exchange of a gluon g.

The physics of strong interactions is described by the field theory called *Quantum Chromodynamics* (QCD). Its mathematical foundation consists of a

Field	Mass (MeV/c^2)	Spin	Charge	$(I,I_3)_{\text{weak}}$	Colour states
d	$4.1 - 5.8$	1/2	$-1/3$	$(1/2, -1/2)$	3
u	$1.7 - 3.3$	1/2	$+2/3$	$(1/2, +1/2)$	3
s	$80 - 130$	1/2	$-1/3$	$(1/2, -1/2)$	3
c	$1200 - 1340$	1/2	$+2/3$	$(1/2, +1/2)$	3
b	$4100 - 4400$	1/2	$-1/3$	$(1/2, -1/2)$	3
t	172000	1/2	$+2/3$	$(1/2, +1/2)$	3
e^-	0.511	1/2	-1	$(1/2, -1/2)$	0
ν_e	< 0.000003	1/2	0	$(1/2, +1/2)$	0
μ^-	105.66	1/2	-1	$(1/2, -1/2)$	0
ν_μ	< 0.19	1/2	0	$(1/2, +1/2)$	0
τ^-	1777	1/2	-1	$(1/2, -1/2)$	0
ν_τ	< 18.2	1/2	0	$(1/2, +1/2)$	0
γ	0	1	0	(0, 0)	0
$W^{\pm}$	38419	1	± 1	$(1, \pm 1)$	0
Z	91188	1	0	(1, 0)	0
g	0	1	0	(0, 0)	8
H	125000	0	0	$(1/2, -1/2)$	0

Table 1.1 Field of the minimal Standard Model. The first group correspond to quarks; the second, to leptons, and the last one, to bosonic fields. Electric charges are given in units of the positron charge. Extracted from [1].

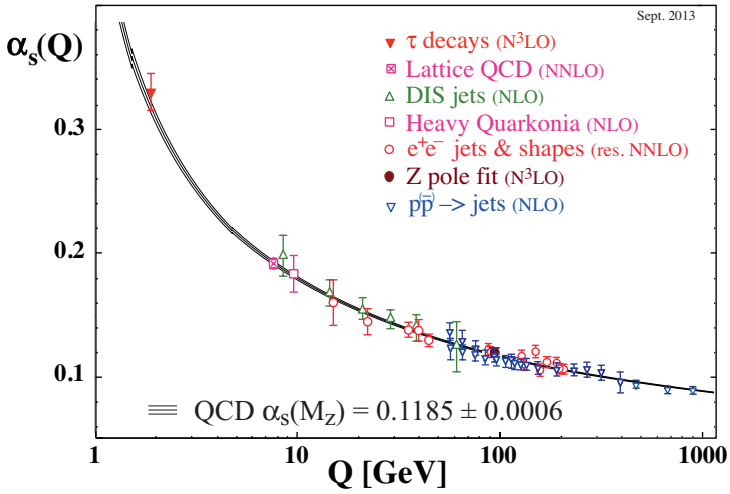

Figure 1.1 The running coupling $\alpha_s$for the strong interaction and its dependence on energy scale Q. The measurements are a collection from many experiments using different techniques at distinct energies. The continuous line is the extrapolation using QCD theory and the world average procedure indicated in [3].

non-abelian Yang-Mills theory characterised by an internal symmetry whose representation corresponds to that of a SU(3) group.

In a QCD interaction the strength of the force, quantified by the strong coupling α_s, decreases with the momentum transferred Q^2 between the interacting fields. Processes with large Q^2, also called hard processes, can be computed by perturbation theory in the same fashion as for the electromagnetic and weak forces. In this respect, the contributions to the interaction cross section between the fields can be computed progressively order by order. This property of QCD is called asymptotic freedom, since in the limit of extremely large Q^2, or equivalently short distances, the strength of QCD interactions is very small. Figure 1.1 shows α_s measured in several experiments at different energies together with the respective perturbative procedure used in the extraction of α_s.

The situation is very different for a soft process (low Q^2) since the large α_s prohibits a perturbative treatment. In those regimes, α_s becomes so large that quarks are effectively bound into colourless quantum states: hadrons[1]. This property is called confinement. At such regimes a description using LatticeQCD [4, 5] is usually employed. The latter is a non-perturbative imple-

[1]Colorless states can be formed by either a quark and and antiquark, called mesons, or three quarks (three antiquarks) called baryons (antibaryons).

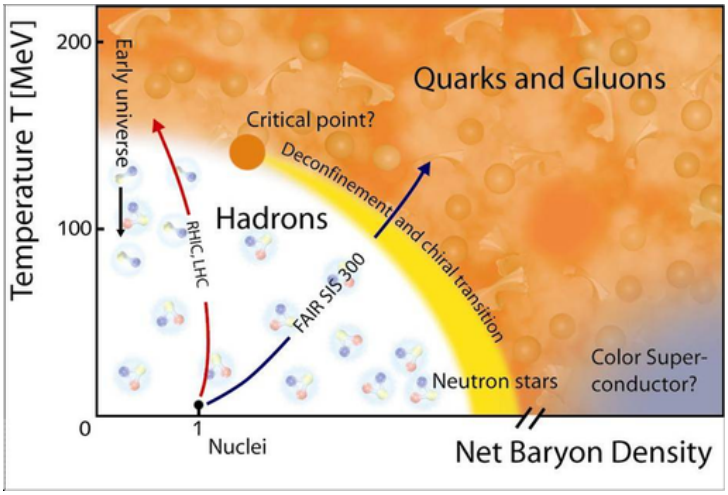

Figure 1.2 Phase diagram of QCD matter showing the QCD phases that occur in nature. The left-most arrow corresponds to path taken in the cosmological evolution of the universe. The red and blue arrows point towards systems made in current and future collider experiments. Figure extracted from [6]

mentation of QCD field theory using a discretisation of space-time aimed to account for the fact that perturbation techniques can not be applied.

An extension of the theory of thermodynamics to nuclear matter has proven to be useful in understanding the nuclear reactions inside stars [7]. Figure 1.2 shows the thermodynamical phase diagram of QCD matter in terms of temperature and net baryon density. In this diagram, normal nuclear matter, which is formed by hadrons interacting mainly via the weak force, is located at almost zero temperature and with a net baryon density of one. As we move along the horizontal axis, the density of quarks and antiquarks vary and so does the net baryon density. Neutron stars are formed at $\kappa T = 0$ with a density in the range of 3-10 times that of nuclei. When the system is subject to an increase of temperature or density, baryons and mesons would ultimately melt into a phase of deconfined QCD matter, where quarks and gluons are not bound into colourless states, but rather move freely.

1.1 STUDYING QCD WITH HEAVY ION COLLISIONS

The study of QCD matter under extreme conditions of temperature and pressure is the main aim of Heavy Ion Collisions (HIC). A wide range of the phase diagram shown in figure 1.2 can be explored in a systematic and controlled way through these kind of collisions. Lattice calculations predict that in those

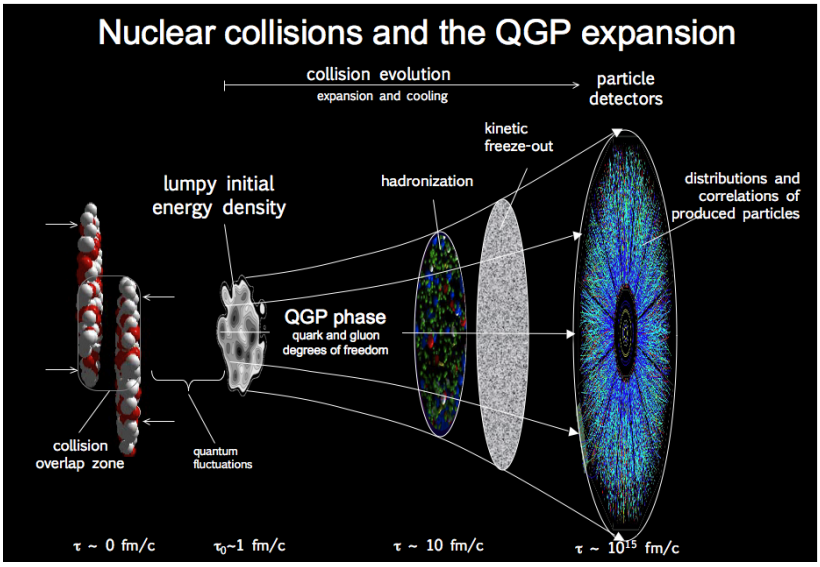

Figure 1.3 Evolution of the matter created in nuclear collisions.

regimes the energy density produced would melt nuclear matter into a phase where quarks and gluons are free [8, 9], followed by the approximate restoration of chiral symmetry.

Previous to the Large Hadron Collider (LHC) era, experiments at the Relativistic Heavy Ion Collider (RHIC) found that the system produced by colliding Au ions at $\sqrt{s_{\mathrm{NN}}} = 200$ GeV is in a state of highly interacting matter which resembles that of a plasma. In this initial state, called Quark Gluon Plasma (QGP), quarks and gluons would move freely over a volume of around 10 fm^3. Figure 1.3 shows a representation of the time evolution of the system created in a heavy ion collision. Shortly after the collision, the system reaches a state of thermal equilibrium, then rapidly expands and cools down from temperatures as high as $\sim$ 500 MeV for RHIC top energies (and much hotter at LHC) towards $\sim$ 170 MeV when hadronisation (or chemical freeze-out) takes place. At this stage the system is composed of hadrons interacting in a state that resembles that of a gas. As the system expands, the mean free path increases leading eventually to a state where hadrons do no interact effectively anymore. At this point, usually referred to as kinematic freeze-out, the final momentum of hadrons is established, after which the hadrons stream free towards the detectors.

Several analyses at CERN and BNL have taught us many aspects of the dynamics of QCD. The evolution of the system can be studied by analysis

of the particles escaping the fireball and being recorded by the detectors. In HIC, each particle species - either photons, electrons, muons or hadrons - and the correlation among them provide different information of the system evolution. Direct photons and lepton pairs, since they do not suffer colour interaction, are more sensitive to the pre-equilibrium and thermalisation of the system. They thus can be connected to the temperature of the emitting source. Jets, group of strongly collimated hadrons, produced by the hard scattering of quarks and gluons are generated in the initial state. By coupling themselves to the medium, they provide important information about its properties. In particular, highly penetrating jets with $p_{\mathrm{T}} > 10$ GeV experience a significant modification in their p_{T} spectrum, when compared to the one produced in pp collisions, due to energy loss in the medium. The nuclear modification factor, also called R_{AA}, quantifies this effect. This factor is also used to quantify the medium modification of the single particle spectra. R_{AA} is defined as the ratio between the p_{T} spectra measured in heavy-ion collisions to the p_{T} spectra from proton–proton collisions scaled by the nuclear overlap function $\langle T_{\mathrm{AA}} \rangle$, according to Eq 1.1.

$$R_{\mathrm{AA}} = \frac{1}{\langle T_{\mathrm{AA}} \rangle} \frac{dN_{\mathrm{AA}}/dp_{\mathrm{T}}}{d\sigma/dp_{\mathrm{T}}}. \tag{1.1}$$

If the particles produced in Pb–Pb collisions result from an incoherent superposition of nucleon-nucleon reactions with no medium effect, then R_{AA} is one by definition. It is found, however, that this is not the case. Particle production in heavy ions is suppressed ($R_{\mathrm{AA}} < 1$) or enhanced ($R_{\mathrm{AA}} > 1$) depending on transverse momentum and differently for every species. The suppression and enhancement can be attributed to a combination of collisional and radiative in-medium energy loss of the partons before hadronisation.

Furthermore, the observation of yields of hidden charmed states, like J/Ψ or Ψ', relative to that of the Υ allow for the study of the deconfined state and colour screening. The width of light vector mesons, like ϕ, ρ and ω, is predicted to be sensitive to chiral restoration in the QGP which reduces their constituent quark masses.

Finally, correlations between particles provide deep insight into the properties of the QGP and its evolution. In particular, the azimuthal correlation of produced particles probe the degree of spatial asymmetry in the formed medium and the strength of its coupling. The latter is related to the mean free path in the interaction between constituents.

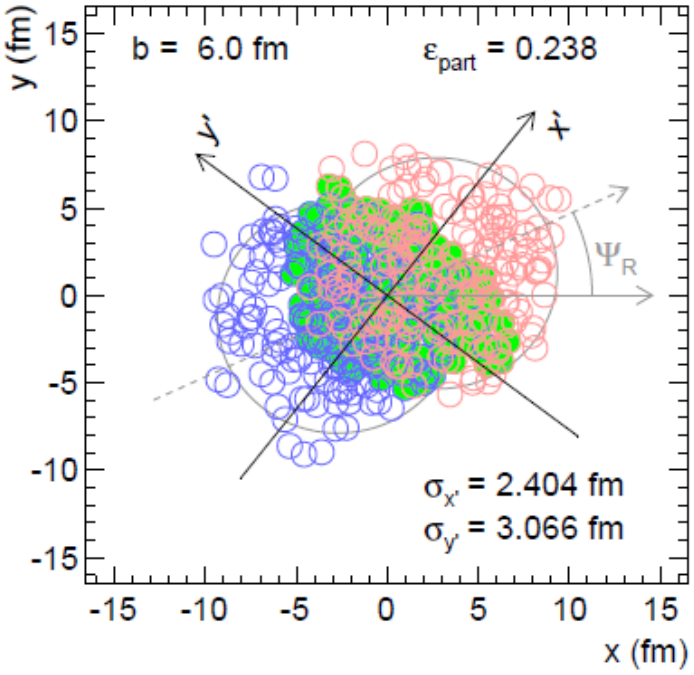

Figure 1.4 Simulation of a non-central heavy-ion collision with impact parameter $b = 6$ fm using the Glauber model. The nucleons that participate in inelastic interactions are marked with filled circles. The x and y coordinates represent the laboratory frame. The participant eccentricity ϵ_{part} and the standard deviations of the participant spatial distribution $\sigma_{x'}$ and $\sigma_{y'}$ are also shown. The angle Ψ_{R} denotes the orientation of the reaction plane angle. Extracted from [10].

1.2 ANISTROPIC FLOW V_N

The particles produced in non-central heavy-ion collisions present an anisotropy in their momentum distribution. This phenomenon is the result of the interactions in the anisotropic shape of the matter produced in such collisions. The anisotropy can be quantified by performing an azimuthal expansion of the momentum distribution of particles around the *reaction plane angle* (Ψ_{RP})[2]. The reaction plane is defined by the vector that connects the centres of the colliding nuclei and the beam direction, whereas the reaction plane angle is measured in the transverse plane as the direction of the line formed by the intersection of the reaction plane and the transverse plane.

[2]In many references the reaction plane "angle" is referred to as just the reaction plane.

In such context, it was shown [11] that a Fourier basis has very useful symmetries which allow for an easy connection between theory and measurements. The Fourier expansion of the azimuthal distribution of momenta around Ψ_{RP} is

$$E\frac{\mathrm{d}^3N}{\mathrm{d}p^3} = \frac{1}{2\pi}\frac{\mathrm{d}^2N}{p_\mathrm{T}\,\mathrm{d}p_\mathrm{T}\,\mathrm{d}y}(1+2\sum_{n=1}^{\infty} v_n \cos n(\varphi - \Psi_{RP})), \tag{1.2}$$

where the odd (sine) terms of the Fourier expansion vanish by symmetry [11] and the factor "two" multiplying the v_n coefficient allows for a direct connection between v_2 and the p_x^2 and p_y^2 asymmetry studied previously [12]. The v_n coefficient are usually referred to as the n-th flow harmonic coefficient.

Due to the finite extension of the colliding nuclei, the resulting medium has an inhomogeneous density profile. The complex shape resulting from a heavy-ion collision is usually analysed using many angles of symmetry. Figure 1.4 shows a sketch of the geometry of a system produced by a heavy-ion collision at the beginning of thermalisation. The reaction plane angle, which is fixed by the collision geometry, is also drawn in the figure. The filled circles represent those nucleons undergoing inelastic collisions (also called participants). The x' and y' lines are along the minor and major axis describing the elliptic ($n = 2$) symmetry of the formed medium: x' being the principal axis. The $x' - z$ plane is called *second-order symmetry plane*[3]. Symmetries of higher order can be found in the medium also. The orientation of the principal axis for all these symmetry planes in the laboratory frame are usually referred to as *symmetry plane angles*.

Experimentally the principal axis of symmetry can be measured[4] from the azimuthal anisotropy of particles escaping the system. The angles of symmetry formed by the azimuthal distribution of final state particles are called *flow angles* (Ψ_n).

For instance, for the determination of v_2 (elliptic coefficient) an expansion around the second order flow angle Ψ_2 is used in equation 1.2 instead of the reaction plane. The v_n coefficient can be extracted by using the orthonormality of the Fourier basis

$$v_2 = \langle\langle \cos 2\,(\varphi - \Psi_2)\rangle\rangle = \langle\langle \mathrm{e}^{2i(\varphi - \Psi_2)}\rangle\rangle, \tag{1.3}$$

where φ represents the azimuthal angle of the particle under study and the average is taken over those particles and over events. The coefficient can

[3] In literature this plane is often called *participant plane* or *event plane* since the second order symmetry is the predominant one in non-central collisions.

[4] A biunivocal relation between the orientation of the symmetry plane angle of the initial state geometry and the flow angle of the final momentum distribution of particles is implied. Current studies [13] are testing the limits of such assumption.

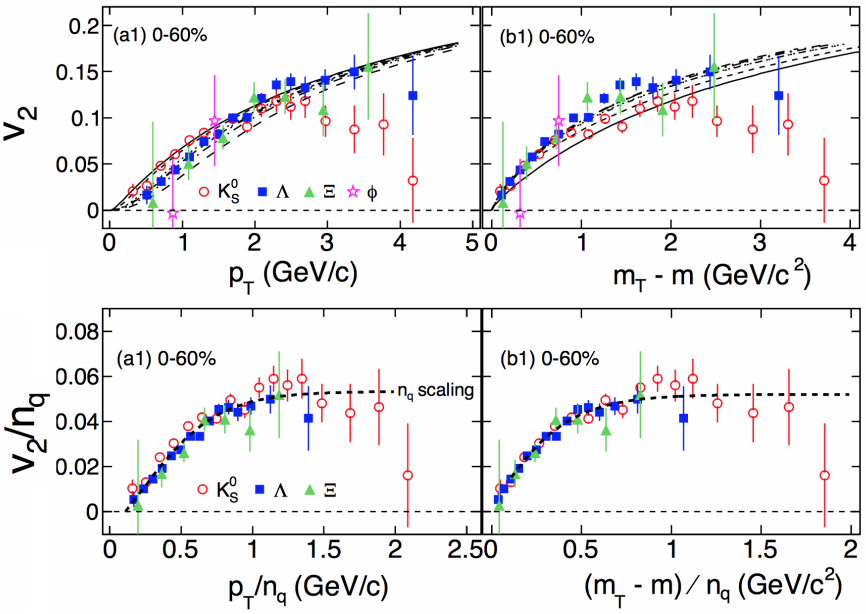

Figure 1.5 Strange hadron v_2 measured in Au+Au collisions at $\sqrt{s_{NN}} = 200$ GeV by the STAR collaboration. Extracted from [15]

also be constructed using complex notation since the imaginary term (sine) vanishes by symmetry [14]. The Argand notation is the nomenclature usually found in literature and therefore adopted in this thesis.

Although the v_n coefficients were meant to study particles that have enough time to interact with the expanding medium (setting a cut off p_T of the order of a couple of GeV/c for LHC energies), these studies are naturally extended to high transverse momentum, where the v_n of identified particles become sensitive to the path length dependence of their energy loss.

1.3 PREVIOUS RESULTS ON THIS SUBJECT

The anisotropic parameter v_2 for strange resonances and cascades in Au+Au collisions at $\sqrt{s_{NN}} = 200$ GeV was recently reported by the STAR experiment [15]. Figure 1.5 shows the differential v_2 for K^0_s, Λ, Ξ and ϕ together with a proposed universal scaling for strange and light quarks. The accuracy for K^0_s and Λ allows for a clear separation in the differential v_2 (top left panel), which

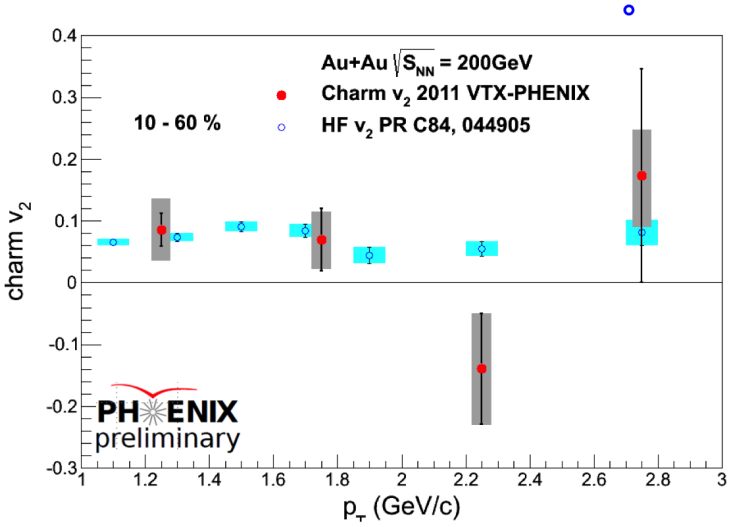

Figure 1.6 v_2 of heavy flavour electrons and open charm measured in Au+Au collisions at $\sqrt{s_{NN}} = 200$ GeV by the PHENIX collaboration. Extracted from [16]

seems to scale[5] rather well when the number of constituent quarks for each hadron is considered (bottom-right panel). However, the limited p_T range and broad centrality selection only allow for a marginal interpretation of the role of strange quarks in the dynamical expansion of the QGP.

On the charm sector, many studies of the azimuthal anisotropy produced in HIC have also been performed. Figure 1.6 shows the anisotropic parameter v_2 for electrons from heavy flavour decays and reconstructed open charm mesons in Au+Au collisions at $\sqrt{s_{NN}} = 200$ GeV. The results show a non-zero charm v_2 for non-photonic electrons whose origin is mostly from heavy flavour weak decays. The recent results from direct reconstruction of open charm mesons is at most marginal, but still compatible with that of heavy flavour electrons.

The present document contains two flow analysis:

The first part is the analysis of v_2 of K^0_s and Λ where I was the main analyser: implemented the analysis algorithms, did the particle reconstruction and performed the Monte Carlo and systematic errors studies. The observables reported here correspond to those measured in Pb–Pb collisions at $\sqrt{s_{NN}} = 2.76$ TeV - more than one order of magnitude higher that those recorded at RHIC - using the data collected during the first long run period of the LHC. These

[5] the scalling and all other features of the RHIC data will be discuss in chapter 5 where the results of this thesis will be presented.

measurements will be compared to the current state of the art hydrodynamic models in narrow centrality classes and fine p_{T} bins. Moreover, the extension in p_{T} up to 12 GeV/c not only allows for a rigorous test of the universal scaling proposed at RHIC, but also provides insight into mechanism of path length dependence in the energy loss of strange quarks traveling through the medium. Furthermore, the new ways to compare the anisotropic parameter v_2 using three different estimates bring a fresh perspective on the effect of flow fluctuations in the measurement of v_2.

The second analysis corresponds to the v_2 of D^0 where I performed the v_2 measurement using two different methods and published them together with an independent analysis done by colleagues using a third method. I was in charge of the systematic uncertainties related specifically to these two methods and the ones common to all of the methods. The new measurements on v_2 of D^0 fully reconstructed in ALICE extend the measurements of charm v_2 up to a much higher transverse momentum with unprecedented accuracy. These results will be compared to models which describe the transport of heavy quarks and have successfully described the data at high p_{T} in both RHIC and LHC energies.

The results of my analyses where published in three refereed journals and were highlighted for public outreach in several editions of the CERN courier. In addition, I worked in the quality assurance inspection of the multiplicity and event plane angle measured with different detectors during the first Pb–Pb collisions and contributed to the analysis of the D^{*+} spectra measured in pp collisions at 7 TeV by performing Monte Carlo fits to the distribution of several topological variables used in its reconstruction. These results were published also, but they are not included in the present manuscript.

The structure of this document is the following: Chapter 2 contains a brief description of the ALICE sub-detectors relevant for this analysis. In chapter 3, the approach to v_n of decaying particles by multi-particle correlations and reconstruction of the Q_{n} vectors is discussed. Chapter 4 encloses the description of the reconstruction of candidates and their v_2. Chapter 5 is where the measurements are presented and discussed. Final remarks will be given in chapter 6. Enjoy it!

The ALICE detector

2

The *Large Hadron Collider* (LHC) is the largest and most powerful synchrotron in the world at the time of the present study. It is designed to accelerate protons up to an energy in the centre of mass of 14 TeV and lead ions up to 5.5 *A* TeV. With a 27 km circumference spanned in both Swiss and French territory, the LHC collides particles at four different locations which correspond to the four particle detectors it hosts: ATLAS, CMS, LHCb and ALICE.

A Large Ion Collider Experiment (ALICE) has been designed specifically to study heavy–ions reactions, although it also has an ambitious pp program.

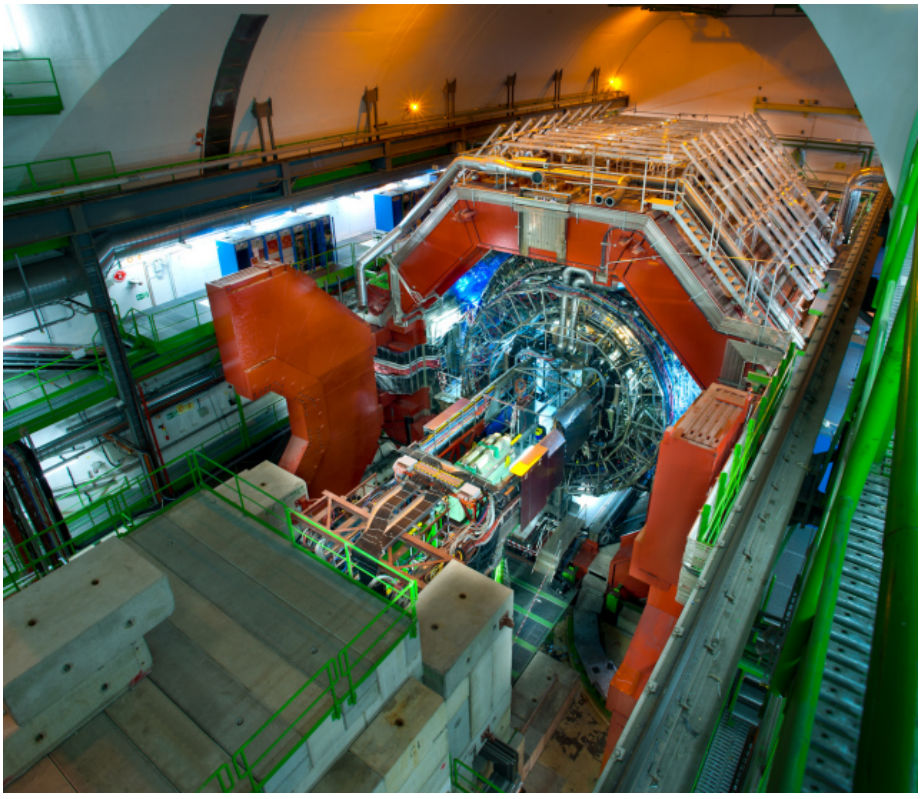

Figure 2.1 Photograph of the ALICE detector in the LHC ring. The cavern where it is located is around 50 m below surface in Saint-Genis Pouilly, France.

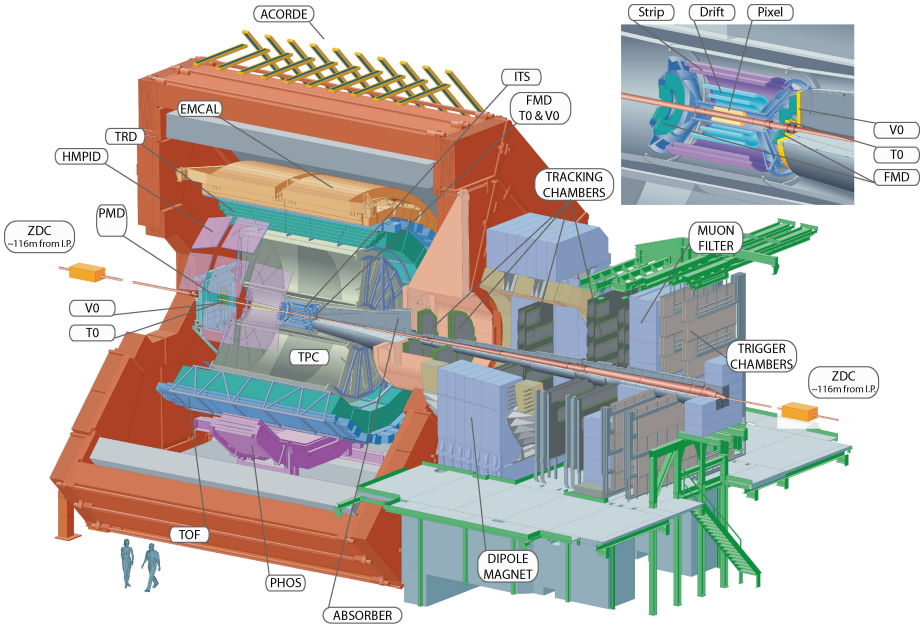

Figure 2.2 Drawing of the ALICE detector showing many of its subdetectors. The silhouette of two people are shown for scaling purposes.

Its main advantages with respect to other LHC detectors are in low momentum reconstruction and particle identification. The detector allows for distinct physics studies going from particle multiplicity to reconstruction of complex structures like decays, showers or jets. Figure 2.1 shows a photograph of the ALICE detector taken during the final preparations before its first operations in late 2009. Although the picture was taken for outreach communication, one can still see the complexity of the sub-detectors as well as the beauty of its superstructure. On the bottom left corner one can see the blocks of concrete which provide extra shielding for the forward spectrometer when the beams are present. Those blocks work also as a deck for visitors when the access to the experiment is open for public.

ALICE's architecture can be classified in three parts according to their pseudo-rapidity coverage: a central, a mid–forward and a very-forward detector.

At mid–rapidity $|\eta| \leq 0.8$, ALICE has full azimuthal coverage, high resolution tracking and particle identification capabilities. This allows for precise measurements of multiplicity density, p_{T}-spectra of charged and neutral par-

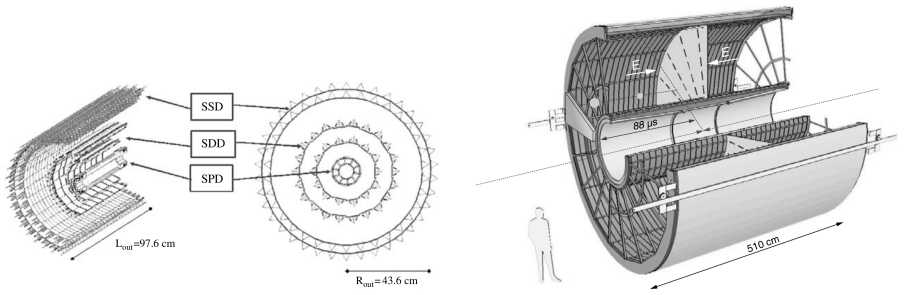

Figure 2.3 Drawings of the (left) ITS detectors and (right) TPC detector; For ITS the dimensions are shown in centimetres; for TPC, the silhouette of a person is drawn for scale purposes.

ticles, jet reconstruction and composition, multi-particle correlations, among others.

In $2 \leq \eta \leq 4$, ALICE features a high resolution multiplicity detector and a muon spectrometer for heavy quarkonia reconstruction. At approximately the same pseudo-rapidities, two scintillator systems are installed one on each side of the interaction point in order to provide a trigger, measure centrality and estimate beam–gas contamination.

Around 150 meters from the interaction point ALICE has a calorimeter designed to measure the energy of the spectator particles from the collision. This detector not only contributes to the determination of centrality, but also allows for measurements of electromagnetic dissociation and flow.

Figure 2.2 shows a drawing of the ALICE detector and many of its sub–detectors. In the present document, I will provide details on the detectors used in this analysis. However, for a complete description of these detectors the reader should refer to [17].

2.1 CENTRAL DETECTORS

At the core of ALICE there is a large 7800-ton solenoidal magnet [17] (L3-magnet), whose yoke is painted in red (see figures 2.1 and 2.2). This device develops a nominal field of 0.5 T parallel to the beam direction with a homogeneity within 2% inside its active volume. Its super-structure extends over 700 m^3 and it features switchable orientation of its magnetic field, a feature very useful when testing e.g. the alignment of the tracking detectors.

The central tracking detectors are mounted inside the L3-magnet and are designed to provide high-resolution momentum measurement, strong two-track separation power, precise vertex determination and particle identifica-

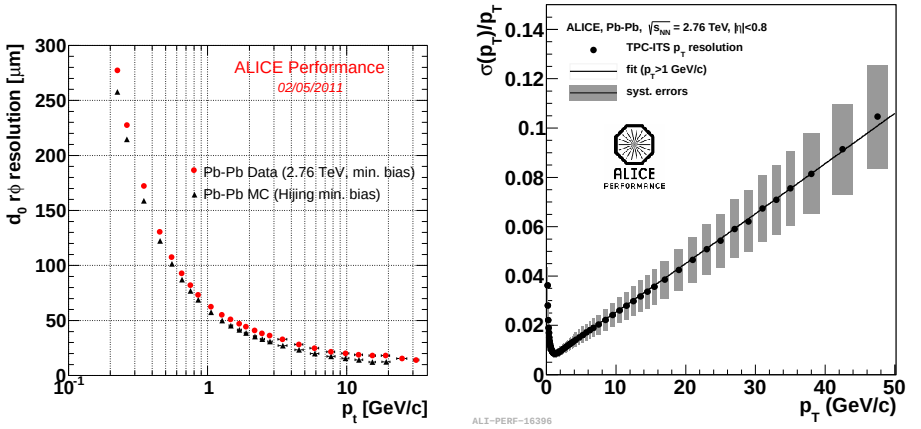

Figure 2.4 Left: Impact parameter resolution of tracks reconstructed with the ITS. Right: Momentum resolution of tracks reconstructed with the combined information of TPC and ITS detectors.

tion. In terms of event selection, the fast response of its inner layers provide also a minimum bias trigger, while its tracking capabilities allow for the trigger of event with more specific characteristics in a refined trigger procedure called High-Level Trigger [18].

2.2 THE INNER TRACKING SYSTEM

The track density in the range of $3.5 \leq r \leq 45$ cm from the interaction point is expected to go from 50 down to 1 particles per cm^2. The *Inner Tracking System* (ITS) has been designed to function in these extreme density conditions. The system consists of six layers of silicon detectors with different technologies and spatial coverage. The first two layers are pixel detectors, the next two are drift detectors and the last two are strip detectors. Their sensitive areas are located at r = 3.9, 7.6, 15.0, 23.9, 38.0 and 43.0 cm, respectively, and provide full azimuthal coverage. The maximum pseudo-rapidity coverage goes from $|\eta| < 2.0$ in the innermost layer to $|\eta| < 0.9$ in the outermost layer. The left side of figure 2.3 shows the schematics of the ITS.

The detector material thickness strongly influences the momentum resolution below 3 GeV/c. The ITS has been engineered to amount to less than 10% of a radiation length X_0 [19]. In order to resolve accurately momenta above 3 GeV/c other tracking detectors are used in conjunction with the ITS.

The spatial precision in the direction of the azimuthal angle r$\Delta\varphi$ is well below 50 μm in all the ITS and 12 μm for the pixel layers [20]. The precision of the inner layers allows for a fast estimation of the *primary vertex* by means of a

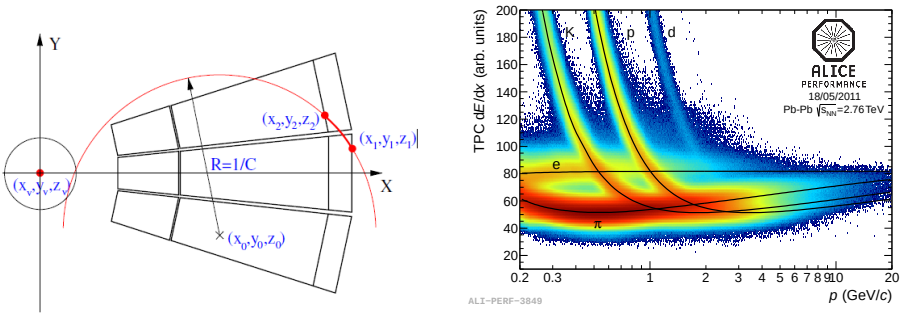

Figure 2.5 Left: First step in *seeding* of primary tracks; Right: Stopping power as function of momentum for tracks measured at the TPC.

linear interpolation of tracklets (pseudo-tracks constructed only with the two first layers of the ITS). This approximate vertex is used as a starting point for the tracking algorithm in the central barrel as will be discussed below. After the tracking is done, the primary vertex is recalculated using the information from the tracks and therefore maximising the resolving power. The resolution in the vertex determination is therefore more accurate for high multiplicity events reaching down to 5 μm. The spatial precision also allows for high resolution in the *impact parameter* of the tracks at the primary vertex, making the measurement of heavy-flavoured hadrons possible. Figure 2.4 shows the detector performance during the first Pb–Pb data taking in 2010. A resolution below 100 μm in the impact parameter of primary tracks is achievable even for transverse momenta below 1 GeV/c.

In addition, the last four layers of the ITS provide a measurement of the specific energy loss in the detector. Although this feature could be used for particle identification in the non-relativistic region, when tracks are crossing at least two of these layers, for the present analysis this information was not used because an equal or more accurate measurement can be achieved from measurements in the outer detectors.

2.3 THE TIME PROJECTION CHAMBER

The *Time Projection Chamber* (TPC) is the main tracking detector at mid-rapidity. Its cylindrical cage is filled with 90 m^3 of Ne/CO2/N2 (90/10/5) gas which was chosen due to its short drift time, low diffusion length, large radiation length, and high stability. Spatially it covers a radius from 85 cm to 250 cm and has an axial coverage of 500 cm ($\pm$250 cm). It also covers full azimuth through eighteen trapezoidal sectors. As the track density is expected to vary with radial distance from the interaction point, each sector is divided radially

into two readout chambers. The inner one covers a third of the total radial coverage and has very dense readout configuration, while the outer chamber has smaller pad density. The cage is separated into two regions of rapidity by a central membrane at $z = 0$ in order to decrease its total drift time and the resulting dead time [21]. The right side of figure 2.3 shows a 3D–view of the TPC and its geometrical segmentation.

Due to its spatial resolution and its low material budget (about 3.5% X_0), it provides adequate *transverse momentum resolution* for an accurate reconstruction of low momentum particles. The right side of figure 2.4 shows the p_T resolution of tracks reconstructed using ITS and TPC altogether. At $p_T < 1$ GeV/c, the resolution is driven by multiple scattering, while at higher p_T, the resolution scales linearly with the transverse momentum. The p_T resolution reaches $\sim 0.7\%$ for particles with p_T around 0.5 GeV/c. At 2 GeV/c the resolution is still around 1%, while at 20 GeV/c, it is still less than 5%.

The *track finding* procedure which involves both ITS and TPC is performed using two steps: a) track seeding and b) tracking following.

The *track seeding* identifies a potential track and provides a rough estimate of its direction. Two different strategies are followed. For *primary tracks*, it starts with the SPD-based primary vertex and two outer TPC-clusters with a large separation between the two - by about 20 rows. The three points constrain a circumference - see figure 2.5 (left) - which is used in a procedure to attach clusters along this path and estimate the robustness of the potential track [22]. For *secondary tracks*, the strategy is somewhat different and involves two algorithms depending on the transverse momentum of the candidate track, see [22] for a detailed explanation.

The *track following* uses a Kalman filter technique [23] with three iterative operations. It starts with clusters reconstructed in the outermost region of the TPC and moves towards the direction of the primary vertex through a sequential scanning of clusters using the trajectory obtained during track seeding. Effects of the material budget on the particle' s trajectory are taken into account during this procedure. Once the innermost layer of the TPC is reached, the found clusters are fit to a helix and the properties of this track are stored and tagged as *tpc-only tracks*. The last cluster found is used as seed for a similar procedure done in the ITS. The next iterative operation uses the innermost cluster and moves towards the outermost one. A third and final operation starts from the outermost cluster and goes inwards. The associated clusters are reassessed during the whole three-step-procedure based on their deviation from the most recent estimation of the track. The tracks resulting from this procedure are called *global tracks*.

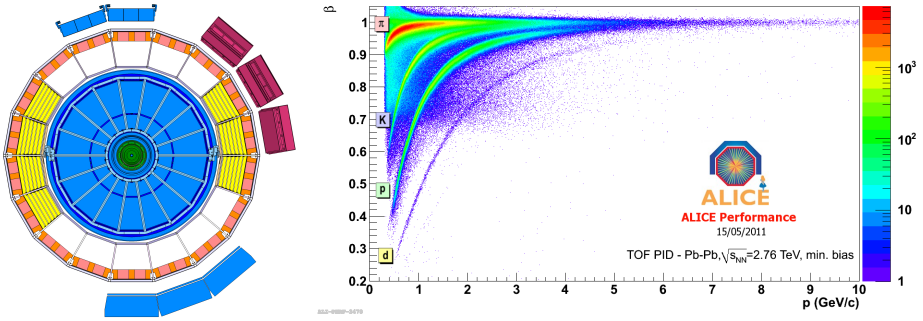

Figure 2.6 Left: Cross section of the ALICE central barrel detectors installed before the first Pb–Pb run; Right: Velocity as function of momentum for particles measured with the TOF.

The detector features a high efficiency in track reconstruction (above 95% for momenta higher than 0.8 GeV/c) keeping the rate of fake tracks to less than 2% even in the most central Pb–Pb collisions. However, due to dead zones which cover about 10% of the total azimuthal acceptance, the overall efficiency with respect to generated particles in full acceptance diminishes down to around 90% for particles with momentum higher than 0.8 GeV/c when tracking is performed using the TPC exclusively [21].

In addition to its highly efficient tracking features, the TPC provides a measurement of the specific energy loss dE/dx of particles traversing its fiducial volume. The right side of figure 2.5 shows a two dimensional distribution of global tracks in terms of the dE/dx (y-axis) and the particle momentum (x-axis). The black lines are the curves expected from a parametrisation of the Bethe-Bloch [3] equation.

Below $p < 0.5$ GeV/c, there is at least a 4σ separation between $K^{\pm}$ and $\pi^{\pm}$, and below $p < 1.0$ GeV/c, protons can be separated from other species.

For relativistic particles, we can profit from the relativistic rise - when the stopping power rises with the $\log \beta\gamma$ - to statistically separate particles up to few tens of GeV/c.

At intermediate p_T (up to 4 GeV/c), where the minimum ionisation limit prohibits a clear separation of species, other detectors can be used. These detectors are located past the TPC and provide complementary (and partially redundant) particle identification in this p_T region.

2.4 THE TIME OF FLIGHT DETECTOR

The *Time Of Flight* (TOF) detector is essential for extending the particle identification to a few GeV/c. This detector consists of an array of Multi-gap

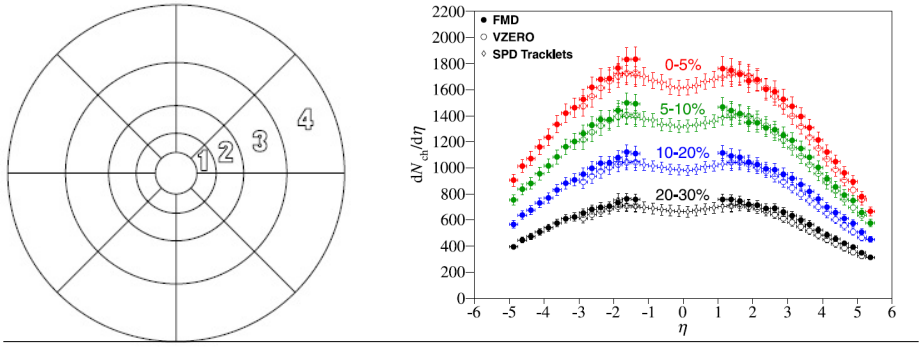

Figure 2.7 Left: Schematics of the VZERO-A detector. Right: Pseudo-rapidity distribution of charged particle multiplicity as measured with several forward detectors including the VZERO.

Resistive Plate Chambers (MRPC) with full azimuthal coverage. Its fiducial volume extends from 370 cm to 399 cm in radius and covers a pseudo-rapidity range of ± 0.9 units. It is segmented in 90 modules: 5 segments in the z direction and 18 segments in azimuth. It features a small material budget which translates to 30% X_0. Three central modules were not installed before the 2010 and 2011 data taking. Figure 2.6 (left) shows a cross section of the central barrel detectors installed for the first Pb–Pb run in 2010. From inside to outside, one can see the ITS in green, the TPC in blue and the TOF detector in light red and covering the full azimuth.

The time resolution of each module is 40 ps with high efficiency [24]. Its efficiency in particle identification depends on both the species and the multiplicity of the overall event. The right side of figure 2.6 shows a two dimensional distribution of global tracks in terms of the measured velocity β (y-axis) and the particle momentum (x-axis). For Kaons in the range from 0.5 to 3 GeV/c, the efficiency goes from 100% in most-peripheral events down to 80% in the most central ones. The contamination from other species is below 5% for a 3σ deviation from the expected time in this p_T range, see [24] for more details.

2.5 THE VZERO SYSTEM

The VZERO system (labelled as Vo in figure 2.2) consists of two circular arrays, named VZERO-A and VZERO-C, of plastic scintillators which cover full azimuth and are positioned on either side of the interaction point. VZERO-A is located at $z = +340$ cm and covers $2.8 < \eta < 5.1$; while VZERO-C, installed at $z = -90$ cm, covers $-3.7 < \eta < -1.7$; see [25] for more details.

Each VZERO disk is divided into 32 cells: four rings of eight sectors which are distributed symmetrically in azimuth. Figure 2.7 (left) shows the segmentation of the VZERO-A detector. Each cell is capable of an independent measurement of the number of particles traversing its volume. Figure 2.7 (right) shows charged particle multiplicity per event as a function of pseudo-rapidity measured by tracklets reconstructed from the SPD and both VZERO disks in central Pb–Pb collisions.

Due to its very fast response (few ns), the detector is used for minimum bias trigger, beam-gas rejection and centrality characterisation. Furthermore due to its pseudo-rapidity coverage and in spite of its coarse granularity, the detector is used to estimate the second order flow angle and particle correlations with large η gap as it will be discussed in the following chapters.

The anisotropic coefficient v_n for reconstructed decays in Pb–Pb collisions

3

The LHC physics program started in November 2009 and continued until February 2013 with short stops which were used for small reparations and minor modifications in their detectors. During this period, referred to as *LHC long run 1* (LR1), collisions of several systems were recorded. The following table summarises the LHC operations:

	System	$\sqrt{s}$ (TeV)	$\sqrt{s_{NN}}$ (TeV)
November 2009	p–p	0.9	
March 2010	p–p	7.0	
October 2010	Pb–Pb		2.76
April 2011	p–p	2.76	
November 2011	Pb–Pb		2.76
April 2012	p–p	8.0	
September 2012	Pb–p and p–Pb		5.02
February 2013	p–p	2.76	

ALICE recorded events in all of these beam configurations, however the analysis presented in this thesis corresponds to Pb–Pb collisions exclusively. The LHC can deliver Pb–Pb collisions in ALICE at a constant rate for several hours. When the beam intensity deteriorates below a certain threshold, the accelerator team informs the experiments so that they stop the data acquisition. The beam is then dumped and the procedure for beam renewal begins. The recovery process can take several hours and involves many steps: beam injection, ramping of energy, stabilisation of beams and focusing for collisions. Therefore ALICE records events in samples fragmented in time and organised in *run numbers*. Some of those samples have problems either with the data acquisition or with lags in the detector. When the data of any of the sub-detectors used in this analysis was compromised and could not be restored by offline recalibration, the run was not considered in this analysis. See appendix A for a list of the run numbers used in this analysis.

3.1 TRIGGER AND CENTRALITY DETERMINATION

The *trigger* is the signal sent to the detectors in order for them to start a recording period. The ALICE strategy uses several trigger solutions in order

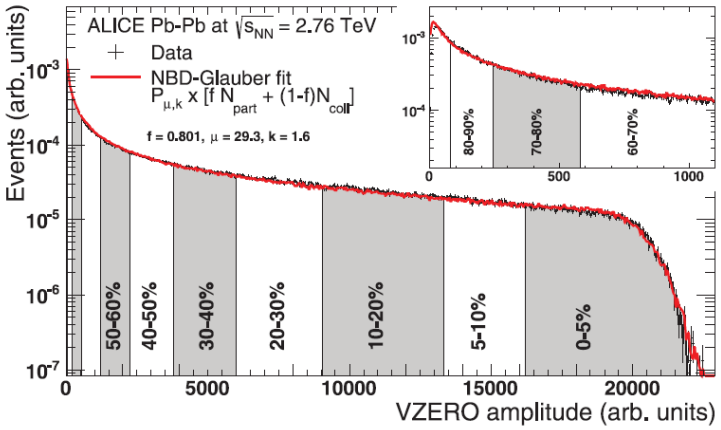

Figure 3.1 Distribution of the VZERO amplitude in Pb–Pb collisions at 2.76 TeV. The alternating grey and white areas indicate the intervals used for centrality selection. A Monte Carlo model is fitted to the data and allows for the classification of events into percentiles of the total hadronic cross section. The inset shows an enlarged view of the region of the small VZERO amplitude which corresponds to the most peripheral collisions.

to cope with the different physics analyses. For instance, for the analysis of muons reconstructed with the forward spectrometer, the detectors involved are only those at forward rapidity and due to their fast response time the trigger could work at very high rate. However whenever the TPC is included in the readout partition, the trigger rate levels off with the TPC response time[1] ($\sim$ 100 Hz)

For the analysis of 2010 data a *minimum-bias trigger* was used. This trigger was constructed by using the total signal registered in the VZERO and the activity in the integrated circuits of the SPD [26]. The events recorded in this mode allow us to measure the dependence of elliptic flow on centrality. Using the events recorded in this period, a pilot study on the elliptic flow of D^0 was also performed which gave us a hint of a remarkably large azimuthal asymmetry for these particles. Although these results were not made public they were reported during 2011 ALICE's collaboration meeting [27]. Based on the pilot analysis, a dedicated trigger for *semi-central collisions* was formed and included in the 2011 data taking. This new trigger relied on the total signal on the VZERO detectors only tuned for a specific centrality range aiming at semi-central collisions where the larger anisotropy is expected. The outcome

[1] This is driven by the readout bandwidth. The intrinsic TPC dead time including the drift time and the time the gate needs to be closed is 280 μs, which is equivalent to a limiting frequency of 3.5 kHz.

was a sample three times bigger than the one recorded in the previous year in the same centrality range.

After the events were recorded, a second stage in the selection was performed by an offline procedure. Here the number of beam-gas collisions is reduced by a time coincidence between both VZERO discs and the requirement of a reconstructed primary vertex by the central tracking system. Detailed information about the trigger system and the modes configured for the LR1 can be found in [18].

Centrality is determined through the event multiplicity using a geometric Glauber model [28] for the initial density profile and a particle production model to connect particle abundance to nuclear overlap. Several detectors are used in order to measure particle abundances: the total signal measured by the VZERO (VoM), the number of tracks measured by the TPC (TRK) and the number of tracklets reconstructed by the SPD (CL1).

The *centrality classes* obtained are defined in terms of percentiles of the total hadronic cross section. Due to the increase of the electromagnetic cross section in very peripheral collisions, the centrality framework works very well only from 0% to 90% with a resolution of 0.5% in most central up to 2% for most peripheral. Figure 3.1 shows the centrality percentiles associated to the VZERO total amplitude for events recorded during 2010. Detailed information on the centrality determination can be found in [28]. In order to ensure a good performance of the centrality estimation, only events with a reconstructed vertex not further than 10 cm along the z-direction from the nominal interaction point were considered in the classification.

3.2 THE Q_N RECONSTRUCTION

3.2.1 *The Q_n vector*

The Q_n vector[2] and the flow angle Ψ_n were formally introduced in [29, 30], although traces of its conceptual origin might date back to the analysis of shape variables [31]. The Q_n vector is defined as the sum of unit vectors in the complex plane made out of the direction of the particles produced in a heavy-ion collisions, according to

$$Q_n \equiv \sum_i^M \exp \imath n \varphi_i \tag{3.1}$$

[2]When first introduced, $\vec{Q}_n$ was defined as a vector in the transverse plane (with two real components) in this thesis and in (most) current literature this vector is replaced by a complex number. Although not formally correct, I will keep calling it vector since that is how is commonly known by the community.

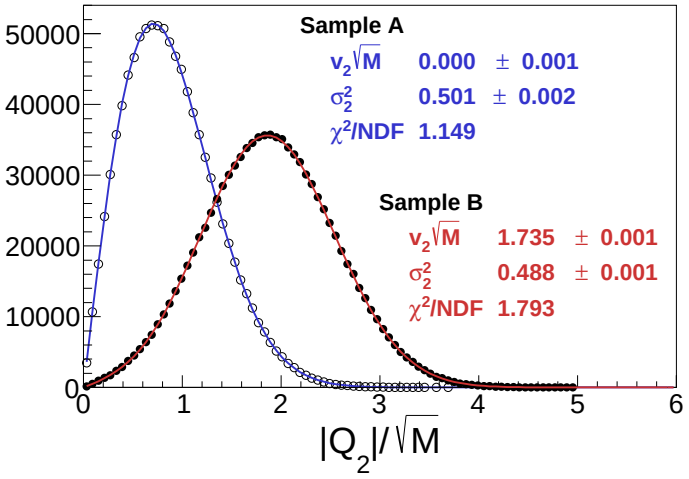

Figure 3.2 q_2 distribution of two samples generated by a 0.1 million Monte Carlo events with random Ψ_2. In each event, 300 particles are generated with azimuthal direction given by equation 1.2. Sample A (open markers) corresponds to events with no anisotropy, i.e. $v_n = 0$. Sample B (full markers) corresponds to events with only $v_2 = 0.1$ and zero for all other harmonics.

where φ_i is the azimuthal angle of the transverse momentum vector of the i-th particle measured in the laboratory frame and the sum runs over all available particles M in the event. Every Q_n vector has associated to it a n-th order flow angle Ψ_n which is obtained from the argument of the Q_n vector using the following definition

$$Q_\mathrm{n} \equiv |Q_\mathrm{n}| \exp \imath n \Psi_n. \tag{3.2}$$

The magnitude of the v_n coefficient is directly accessible from the distribution of the length of the Q_n vector. When the azimuthal direction of the particles are not correlated, equation 3.1 equals the sum of unit vectors with random direction - which is similar to the problem of the random walk [32]. In the presence of non-zero v_n, the distribution of $|Q_\mathrm{n}|$ deviates from that of a random walk moving its mean to higher values. An analytical approximation of such distribution reads [33]

$$\frac{dN}{dq_n} = \frac{q_n}{\sigma_n^2} \exp\left(-\frac{a^2 + q_n^2}{2\sigma_n^2}\right) \mathrm{I}_0\left(\frac{q_n a}{\sigma_n^2}\right), \tag{3.3}$$

where I_0 is the zeroth order modified besel function of the first kind, $q_n = |Q_n|/\sqrt{M}$, σ_n^2 characterises the width of the distribution, $a = v_n\sqrt{M}$, and M is the multiplicity of the event.

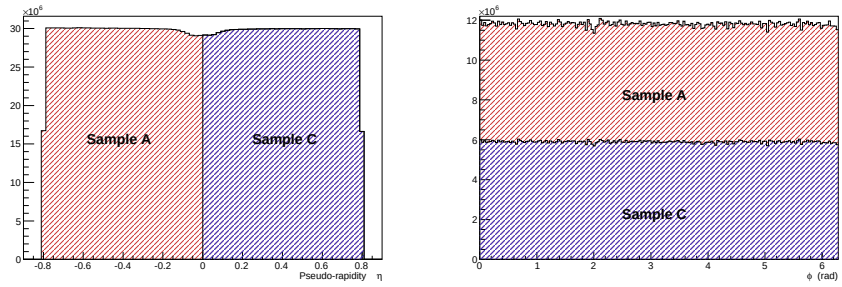

Figure 3.3 Pseudorapidity (left) and azimuthal (right) distribution of central tracks for events in centrality class 10-20%.

Figure 3.2 shows the q_n distribution of two generated samples of 0.1 million events each with fixed multiplicity $M = 300$. The particles in sample A were generated isotropically (random walk), while those in sample B were injected with a direction following a purely elliptical azimuthal distribution $1 + 0.2\cos(2\varphi)$ (i.e. $v_2 = 0.1$). The fit parameters obtained when modelling the distribution using equation 3.3 reproduce the input values quite well.

The Q_{n} vectors used in this analysis are reconstructed from two detectors: the ITS-TPC (central tracks) and the VZERO (forward pseudo-tracks).

3.2.2 *Reconstruction of the reference Q_{n} vectors from central tracks*

Central tracks are defined as tracks measured by the combined ITS-TPC tracking procedure that pass several quality and topological cuts. These tracks are required to

- have at least 70 number of TPC space points associated to them, with a χ^2 of the momentum fit per degree of freedom of less than 2 during the third iteration of the track fitting procedure,
- have a distance of closest approach to the primary vertex inside an ellipsoid with axis of 2.4 cm in the xy plane and 3.2 cm in the z direction,
- have pseudo-rapidity in the range of $[-0.8, +0.8]$, and
- have transverse momentum in the range of $[0.2, 5.0]$ GeV/c.

The first two requirements warrant a good balance between efficiency in the track reconstruction and fake track rejection [22]. The last two requirements aim to maximise the sensitivity to the azimuthal asymmetry of the event.

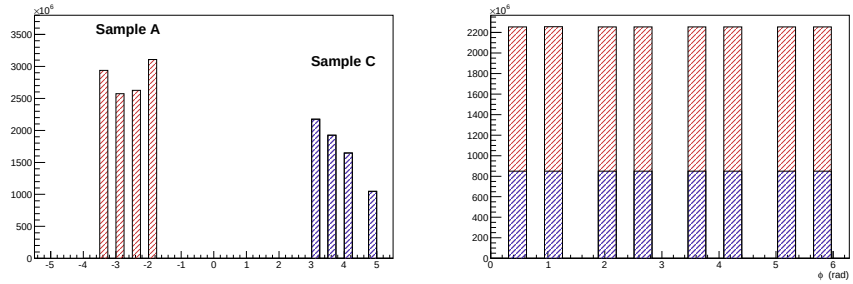

Figure 3.4 Pseudorapidity (left) and azimuthal (right) distribution of forward pseudo-tracks for events in centrality class 10-20%.

The central tracks are divided into two groups (A and C) according to the sign of their pseudo-rapidity. Figure 3.3 shows the pseudo-rapidity and azimuthal distribution of both sets reconstructed in 1.6 million Pb–Pb collisions that correspond to the centrality class $10-20\%$. Both sets present full azimuthal coverage and homogeneous efficiency. Three Q_{n} vectors constructed from central tracks are used in the present analysis: $Q_n^{\mathrm{TPC;A}}$ and $Q_n^{\mathrm{TPC;C}}$, constructed from central tracks with negative and positive pseudo-rapidity, respectively, and $Q_n^{\mathrm{TPC}} = Q_n^{\mathrm{TPC;A}} + Q_n^{\mathrm{TPC;C}}$ constructed from all central tracks. All of these Q_{n} vectors are computed using equation 3.1.

3.2.3 *Reconstruction of the reference Q_{n} vectors from forward pseudo-tracks*

Pseudo-tracks are built using the VZERO detector. The signal extracted from each VZERO cell is proportional to the amount of minimum ionising particles crossing it. The strategy adopted in this thesis was to build a pseudo-track for each cell by acquiring its azimuthal and pseudo-rapidity position. The signal registered in each cell is used as weight to convert equation 3.1 into:

$$Q_n^{\mathrm{VZERO-A}} = \sum_{\mathrm{i}=1}^{32} \mathrm{S_i} \times \exp\left(\imath n \varphi_{\mathrm{i}}\right) \tag{3.4}$$

where φ_{i} measures the azimuthal angle of the centre of the VZERO-A cell and $\mathrm{S_i}$ is its corresponding signal. Another Q_{n} vector for VZERO-C was build accordingly.

During the 2010 data taking, the azimuthal efficiency of the VZERO system was not uniform and varied with time. For this period a calibration of the VZERO system was needed. The details of the calibration procedure is reported in appendix B.

Figure 3.4 shows the pseudo-rapidity and azimuthal distribution of the signal registered in the VZERO detector for 1.6 million Pb–Pb collisions that correspond to centrality class $10 - 20\%$. The segmentation of the VZERO detector, shown in figure 2.7, becomes apparent in these distributions. Notice that each ring of the VZERO-A and VZERO-C records different total signal, a fact that comes from secondary production and signal normalisation. However, this pseudo-rapidity scaling has no effect in the reconstruction of the Q vector, see appendix B. The distribution in azimuth, on the other hand, is quite flat, as can be seen from the pile distribution in figure 3.4. The overall difference in the number of counts from sample A and C is reflected on both distributions.

3.3 V_N OF RECONSTRUCTED DECAYS

The azimuthal anisotropy coefficient v_n for reconstructed decays at lower energies have been reported by PHENIX [34–38] and STAR [15, 39–46]. These experiments measured v_n of decays by analysing the yield of the candidates in bins of $\Delta\varphi$ which accounts for the difference between the azimuthal angle of the candidate and Ψ_2. This methodology presents several limitations. The most important one is that the observable is affected by flow-fluctuations in an uncontrolled way [47] measuring a value somewhere between $\langle v_2 \rangle$ and $\sqrt{\langle v_2^2 \rangle}$. The actual value depends on the strength of the event-by-event flow-fluctuations and on the accuracy with which the second order flow angle is reconstructed, which in turn depends on the multiplicity and v_2 of the event at hand with both quantities being centrality dependent.

It has been shown than multi-particle correlation methods provide a complete control over flow-fluctuations and spurious flow [48, 49] and, thus, they were adopted in the present analysis. To this end, each reconstructed candidate - *particle of interest* (POI) - is correlated with one or more *reference particles* (RPs). The methods used in this analysis and their reach will be explained in the following section.

3.4 METHODS TO MEASURE DIFFERENTIAL V_N

Since "flow" affects the azimuthal distribution of all particles in the event, it can be quantified directly by performing an azimuthal correlation between two or more particles [50].

However, flow is not the only mechanism which imprints azimuthal correlation among particles. Resonance decays and jets also create correlations

among the particles produced in heavy-ion collisions. Every single correlation not connected to the common plane is called *non-flow*. Most of these correlations are localised in phase space[3] and therefore can be suppressed by correlating, for instance, particles from different pseudo-rapidity regions [47].

In this thesis two types of correlations are studied: two-particle correlations and four-particle correlations.

3.4.1 *Two-particle azimuthal correlations*

A two-particle azimuthal correlation is an event-wise observable defined as [50]:

$$\langle 2 \rangle_n \equiv \langle \exp n\imath \left(\varphi_i - \varphi_j \right) \rangle, \tag{3.5}$$

where φ_i and φ_j denote the azimuthal angle of particle i and j, respectively. The average is computed over all possible distinct pairs available in a single event.

When particles i and j are correlated only through the n-order flow angle the correlator can be *factorised* and directly connected to v_n through the following equation

$$\begin{aligned} \langle \langle 2 \rangle_n \rangle &= \langle \langle \exp n\imath \left(\varphi_i - \Psi_n + \Psi_n - \varphi_j \right) \rangle \rangle \\ &= \langle \langle \exp n\imath \left(\varphi - \Psi_n \right) \rangle \langle \exp n\imath \left(\Psi_n - \varphi \right) \rangle \rangle = \langle v_n^2 \rangle. \end{aligned} \tag{3.6}$$

3.4.1.1 *v_n from the second order Q-Cumulant: $v_n\{2\}$*

The analysis of v_n through cumulants, introduced in [50], provides a versatile technique in order to compute the harmonics from multi-particle correlations.

In order to compute differential v_n two Q_{n}-like vectors need to be constructed. Following the notation of [51], these vectors are named: Q_{n}, constructed from RPs; and p_{n}, made out of POIs in a specific p_{T}, η and mass[4] bin.

Using equations 3.2 and 3.5, the relevant two-particle correlator can be written as [51, 52]

$$\langle 2 \rangle_{n;p,Q} = \frac{p_n Q_n^* - m_q}{m_p M - m_q}, \tag{3.7}$$

where M is the number of RPs, m_p is the number of POIs and m_q is number of particles belonging to both sets (zero for reconstructed decays). The cumulant of this correlator is defined as [14]

$$d_n\{2\} \equiv \langle \langle 2 \rangle_{n;p,Q} \rangle \tag{3.8}$$

[3] There are, however, long-range correlations, coming from for instance di-jets which introduce long range - in pseudo-rapidity - correlations and might play also a significant role.

[4] invariant mass will be properly introduced in the next chapter.

where the last average is taken over events.

Following the steps shown in equation 3.6, $d_n\{2\}$ can be identified as the product of the v_n for RPs and that from POIs. By replacing p with Q in equation 3.8 one obtains the cumulant associated with RPs only $r_n\{2\}$. Thus, following the prescription of [50], the $v_n\{2\}$ of the particles of interest is computed as

$$v_n\{2\} = \frac{d_n\{2\}}{\sqrt{r_n\{2\}}}, \tag{3.9}$$

3.4.1.2 v_n *from Scalar Product method:* $v_n\{2;\Delta\eta\}$

Decaying particles imprint trivial correlations to its daughters due to conservation of energy and momentum. In the presence of such non-flow correlations, a factorisation of the two-particle correlations - as the one shown in equation 3.6 - is not guaranteed. However since non-flow implies correlation of particles close in phase space, this component can be reduced by imposing a pseudo-rapidity difference between the particles being correlated.

There are several ways to incorporate a pseudo-rapidity separation into two particle correlations. The method used here is called *Scalar Product*, since it is based on the inner product of Q vectors made out of particles from different pseudo-rapidity regions.

Following equation 3.9, the v_n is defined as

$$v_n\{2;\Delta\eta\} \equiv \frac{\langle p_n\, Q_n^* / m_p M\rangle}{\sqrt{\langle Q_n\, Q_n'^* / MM'\rangle}} \tag{3.10}$$

where the p_n vector is made out of POIs, while the Q_n and Q_n' vectors are made out of two sets of RPs here called set A and set C, respectively. Two pseudo-rapidity separations are enforced: the first $\Delta\eta_1$ between the POIs and set A in order to diminish non-flow in the numerator, and the second $\Delta\eta_2$ between set A and C to do the same in the denominator. In principle the larger the gap, the better the non-flow suppression. In practice $\Delta\eta >\sim 0.8$ is enough to remove a large fraction of the correlations coming from jet fragmentation. To be conservative, the label $\Delta\eta$ in the left-hand-side of equation 3.10 is taken as the minimum pseudo-rapidity separation achievable, i.e. $\Delta\eta = \mathrm{MIN}\,(\Delta\eta_1, \Delta\eta_2)$.

Some source of non-flow, for instance jets, can introduce correlations to particles in a broad pseudo-rapidity region. In order to suppress as much non-flow as possible, large $\Delta\eta$ separation is preferred. This practice usually involves moving to forward rapidity regions to measure RPs sometimes creating an imbalance in the degree of anisotropy recorded in Q_n and Q_n'. When

the v_n of the RPs in Q_n is not the same as in Q'_n, equation 3.10 is no longer valid. Many adaptations of 3.10 can be found in literature [47]. In this thesis the following solution was adopted

$$v_n\{2;\Delta\eta\} \equiv s\sqrt{\frac{|\langle p_n\, Q_n^* / m_p M\rangle\langle p_n\, Q_n'^* / m_p M'\rangle|}{\langle Q_n\, Q_n'^* / MM'\rangle}}, \tag{3.11}$$

where s is the sign of the v_n coefficient. The sign of the v_n coefficient is evaluated from the sign of the pQ correlations in the numerator.

3.4.2 *Four-particle azimuthal correlations*

A four-particle azimuthal correlation is an event-wise observable defined as [50]:

$$\langle 4\rangle_n \equiv \langle \exp n\imath\left(\varphi_i + \varphi_j - \varphi_k - \varphi_l\right)\rangle, \tag{3.12}$$

where φ_i denotes the azimuthal angle of particle i. The average is computed over all possible combinations of four distinct particles.

By performing a similar analysis of that shown for the two-particle correlator, one obtains that the four-particle correlator is proportional to the fourth power of v_n.

3.4.2.1 *v_n from the fourth order Q-Cumulant: $v_n\{4\}$*

The four-particle correlator can be constructed using three Q_n vectors: p, Q and q. The first two correspond to the ones constructed from particles of interest and reference particles, respectively. The third one is constructed with the particles which belong to both groups at the same time. The four-particle correlation is [52, 53]

$$\begin{aligned}\langle 4\rangle_{n;p,Q,q} =&[p_n Q_n^* |Q_n|^2 - q_{2n} Q_n^* Q_n^* - p_n Q_n Q_{2n}^* + q_{2n} Q_{2n}^* - 2M\, p_n Q_n^* \\ &- 2m_q |Q_n|^2 + 7 q_n Q_n^* - Q_n q_n^* + 2 p_n Q_n^* + 2 m_q M \\ &- 6 m_q]/\left(m_p\, M - 3 m_q\right)(M-2)\,(M-1)\end{aligned} \tag{3.13}$$

The cumulant of this correlator is defined as [14]

$$d_n\{4\} \equiv \langle\langle 4\rangle_{n;p,Q,q}\rangle - 2\langle\langle 2\rangle_{n;p,Q}\rangle\langle\langle 2\rangle_{n;Q,Q}\rangle, \tag{3.14}$$

and it is proportional to the v_2 of the particles of interest multiplied three times by the v_2 of the reference particles. The cumulant associated with the reference particles only can be computed by replacing p and q with Q. This cumulant - named $r_n\{4\}$ - is equal to the four power of the v_2 of reference particles. Thus $v_n\{4\}$ for the particles of interest can be computed as[14]

$$v_n\{4\} = -\frac{d_n\{4\}}{\sqrt[4]{-r_n\{4\}}^3} \tag{3.15}$$

Provided that non-flow is not present, the main difference between the observables $v_n\{2\}$ and $v_n\{4\}$ is in their sensitivity to small fluctuations when averaging over many events. The size of the fluctuations can be quantified from equations 3.9 and 3.15 by considering the anisotropy of all particles (setting $p_n = Q_n$). Under this consideration these observables become

$$v_n\{2\} = \langle v_n^2 \rangle^{1/2} \qquad v_n\{4\} = \left(-\langle v_n^4 \rangle + 2\langle v_n^2 \rangle^2 \right)^{1/4} \tag{3.16}$$

where $\langle\ \rangle$ denotes the average over events. Thus in the presence of event–to–event v_n fluctuation these observables are clearly biased.

Two types of eccentricity fluctuations are usually considered in literature [52, 54]: i) Gaussian fluctuations (that would result from statistics), and ii) Bessel-Gaussian fluctuations (which would result from fluctuations of the Q vector distribution).

For a purely Gaussian fluctuation we have

$$\mathrm{v_n}\{2\} \simeq \langle \mathrm{v_n} \rangle + \frac{\sigma^2}{2\langle \mathrm{v_n} \rangle} \qquad \mathrm{v_n}\{4\} \simeq \langle \mathrm{v_n} \rangle - \frac{\sigma^2}{2\langle \mathrm{v_n} \rangle}, \tag{3.17}$$

while for Bessel-Gaussian fluctuations we have

$$\mathrm{v_n}\{2\}^2 \simeq \langle \mathrm{v_n} \rangle^2 + 2\sigma^2 \qquad \mathrm{v_n}\{4\} \simeq \langle \mathrm{v_n} \rangle, \tag{3.18}$$

where σ^2 is the variance of v_n when averaging over all events. Both expressions are valid as long as $\sigma \ll \langle \mathrm{v_n} \rangle$, second order and above corrections were neglected, an approximation usually used in literature.

Thus the relative size of the fluctuations become experimentally accessible by combining $v_2\{2\}$ and $v_2\{4\}$ in either of the two following ways

$$\sigma_n^{\mathrm{G}} / \langle v_n \rangle \simeq \sqrt{2\frac{v_n\{2\} - v_n\{4\}}{v_n\{2\} + v_n\{4\}}} \qquad \sigma_n^{\mathrm{BG}} / \langle v_n \rangle \simeq \sqrt{\frac{v_n\{2\}^2 - v_n\{4\}^2}{v_n\{2\}^2 + v_n\{4\}^2}}. \tag{3.19}$$

where once more the approximation for small relative fluctuations was used.

These observables will be re-discussed in chapter 5, where the measurement of $\sigma_n^{\mathrm{BG}} / \langle v_n \rangle$ for both $\mathrm{K_s^0}$ and Λ will be compared to that for charged particles.

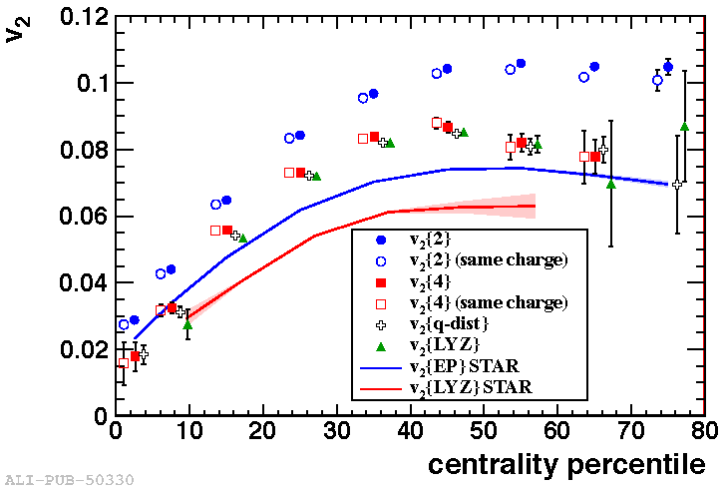

Figure 3.5 (Color online) Centrality dependence of charged particles v_2 in Pb–Pb at $\sqrt{s_{\mathrm{NN}}} = 2.76$ TeV using 2– and 4–particle azimuthal correlations. The open markers correspond to correlation of particles of same charge. Computation using Lee-Yang-Zeroes and fit of the Q distribution methods are also shown. The bands correspond to measurements in Au–Au collisions at $\sqrt{s_{\mathrm{NN}}} = 200$ GeV. Figure extracted from [49].

3.6 INTEGRATED V_N

Integrated v_n is defined as

$$v_n = \int_0^\infty \mathrm{d}p_{\mathrm{T}} \frac{\mathrm{d}N_{\mathrm{AA}}}{\mathrm{d}p_{\mathrm{T}}}(p_{\mathrm{T}}) \times v_n(p_{\mathrm{T}}). \tag{3.20}$$

Figure 3.5 shows the centrality dependence of the integrated v_2 of charged particles measured in Pb–Pb collisions at $\sqrt{s_{\mathrm{NN}}} = 2.76$ TeV using several methods. When computing $v_2\{2\}$ using only like-sign charged particles there is a small decrease in the correlation with respect to all charged particles for most peripheral collisions ($> 40\%$). The decrease could be attributed to a reduction of non-flow from neutral particles decaying into two charged particles. On the other hand $v_2\{4\}$, which only contains non-flow coming from four or more particles, is well below v_2 and shows no further reduction when only same charge particles are used.

3.7 FINAL REMARKS ON THE V_N COMPUTATION

For the analysis of decaying particles, the reconstructed candidates are classified in bins according to their invariant mass. The candidates in each mass

bin enter into the computation of v_2 using either the Scalar Product or the Q-Cumulants method. Previous studies [52] show that the numerical convergence of the flow algorithms depends on two things: the degree of the azimuthal anisotropy and the amount of particles in the event. In practice, fortunately, small values of flow are found in most central events - where multiplicities are the highest; and large values of flow are found in more peripheral events - where typical multiplicities in acceptance are of the order of few hundreds particles. However when we measure the elliptic flow of candidates as function of mass, for some mass bins - the ones far from the peak region - not many candidates are available. Since these candidates are correlated with the reference flow particles -whose multiplicity never goes below 100 per event, a very small amount of candidates per mass bin are needed in order for the algorithm to converge. Notice that this requirement on the minimum number of candidates per mass bin is for the whole event sample - since the relevant average is taken over all events. This is crucial since it allows us to study the anisotropic flow of particles as scarce as the D^0.

There is a trivial azimuthal correlation among the reconstructed decay and its daughters. When measuring the elliptic flow using the Q-Cumulants method, the Q vector and the daughters of the decay are reconstructed both in the central barrel in the pseudo-rapidity range $[-0.8, +0.8]$. In order to avoid trivial correlations, when doing Q-cumulants via two particle correlation (as for D^0) and when any of the daughters of the reconstructed decay was used in the construction of the Q vector, the Q vector is modified such that the contribution of these daughters are excluded. In practice, since for the D^0 there is only at most one candidate per event, the correction on the Q vector is minimal.

The v_2 of K^0_s, Λ and D^0

4

The particles used in this analysis are reconstructed from their weak decay into two charged hadrons. The channels used in the reconstruction are the following:

K^0_s	$\rightarrow$	$\pi^+ + \pi^-$	$\Gamma_i/\Gamma_{tot} = 69.2\%$	$c\tau = 2.684$ cm,
Λ	$\rightarrow$	$p + \pi^-$	$\Gamma_i/\Gamma_{tot} = 63.9\%$	$c\tau = 7.89$ cm,
D^0	$\rightarrow$	$\pi^+ + K^-$	$\Gamma_i/\Gamma_{tot} = 3.88\%$	$c\tau = 122.9$ μm.

4.1 SELECTION OF THE DECAY DAUGHTERS

The decay products were reconstructed using the combined ITS and TPC tracking procedure. The following track properties were considered:

The *impact parameters* of the track (IP_{xy} and IP_z) are defined as the projection of the distance of closest approach between the primary vertex and the helix traced by the track in the xy plane and the z axis, respectively. The sign of IP_z depends on the z-position in the laboratory frame, while that for IP_{xy} depends on the concavity of the track's spiral, both with respect to the primary vertex in the transverse plane (xy-plane). For K^0_s and Λ reconstruction and due to their long decay length, tracks with large IP_{xy} were chosen in order to reduce the combinatorial background. The strategy is opposite for D^0 reconstruction,

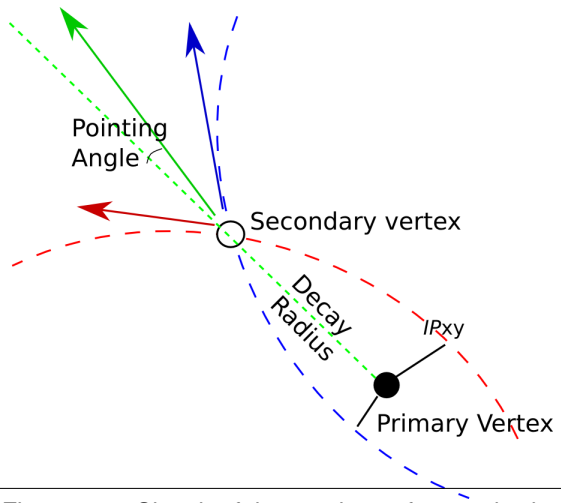

Figure 4.1 Sketch of the topology of a two–body decay.

$\lvert IP_{xy} \rvert$ (cm)	≥ 0.1
TPC space points	≥ 70
TPC-refit χ^2/n.d.f.	≤ 2.0
p_T (GeV/c)	≥ 0.1
η–range	$[-0.8, +0.8]$

Table 4.1 Selection criteria for the daughters of K^0_S and Λ

$\lvert IP_{xy} \rvert$ (cm)	$[0.005, 0.1]$
$\lvert IP_z \rvert$ (cm)	≤ 0.1
ITS space points	≥ 2
SPD space points	≥ 1
TPC space points	≥ 70
TPC-refit χ^2/n.d.f.	≤ 2.0
p_T (GeV/c)	> 0.5
η–range	$[-0.8, +0.8]$

Table 4.2 Selection criteria for the daughters of D^0

where tracks very close to the vertex are preferred. The latter were chosen by an upper cut in the IP_{xy} and IP_z, while leaving a minimum cut in the IP_{xy} so that the displaced vertex can be resolved.

The *ITS–refit* and *TPC–refit* are requirements in the usage of clusters associated with these detectors during the third iteration of the fitting procedure for this track [21]. The χ^2 *of the momentum fit per degree of freedom* in the TPC–refit is used as a quality control parameter in the track selection.

A track can have a maximum of 159 *TPC space points* associated with it. In order to ensure a good efficiency and momentum resolution while keeping the reconstruction of fake tracks to a minimum, each track is required to contain at least 70 TPC space points. Monte Carlo simulations show that under these conditions the fake ratio is below 1% and the efficiency for track reconstruction is close to 100% [22].

Similarly a track can have a maximum of 6 *ITS space points* associated with it: two from each sub detector. For D^0 reconstruction the tracks are required to have at least one space point reconstructed in the SPD, the innermost layers of the ITS.

The selection criteria for the decay daughters are summarised in tables 4.1 and 4.2.

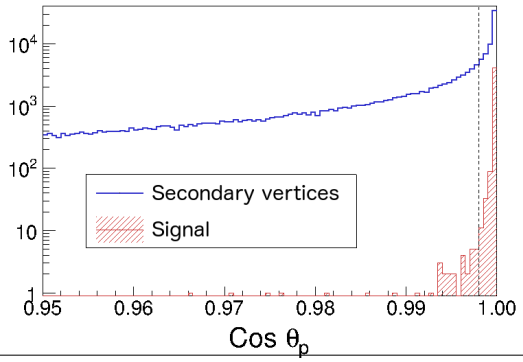

Figure 4.2 Cosine of pointing angle for reconstructed K^0_s candidates compared to the distribution from real decays. Sample extracted from a Monte Carlo simulation of particles produced in Pb–Pb collisions propagated through the reconstruction chain in the ALICE detector.

4.2 RECONSTRUCTION OF THE DECAY VERTEX

Particles with opposite charge are propagated to their *Distance of Closest Approach* (DCA) where the reconstruction of the potential secondary vertex is performed. Each track is displaced along the helix reconstructed during the tracking procedure. The magnitude and direction of each track are recomputed based on the amount of material that they traverse. The secondary vertex is placed on the line connecting the two daughters' tracks at the points of the DCA. The vertex is determined using the covariance matrix of each track as weight.

In order to increase the signal over background ratio of the sample and to minimise the amount of feeddown from other decays, several geometrical cuts were imposed. The topological cuts used in this analysis are the following:

The *cosine of the pointing angle* ($\cos\theta^p_{xy}$) is the cosine of the angle in the transverse plane between the reconstructed transverse momentum of the candidate and the line subtended by the primary and its secondary vertex, see figure 4.1. Primary particles which decay into two charged hadrons present a relatively small value of the pointing angle, which leads to values of $\cos\theta^p_{xy}$ close to one. Besides its leverage in signal over background discrimination, this variable is very powerful in reducing contamination from feeddown decays. Figure 4.2 shows the $\cos\theta^p_{xy}$ distribution of signal-like and background-like candidates for secondary vertices reconstructed using the track selection of a K^0_s particle. In addition to $\cos\theta^p_{xy}$, the cosine of the pointing angle in 3D space was also used in order to reduced background using directionality in the z-direction. The cut used was about 10% looser than $\cos\theta^p_{xy}$.

p_T (GeV/c)	$[0.4 - 1.2]$	$[1.2 - 2.0]$	$[2.0 - 12.0]$
Pseudorapidity	$\|\eta\| < 0.8$	$\|\eta\| < 0.8$	$\|\eta\| < 0.8$
Rapidity	$\|y\| < 0.5$	$\|y\| < 0.5$	$\|y\| < 0.5$
DCA (cm)	< 0.5	< 0.5	< 1.0
R_{xy} (cm)	> 5.0	> 5.0	> 1.0
$\cos\theta^{p}_{xy}$	> 0.998	> 0.998	> 0.998
PID daughters	yes	no	no

Table 4.3 Selection criteria used in the decay topology of K^0_s and Λ.

The measurement of the $\cos\theta^{p}_{xy}$ requires the ability to differentiate the position of the secondary vertex with respect to the primary vertex. This can be enforced in two ways.

1. Method one consists of a minimum cut in the *decay radius* (R_{xy}), which is defined as the distance in the transverse plane from the primary vertex to the secondary vertex. This method is optimal for particles with long decay length: K^0_s and Λ. For these candidates, the decay radius is chosen to be above 1 cm for $p_T > 2$ GeV/c and above 5 cm for $p_T \leq 2$ GeV/c.

2. Method two uses a maximum cut in the *product of impact parameters* ($IP^{+}_{xy} \times IP^{-}_{xy}$), which is defined as the signed product of the IP_{xy} of both daughters. For D^0 candidates this method has the additional advantage to remove a large fraction of the combinatorial background as well. The overwhelming combinatorial background is reduced by rejecting positive values of $IP^{+}_{xy} \times IP^{-}_{xy}$. For D^0 the cut was set at $\sim -10^{-4}$ cm^2.

The *cosine of the decay angle* ($\cos\theta^*$) is the cosine of the angle between the reconstructed transverse momentum of the candidate in the laboratory frame and the direction of one of its daughters when the decay is boosted to its centre of mass as shown in figure 4.3. Due to the asymmetry of the system, a cut in this variable for the D^0 is very useful in removing a large part of the background. For D^0 the decay angle is computed with respect to the kaon daughter. Only candidates within the range $-0.8 < \cos\theta^* < +0.8$ are accepted. This cut is not needed for K^0_s and Λ since the signal over background ratio obtained by using $\cos\theta^{p}_{xy}$ and R_{xy} is already high.

The selection cuts used in the decay topology are summarised in tables 4.3 and 4.4.

4.3 ARMENTEROS-PODOLANSKI SPACE

A very useful tool to study strange particle decays was introduced in 1954 by R. Armenteros and J. Podolanski [55]. The method helps to statistically

p_{T} (GeV/c)	$[2.0, 4.0]$	$[4.0, 16.0]$
Pseudo-rapidity	$\lvert\eta\rvert < 0.8$	$\lvert\eta\rvert < 0.8$
Rapidity	$\lvert y\rvert < 0.7$	$\lvert y\rvert < 0.8$
PID daughters	yes	yes

p_{T} (GeV/c)	DCA (mm)	$\mathrm{IP}^{+}_{\mathrm{xy}} \times \mathrm{IP}^{-}_{\mathrm{xy}}$ (cm^2)	$\cos\theta^{\mathrm{p}}_{\mathrm{xy}}$
$[2.0, 3.0]$	< 0.25	$< -4.0 \quad 10^{-4}$	> 0.991
$[3.0, 4.0]$	< 0.25	$< -3.6 \quad 10^{-4}$	> 0.993
$[4.0, 6.0]$	< 0.25	$< -2.5 \quad 10^{-4}$	> 0.996
$[6.0, 8.0]$	< 0.27	$< -1.4 \quad 10^{-4}$	> 0.998
$[8.0 - 12.0]$	< 0.30	$< -5.0 \quad 10^{-5}$	> 0.995
$[12.0 - 16.0]$	< 0.35	< 0	> 0.995

Table 4.4 Selection criteria used in the decay topology of D^0.

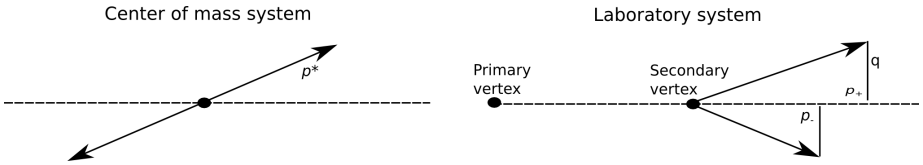

Figure 4.3 Decay kinematics in the laboratory and centre of mass frame.

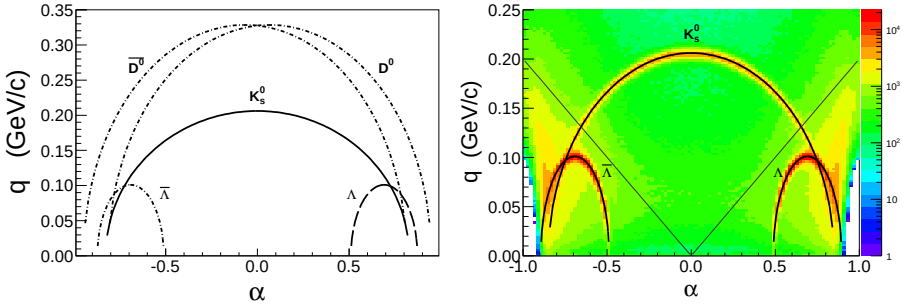

Figure 4.4 Left: α–q space for relativistic ($\beta = 1$) $\mathrm{K}^0_{\mathrm{s}}$, Λ and D^0 decays. Right: α and q distribution of candidates in p_{T} $[2.0; 2.4]$ GeV/c after applying the topological selection of table 4.3. The Armenteros-Podolanski parametrization corresponding to this p_{T} range for each species is overlaid. The boundary of the cut used in the $\mathrm{K}^0_{\mathrm{s}}$ analysis is also shown. Notice the strong separation power for Λ and $\bar{\Lambda}$ particles when using these cuts.

separate K^0_s and Λ by the usage of two kinematic variables: α and q. The transverse momentum of both daughters is decomposed orthogonally along the mother's momentum. $\alpha = \frac{p_+ - p_-}{p_+ + p_-}$ is defined as the asymmetry between the longitudinal components of both daughters. q is defined as the transverse component of the positively charged daughter - see figure 4.3 (right).

In the α–q space, relativistic particles coming from a physical decay lie on the line subtended by an ellipse due to energy and momentum conservation. The relationship between α and q is given by

$$\left(\frac{\alpha - a}{b}\right)^2 + \left(\frac{q}{p^*}\right)^2 = 1, \qquad a = \frac{E^*_+ - E^*_-}{m} \qquad b = \frac{2p^*}{\beta m} \tag{4.1}$$

where m is the mass of the decay and β its velocity. p^*, E^*_+, E^*_- are the momentum and energy of each daughter at the centre of mass - see figure 4.3 (left).

For K^0_s decaying into two charged pions ($E^*_+ = E^*_-$), a equals zero, thus the centre of the ellipse is at the origin of coordinates. On the other hand, for Λ decaying into a pion and a proton, the centre of the ellipse will be displaced to the right, while for $\bar{\Lambda}$ decaying into a pion and an anti-proton the centre will be at the opposite side. Thus, this variable is very useful to separate Λ from $\bar{\Lambda}$, even if the pion and proton are not individually identified.

Figure 4.4 (left) shows the α–q space with the expected curves from relativistic K^0_s, Λ, $\bar{\Lambda}$, $D^0$and $\bar{D}^0$ decays. Notice that, by construction, non-relativistic particles ($\beta < 1$) would lie on ellipses with enlarged minor axis as it transpires from equation 4.1.

Figure 4.4 (right) shows the distribution of α and q for candidates in the p_T range of $[2.0 - 2.2]$ GeV/c that have passed the topological selection. The candidates were selected from a sample of Pb–Pb collisions in centrality class 10-20%. It can be seen that the three bands - for K^0_s, Λ and $\bar{\Lambda}$ - are well separated.

Real decays that were reconstructed using the wrong mass assumptions for their daughters are called reflections. Since the decay topology for K^0_s and Λ are very similar, both K^0_s and Λ are the main source of reflections of one another. This can be seen in the intersection between the lines shown in figure 4.4 (right). The amount of reflections was diminished in the K^0_s sample by a cut in the α, q variables. Only candidates passing the requirement of $q > 0.2(\text{GeV}/c)^{-1}|\alpha|$ were accepted. For Λ, where such a cut is impractical, a rejection criterium using the mass hypothesis of the K^0_s reflection was implemented. On the other hand, the D^0 particle requires a special strategy since none of the previous solutions are accurate enough to reduce the reflections coming from its antiparticle. For candidates compatible with the cuts for both

D^0 and $\bar{D}^0$, the solution was to use the difference found in v_2 using both mass hypotheses as a systematic uncertainty.

In the analysis of Λ, the α variable was used to separate the sample into a Λ-like and a $\bar{\Lambda}$-like set. Additionally a 3σ cut on the dE/dx in the TPC was imposed to both daughters in order to enhance the signal over background ratio.

4.4 INVARIANT MASS ANALYSIS

The separation of signal over background is done through an analysis of the *invariant mass* (W) of the candidates. The invariant mass of a candidate is computed from the reconstructed momentum of its daughters and their mass hypothesis using the following expression.

$$W(p_1, p_2; m_1, m_2) = \sqrt{\left(\sqrt{m_1^2 + p_1^2} + \sqrt{m_2^2 + p_2^2}\right)^2 - (\mathbf{p_1} + \mathbf{p_2})^2}, \quad (4.2)$$

where $\mathbf{p}_1$, $\mathbf{p}_2$ are the reconstructed momentum of the two daughters, and m_1, m_2 are the masses associated with each daughter which were taken from [3].

The selection was tested in a Monte Carlo simulation. The simulation consists of 1 million Pb–Pb collisions generated using HIJING [56] that produce particles which are propagated to the ALICE detector using GEANT3 [57], a computer package to simulate the passage of particles through matter.

HIJING stands for Heavy Ion Jet INteraction Generator and was chosen by ALICE to study particle production in Pb–Pb collisions among other observables. HIJING uses low p_T multistring phenomenology together with pQCD inspired models.

The geometry, material budget and detector response of the ALICE detector was configured to match the elements installed at the time of the first Pb–Pb run in 2010. That includes switching off some regions of the ITS, which were not active, and simulating the variation of the response of the TPC as a function of time in order to match the conditions present during data taking. The procedure to reconstruct the event from the raw signal in the detectors was also the same as the one used for experimental data.

Monte Carlo (MC) particles coming either from the generator, from the interaction with the material or from decays are called *MC truth particles*. When one of these particles is close in space to a reconstructed track then the track is *matched* to it. The amount of fake matches is kept down by requiring that a certain fraction of the track's space points have only one matched track. In

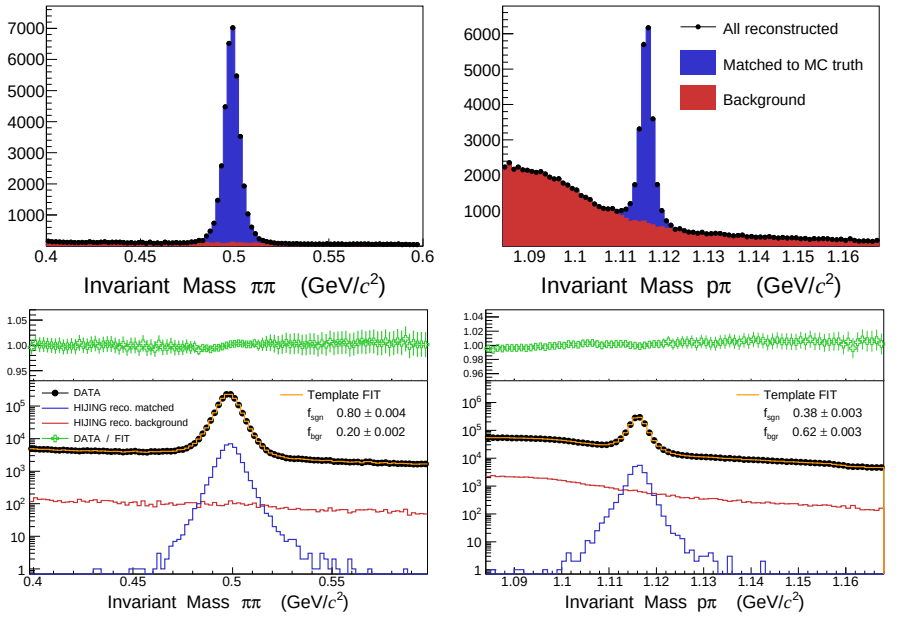

Figure 4.5 Top: (HIJING) Invariant mass of K^0_S (a) and Λ (b) candidates. 100 thousand events in centrality class 10-20% were simulated using Hijing Pb–Pb collisions. The candidates are separated into background and real K^0_S and Λ. Bottom: (Experimental data) Invariant mass of K^0_S (c) and Λ (d) in centrality class 10-20% and $1.2 < p_T < 1.4$. The data were fitted using MC templates from HIJING.

order to *match a decay*, four steps were followed: A) both reconstructed daughters were matched to a MC truth, B) the species of each daughter was required to be compatible with the decay at hand, i.e. two charged pions for K^0_S, and a (anti)proton and a pion for Λ, C) both MC particles had to come from the same decay, and finally, D) the species of the mother particle was correct.

Figure 4.5 shows the invariant mass of reconstructed K^0_S (left) and Λ (right) candidates in both MC and data in centrality class 10-20% for candidates with transverse momentum $1.2 < p_T < 1.4$. The reconstructed candidates in MC that were matched to a real K^0_S or Λ were separated from the combinatorial background. According to MC there is a good separation of signal over background even at low p_T (where the combinatorial background without any cut is overwhelming). There is also a smooth distribution of background candidates around the peak.

The W distributions found in data were fitted with MC templates from where the shape for signal and background was extracted. The shape of the invariant mass found in data is reproduced quite well by MC. However the

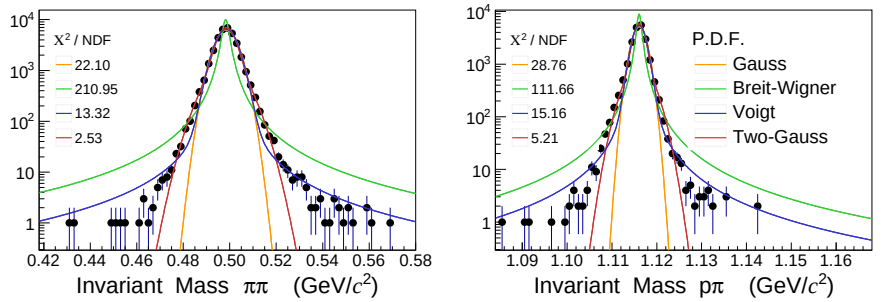

Figure 4.6 Invariant mass distribution of reconstructed candidates matched to a truth K^0_s or Λ particle for events in centrality class 10-20%. The distributions were fitted using four different functions.

relative signal and background fractions - quantified by f_{sgn} and f_{bgr} - are different. In data there is an enhancement of K^0_s and a reduction in Λrelative to HIJING, most likely due to the inaccurate prediction of HIJING of the particle ratios produced in heavy-ion collision at LHC energies. The ratio of the signal to the fit is computed in the upper panel. The deviations found are smaller than 0.5% and are located mainly close to the mass peak.

The invariant mass distribution of reconstructed particles matched to a MC truth particle is shown in figure 4.6. Theoretically, the distribution for resonance decays presents an underlying Breit-Wigner *probability density function* (pdf), where the decay width Γ, which equals the inverse of the life time $\hbar/\tau$, governs the width of the distribution. Experimentally, the finite momentum resolution of the daughters causes a smearing on the invariant mass reconstruction. This smearing is much larger than Γ for K^0_s, Λ and $D^0$and therefore drives the width of the distribution making the expected pdf to be a Gaussian. A Gaussian profile, however, fails to fit the tails of the distributions as can be seen in figure 4.6. A Voigt profile - which results from the convolution of a Breit-Wigner and a Gaussian pdfs - describes somewhat better the long tails of the distribution but fails in accuracy beyond 1σ. A better fit is found when two gaussians - both sharing the same mean μ, but with different widths - are used. The two-gaussian fit was selected as the nominal pdf for signal extraction, while the other pdfs were used as checks in the hunt for systematic errors. A list of all these pdfs can be found in appendix C

The width of the invariant mass distribution is driven by the momentum resolution of the reconstructed tracks, which could also bias the momentum reconstruction of the decay. It is specially important to be able to reconstruct the momentum of the reconstructed decay with high accuracy, since this analysis is performed differentially in p_T. In order to quantify the *momentum*

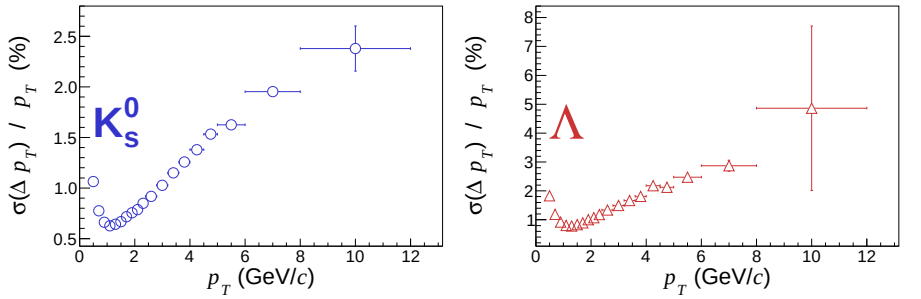

Figure 4.7 Transverse momentum resolution of K^0_s (left) and Λ (right) decays according to Monte Carlo for events in centrality class 10-20%.

resolution, the difference between the reconstructed transverse momentum of the matched candidate and the p_T of the MC particle was computed. The distribution of these differences were fitted with a Gaussian function with width $\sigma(\Delta p_T)$. Figure 4.7 shows the momentum resolution ($\sigma(\Delta p_T)/p_T$) for K^0_s and Λ according to Monte Carlo. As can be seen, the features found in single tracking are inherited in the reconstruction of secondary vertices from its decay into two charged particles. Above 1 GeV/c the resolution grows almost linearly with p_T from 0.6% up to 2% at 8 GeV/c (and slightly higher for Λ). Below 1 GeV/c, the resolution is driven by the material budget and degrades more quickly, however it is not bigger than 2 %, which is much smaller than the binning used.

In this analysis it is desirable to have a high purity sample, however that is not always possible. The stricter the cuts, the better is the signal over background ratio, but also the more particles we loose. The *signal fraction* is quantified from the fit of the invariant mass distribution as the ratio between the signal over signal plus background of reconstructed candidates in a 3σ window around the reconstructed mass μ. The *efficiency* is defined as the ratio between the raw yield and the amount of particles generated. The latter are primaries selected in the same p_T, η and rapidity window.

The signal fraction and efficiency for K^0_s and Λ as a function of transverse momentum extracted from MC are shown in the top panel of figure 4.8. The kinks present in both curves are due to the change in the selection strategy with p_T (reported in table 4.3). The reduction in the overall efficiency below 2 GeV/c is due to the increase in the minimum allowed R_{xy} for those candidates. There is an enhancement in the signal fraction below 1.2 GeV/c when the TPC identification for the daughters of the decay is required. At high p_T the signal fraction reaches a plateau of $\sim$ 85% for both K^0_s and Λ. The signal fraction extracted from data - shown in the lower panel of the figure - presents the

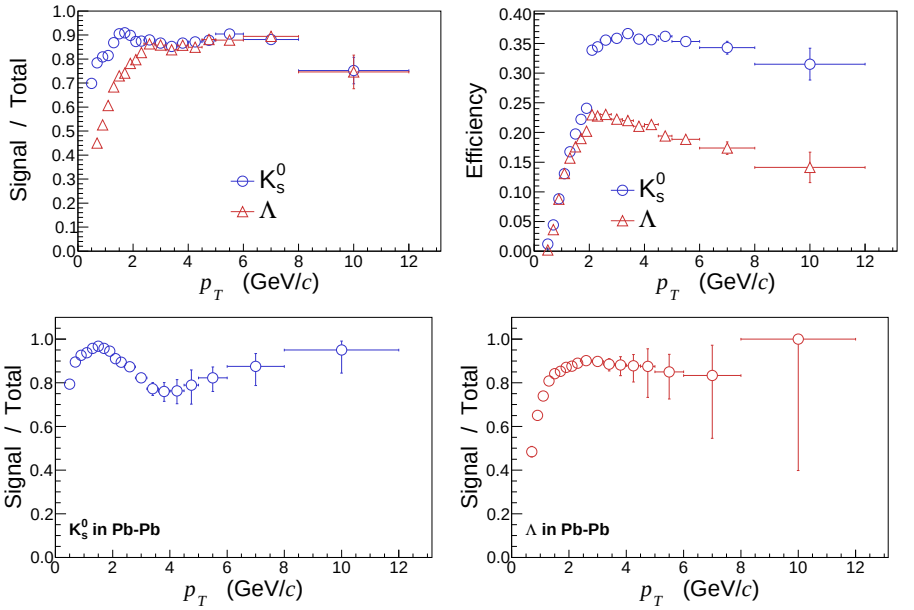

Figure 4.8 Top-left: Signal fraction of K^0_s and Λ candidates selected with the nominal cuts in 0.1 million Hijing events compatible with centrality class 10-20%. Top-right: Efficiency for reconstruction of K^0_s and Λ particles. Bottom-panels: Signal fraction of K^0_s (left) and Λ (right) for Pb–Pb collisions in centrality class 10-20%.

same p_T trend as the one from MC, however an enhancement in the signal fraction below $p_T < 3$ GeV/c with respect to the MC is present in data.

4.5 SIMULTANEOUS FIT OF INVARIANT MASS AND V_2

Since the v_n measurements result from an average over particles of interest and over events, the azimuthal correlation obtained in each mass bin can be decomposed[1] into a signal-like and a background-like set, according to

$$(S+B)\, v_n = S\, v_n^S + B\, v_n^B, \tag{4.3}$$

where S is the set of candidates identified as signal and B is for background candidates.

In this approach, by definition all candidates belonging to the signal-like set have the same ${v_n}^S$, while candidates belonging to the background-like set are allowed have a ${v_n}^B$ that varies smoothly with invariant mass. The latter

[1] It is worth mentioning that this additivity is a result of the definition of v_n - a harmonic decomposition of the azimuthal distribution of particles - and therefore is valid for any method used to calculate v_n.

assumption - supported by the Monte Carlo studies - relies on the fact that that the background is made out of random combination of particles with no sudden change in its chemical composition along W. Thus, as a function of invariant mass, equation 4.3 can be written as

$$v_n(W) = f_S(W)\, v_n^S + f_B(W)\, v_n^B(W), \tag{4.4}$$

where f_S and f_B are the signal-like and background-like fractions, respectively.

The final measurement is obtained with the use of a binned fit to $v_n(W)$ using a linear function for the W dependence of v_n^B and the following integrals:

$$f_S(W) = \int_\Delta \mathrm{d}w \frac{S(w)}{S(w)+B(w)} \qquad f_B(W) = \int_\Delta \mathrm{d}w \frac{B(w)}{S(w)+B(w)} \tag{4.5}$$

where $S(w)$ and $B(w)$ come from the fit of the invariant mass distribution and Δ is the mass bin size in the $v_n(W)$ computation, chosen wide enough to ensure numerical convergence.

Figures 4.9, 4.10 and 4.11 show the invariant mass distribution and $v_2(W)$ for K^0_s, Λ and D^0 candidates, respectively, in several p_T bins for Pb–Pb collisions. The invariant mass distributions for K^0_s and Λ were fitted using a Double-Gaussian probability distribution function for the signal and a second order polynomial for the background. For D^0 candidates, a Gaussian pdf was used for the signal and an exponential function for the background. It is seen that the v_2 is different in the region of the correct mass, which indicates a significantly different value of the real v_2^{sgn} as compared to the relevant ones in the side bands. A large correlation is found for the combinatorial background. This can be attributed to the fact that each particle used in the reconstruction is ultimately correlated with the reaction plane. A background-like candidate acquires azimuthal anisotropy through its daughters. The main features of the measured $v_2(W)$ are persistent for different centrality classes and transverse momentum bins. The mass dependence of v_2 was fitted with equation 4.4.

4.6 STUDY OF SYSTEMATIC BIASES

In this study, the stability of the observables was tested by changing the particle selection strategy and the probability distribution functions used for the signal characterisation. For changes in the selection strategy, the difference (*residuals*) between the observable subject to each variation relative to the nominal measurement is computed for every v_2 method, centrality and p_T bin analysed. No systematic bias which could incur into a correction was found.

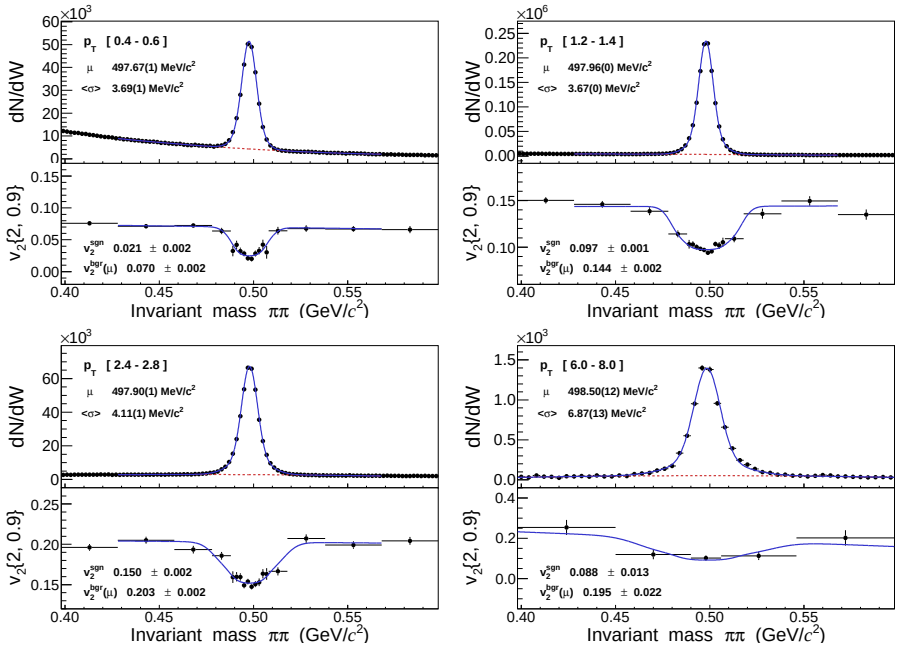

Figure 4.9 Invariant mass and $v_2(W)$ of K^0_S candidates for several p_T bins in Pb–Pb collisions for centrality class 10-20%. The distribution have been fitted using a double-gauss parametrization for the signal and a second order polynomial for the background candidates (solid line). The background only component (dashed lines) result from the interpolation of the background function to the peak region. The mass dependence in v_2 have been fit using equation 4.4.

However potential systematic effects were quantified based on the residuals of quantities for which the observables are expected to be most sensitive and assigned as an additional uncertainty. The summary of this study is presented here.

4.6.1 *Centrality selection*

Inaccuracies in the centrality determination translate into the acceptance of events with smaller or larger azimuthal anisotropy, which would cause a systematic shift in the p_T trend of each observable. Moreover when averaging over events, flow and multiplicity fluctuations would bias each observable differently. Since $v_2\{4\}$ is weighted event-by-event by the fourth power of the multiplicity, this observable would be most affected by outliers in the centrality percentile under study.

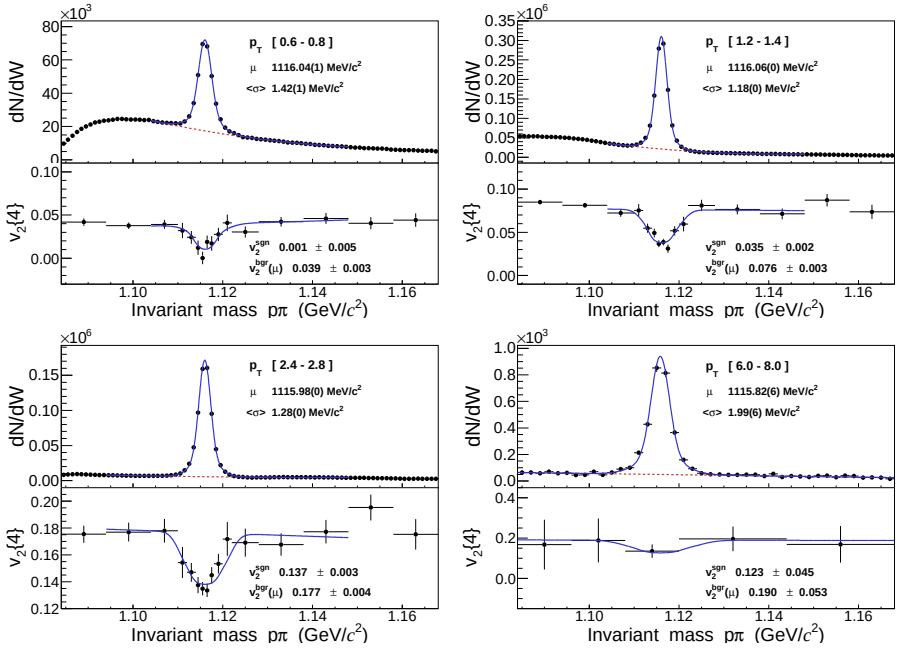

Figure 4.10 Invariant mass and $v_2(W)$ of Λ candidates for several p_{T} bins in Pb–Pb collisions for centrality class 10-20%. The distribution have been fitted using a double-gauss parametrization for the signal and a second order polynomial for the background candidates (solid line). The background only component (dashed lines) result from the interpolation of the background function to the peak region. The mass dependence in v_2 have been fit using equation 4.4.

		00-05	05-10	10-20	20-30	30-40	40-50	50-60
K^0_S	$v_2\{2, 0.0\}$	0.8%	0.7%	0.4%	0.1%	0.1%	0.2%	0.2%
K^0_S	$v_2\{2, 0.9\}$	1.3%	0.8%	0.3%	0.3%	0.2%	0.4%	0.5%
K^0_S	$v_2\{4\}$	–	2.8%	1.0%	0.3%	0.3%	1.8%	1.9%
Λ	$v_2\{2, 0.0\}$	1.1%	0.8%	0.4%	0.1%	0.1%	0.3%	0.3%
Λ	$v_2\{2, 0.9\}$	0.8%	0.8%	0.5%	0.2%	0.2%	0.2%	0.2%
Λ	$v_2\{4\}$	–	2.7%	0.9%	0.6%	0.5%	2.0%	2.0%
D^0	$v_2\{2\}$	–				9.0%		–
D^0	$v_2\{2, 0.9\}$	–				8.8%		–

Table 4.5 Potential bias due to centrality selection in $2.0 < p_{\mathrm{T}} < 2.1$ GeV/c for K^0_S and Λ particles and in $3.0 < p_{\mathrm{T}} < 4.0$ GeV/c for the D^0 meson. The values are expressed as relative percentages of the nominal value.

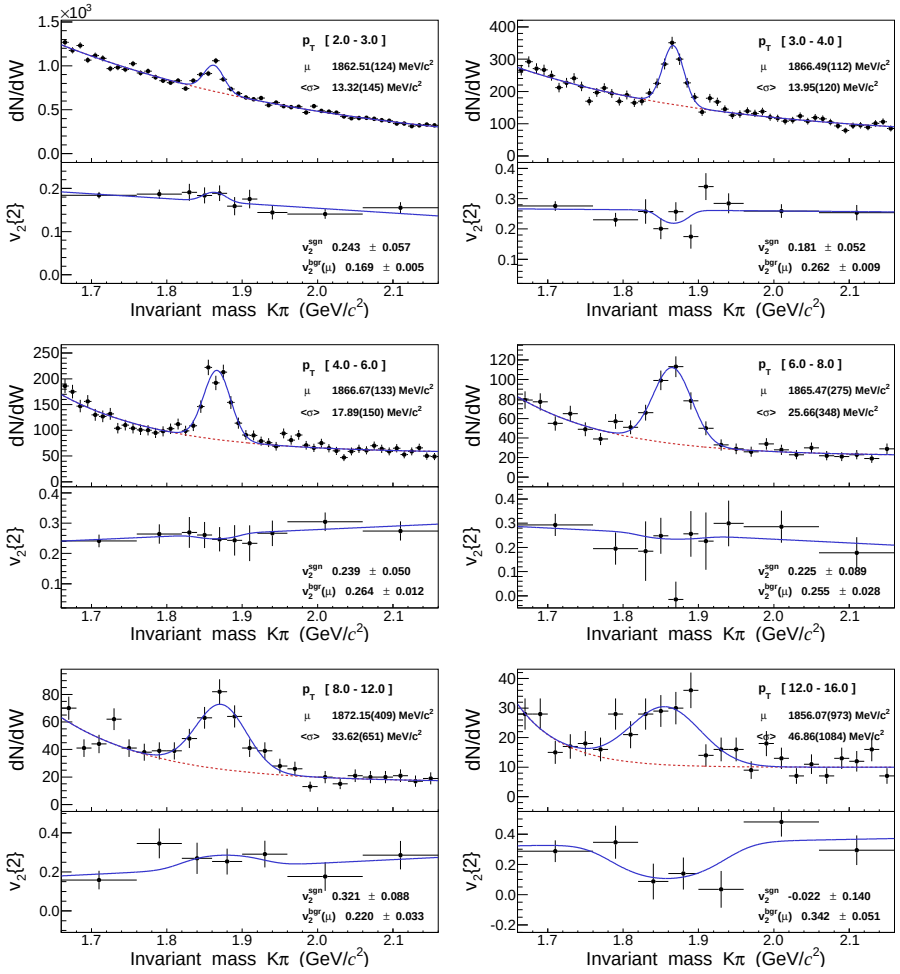

Figure 4.11 Invariant mass and $v_2(W)$ of D^0 candidates for several p_T bins in Pb–Pb collisions for centrality class 30-50%. The distribution have been fitted using a Gauss parametrization for the signal and an exponential function for the background candidates (solid line). The background only component (dashed lines) result from the interpolation of the background function to the peak region. The mass dependence in v_2 have been fit using equation 4.4.

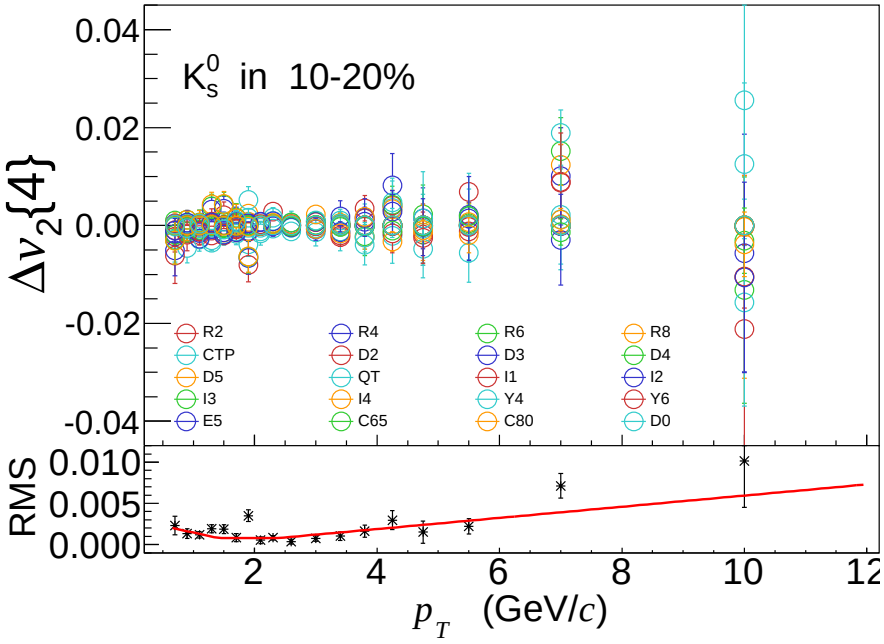

Figure 4.12 Difference between nominal $v_2\{4\}$ and the $v_2\{4\}$ obtained from several changes in the selection strategy as a function of transverse momentum for K^0_s particles in centrality class $10-20\%$.

The stability of the observables to the centrality definition was tested by changing the multiplicity estimator of the events among: i) TPC tracks (TRK), ii) SPD tracklets (CL1), and iii) VZERO signal (VoM). The residuals were found to vary around zero with no trend in p_T which suggests no change in the impact parameter range matched to each centrality class. Since effects due to the flow and multiplicity fluctuations cannot be disentangled from the pure statistical fluctuations, the root mean square (RMS) of the residuals point by point was computed to asses the size of any potential bias in this respect. Table 4.5 shows the relative size of the RMS with respect to the nominal value in percentage for K^0_s and Λ particles in $2.0 < p_T < 2.1$ GeV/c and for D^0 in $3.0 < p_T < 4$ .0 GeV/c. For all of the observables the RMS is found to be driven by statistical fluctuations (growing in p_T regions where the statistics is scarce), larger for $v_2\{4\}$ and very small when compared to the statistical uncertainty.

4.6.2 *Particle selection*

Regarding particle selection, loosening or tightening the parameters governing the reconstruction not only assesses the potential bias in the resolution of the detector but also changes the purity in the sample. The additional change in purity allows us to test the background subtraction procedure described by equation 4.4. It was found that these variations show no systematic effect for any of the observables presented here.

The stability of the observables to changes in the topological selection was tested by varying each variable around the nominal set of cuts. Figure 4.12 shows as an example the residuals for K^0_s $v_2\{4\}$ in centrality class 10-20% for several variations in the selection strategy. The acceptance of the decay candidate and its daughters was changed by varying the pseudo-rapidity (E5) acceptance of the daughter tracks and the pseudo-rapidity and rapidity (Y4, Y6) of the reconstructed candidates. The distance of closest approach between daughters (D2, D3, D4, D5) and the Cosine of the Pointing Angle (CTP) were varied significantly. Additionally for K^0_s and Λ the decay radius (R2,R4,R6,R8) and the cuts for the reflections rejection (QT,KM) were released and tightened, while for D^0 the product of impact parameters (DoDo) and the reflection hypothesis (SW) were changed. Moreover the sensitivity to the quality of the tracks used in the reconstruction are assessed by changing the number of associated TPC (C65,C80) and ITS space points to the track. Additionally, for secondary tracks used in the reconstruction of K^0_s and Λ below 2 GeV/c ITS-refit was required improving additionally the accuracy in the secondary vertex reconstruction (I1, I2, I3, I4). For the three particles, no significant systematic trend was found. As an example, figure 4.12 shows the RMS of the residuals for K^0_s $v_2\{4\}$ as a function of p_T, which in turn is much smaller than the statistical error.

4.6.3 *Signal extraction*

In order to study possible effects from signal extraction several models for the signal and background were tested.

The probability distribution function (pdf) used to model the invariant mass distribution of the signal are: Gauss, Breit-Wigner, Voigt and Double-Gauss. The background was described by a second order polynomial function or an exponential function.

The changes due to the signal extraction were found to be minimal however finite. The uncertainty due to this source was assigned by quantifying the maximum deviation from the nominal signal.

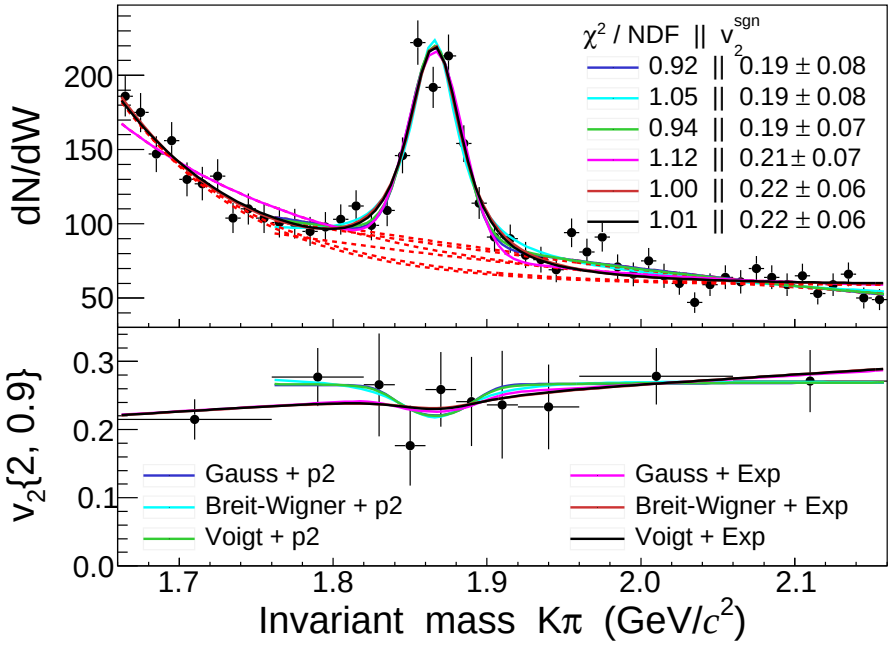

Figure 4.13 Invariant mass (W) distribution and $v_2\{2, 0.9\}$ as function of W for D^0 candidates with $4 < p_T < 6$ GeV/c in centrality class 30-50%. Three models for the signal and two for the background were used to quantify up to six different measurements. The dashed lines represent the backgound model interpolated to the peak region. The normalized χ^2 and the estimation of the v_2^{sgn} is shown in the top right corner.

4.6.4 *Feeddown*

The *raw yield* extracted from the fits as a function of p_T is reported in figure 4.14 (left). The raw yield includes not only primary particles, but also secondaries coming from production in material or particles with an ancestor produced in the collision. The latter is called *feeddown*. Based on the selection strategy, and according to the Monte Carlo, almost all of our contamination from secondaries comes from feeddown. The latter comes mostly from very specific channels.

ϕ	$\rightarrow$	$K^0_S + K^0_L$	$\Gamma_i/\Gamma_{tot} = 34\%$
Ξ	$\rightarrow$	$\Lambda + \pi$	$\Gamma_i/\Gamma_{tot} = 99\%$
B mesons	$\rightarrow$	$D^0 + X$	$\Gamma_i/\Gamma_{tot} = 8\%$

The amount of feeddown present in the samples depends on the selection strategy. For K^0_s and Λ, the reconstructed candidates matched to a MC truth were followed backwards towards the primaries. By doing this, the computed

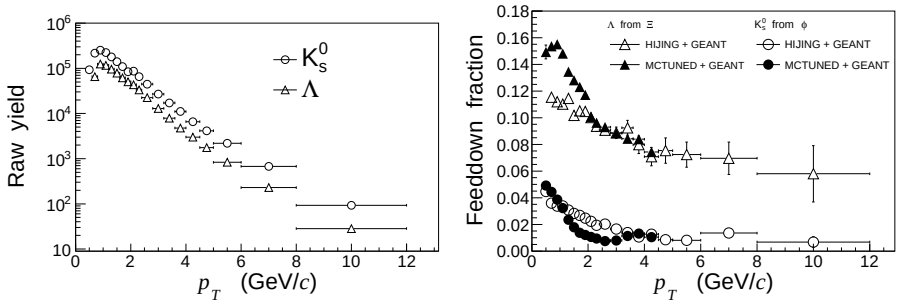

Figure 4.14 Left: Raw yield of K^0_s and Λ particles selected using the nominal selection in 0.1 million Hijing events compatible with centrality class 10-20%. Right: Fraction of particles coming from feedown.

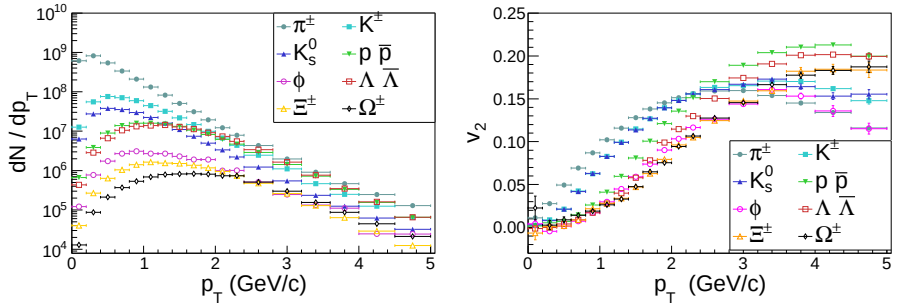

Figure 4.15 Left: Number of particles generated in the acceptance for all the species simulated in the MCTUNED sample. Right: v_2 of the particles generated by the MCTUNED Monte Carlo. These figures correspond to Monte Carlo events for centrality class 10-20%.

fraction includes efficiency and acceptance of the selections used, but relies on the ability of HIJING to correctly account for the multiplicity, particle ratios and their centrality dependence relative to what is measured experimentally. HIJING was found to be deficient in the description of particles produced at low transverse momentum. The strategy used here was to complement HIJING with another Monte Carlo sample. This Monte Carlo - called MC-TUNED - was built using as input the spectra of identified $\pi^\pm$, $K^\pm$, K^0s, p, $\bar{p}$, Λ, $\bar{\Lambda}$, ϕ $\Xi^\pm$, $\Omega^\pm$ published by ALICE [58–60]. These particles were injected with a v_2 and v_3 profiles that mimic the ones obtained from preliminary results. The particles introduced were let to decay in their respective channel while propagating through the ALICE central detectors. Figure 4.15 shows the spectra (left) and v_2 (right) of identified particles injected into 0.1 million Monte Carlo events for centrality class 10-20%.

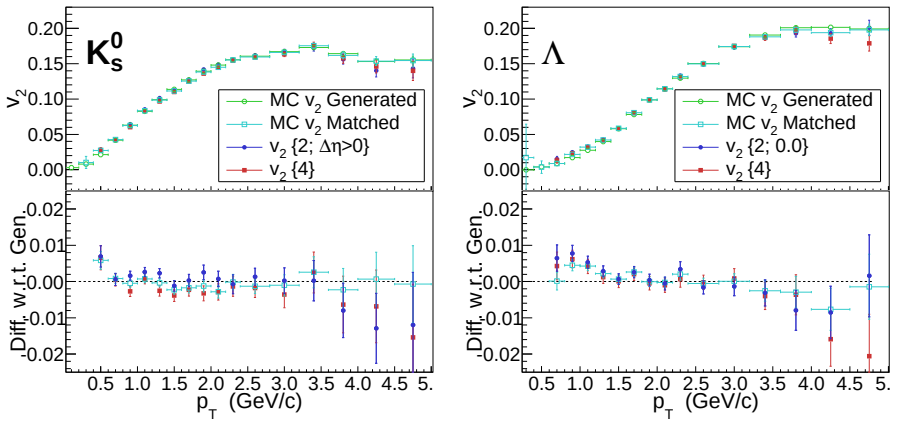

Figure 4.16 Comparison between the v_2 of generated particles (open circles) and those reconstructed by the ALICE detector using the nominal selection (open squares). The solid markers correspond to the measurements using either the ScalarProduct or the Q-Cumulants methods by performing a background subtraction for the reconstructed candidates as done for data. These figures correspond to Monte Carlo events for centrality class 10-20%.

Figure 4.14 (right) shows the fraction of feeddown expected from ϕ to K^0_s and $\Xi^{\pm}$ to Λ. The fraction of Λ from Ξ is found to be slightly below 16% at low transverse momentum, decreasing with increasing p_T and reaching below 10% at 3 GeV/c. The fraction of K^0_s from ϕ is much smaller, but with similar trend in p_T going from 5% in the lowest reconstructed p_T down to below 2% at 3 GeV/c. Due to decay kinematics one expects that the K^0_s coming from ϕ scales by two $v_2^K(0.5 * p_T) = v_2^{\phi}(p_T)$, while for the Λ coming from Ξ, the scaling would be less strong. This would regulate the feeddown yield leaving a somewhat different percentage for the v_2.

Figure 4.16 shows the comparison among the flow of primaries generated in the acceptance (green), the flow of reconstructed particles (cyan) and the measured flow using $v_2\{2, 0.0\}$ and $v_2\{4\}$ (blue and red, respectively). The bottom panel shows the ratio of each value with respect to the primary particles generated in the acceptance. The results show not only that within errors the measurements reproduce the true flow value, but also that the effective effect from contamination (difference between green and cyan) is negligible for all particles in most p_T bins.

For D^0 the procedure followed was different since full simulation of D and B hadrons is impractical. The expected spectra of B particles decaying into D^0 were estimated using the cross section of produced B particles in pp collisions from a pQCD calculation scaled to Pb–Pb at centrality $30 - 50\%$, using the

assumption that the R_{AA} of B mesons is between 2 to 3 times the one from D mesons.

The fraction of D^0 from B mesons in the selection is defined as the following ratio

$$f_b = \frac{N^{RAW}_{B\to D^0}}{N^{RAW}_{D^0}}, \tag{4.6}$$

where the denominator is the amount of D^0 particles selected during the analysis and the numerator quantifies the amount of those that come from B decays. This last quantity can be written in terms of the R_{AA} (eq. 1.1) as

$$f_b = \frac{R^{B\to D^0}_{AA}}{N^{RAW}_{D^0}} \times \langle T_{AA} \rangle \, (\Delta y \Delta p_T) \, \frac{d^2\sigma^{FONLL}_{B\to D^0}}{dy dp_T} \, (Acc \times \epsilon)^{EVGen}_{B\to D^0} \, B.R. \, N_{ev} \tag{4.7}$$

where the spectra $dN^{B\to D^0}_{AA}/dp_T$ has been decomposed further. The acceptance and efficiency effects of the cuts used were included in the computation of f_b using a Monte Carlo model for the decay kinematics called EvtGen [61] and the cross section for pp events was computed using FONLL. The resulting factor f_b was found to be around 18% in the entire p_T range.

Since we do not know the v_2 of particles with bottom content, the assumption that this value ranges from 0 to the measured v_2^c was taken. Thus the largest deviation expected comes from the case when $v_2^b = 0$. This would correspond to an increase of the measured v_2 as $v_2^{c\prime} \to v_2^c/f_b$.

Results and discussion

5

5.1 K^0_S AND Λ DIFFERENTIAL V_2

Three different estimates ($v_2\{2, 0.0\}$, $v_2\{2, 0.9\}$ and $v_2\{4\}$) of the v_2 for K^0_s and Λ as function of transverse momentum and centrality class are presented in figures 5.1, 5.2 and 5.3, respectively. Even though these three methods have different sensitivities to non-flow and flow-fluctuations, as was discussed in chapter 3, they present many similarities. Both K^0_s and Λ v_2 show a quick build-up with p_T reaching a maximum at different p_T values: ~ 3 GeV/c for K^0_s and ~ 4 GeV/c for Λ. Beyond each maximum v_2 decreases slowly towards a small, however non-zero, value of anisotropy.

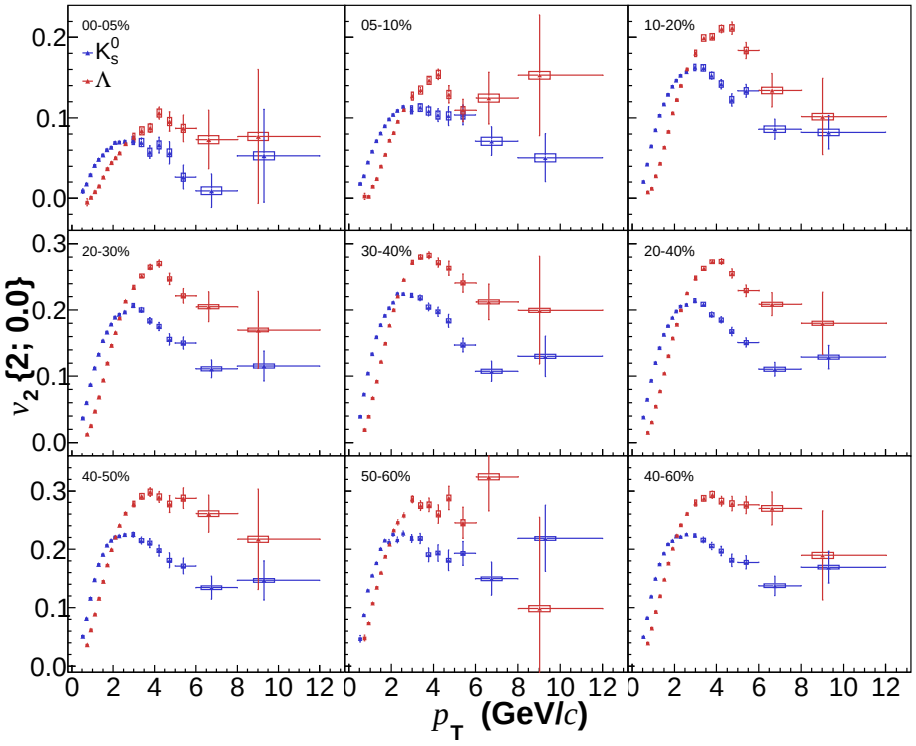

Figure 5.1 $v_2\{2, 0.0\}$ for K^0_s and Λ as a function of transverse momentum and its evolution with centrality.

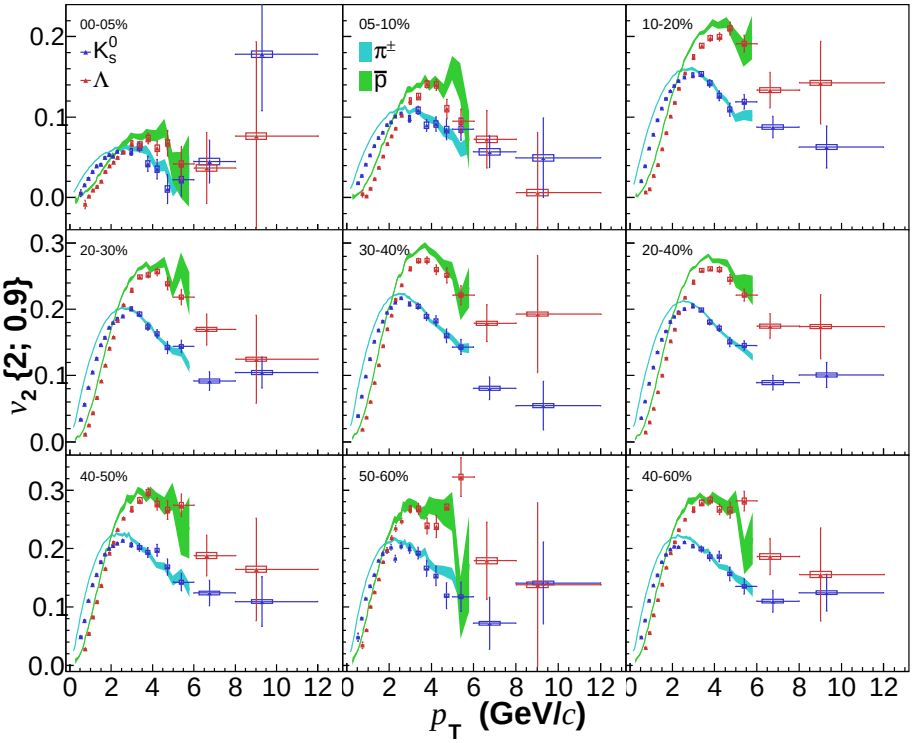

Figure 5.2 $v_2\{2, 0.9\}$ of K^0_S and Λ as a function of transverse momentum and its evolution with centrality. The results for pions and protons, extracted from [26], show the comparison with particles with no strange flavour.

In addition, a small v_2 is present in the most central class 0-5%. For all other centralities v_2 increases as the collisions become more peripheral. The inclusion of the pseudo-rapidity gap of $\Delta\eta > 0.9$ (shown in figure 5.2) leads to a considerable reduction in v_2. This difference is expected to be due to a reduction in the amount of non-flow. As can be seen in figures 5.2 and 5.3, $v_2\{4\}$ is even smaller than $v_2\{2, 0.9\}$ for all centralities, but shows the same trend with p_T. These characteristics were also found in the v_2 of charged particles [49, 62] at the same collision energies.

The results for $v_2\{2, 0.9\}$ of pions and protons[1] are shown in figure 5.2. Below 2 GeV/c, v_2 shows a mass hierarchy: the bigger the mass of the species is the lower its v_2. Between $2 < p_T < 5$ GeV/c, v_2 of the different species seems to group based on their number of constituent quarks, i.e. mesons vs baryons. Both features were also found in the v_2 of identified particles at lower beam energies and reported by PHENIX and STAR [15, 34–46, 63–65], where

[1] Both published in [26], where part of the results obtained in this analysis was also reported.

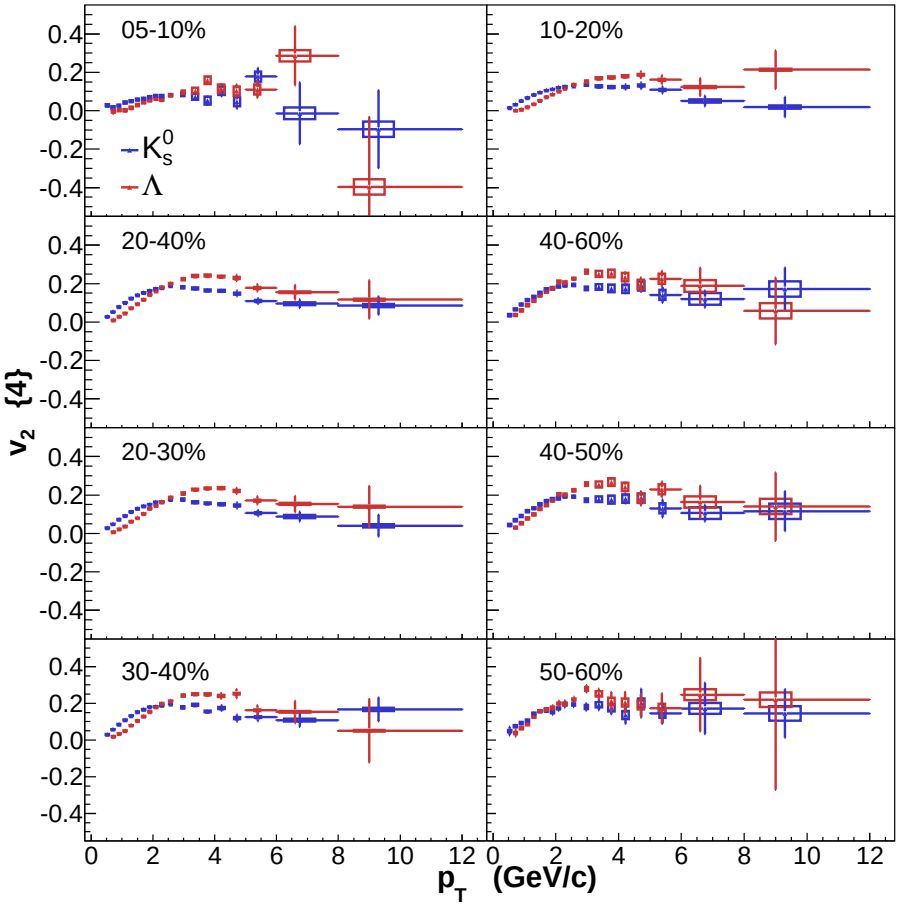

Figure 5.3 $v_2\{4\}$ of K^0_s and Λ as a function of transverse momentum and its evolution with centrality.

the observed mass hierarchy was reproduced by hydrodynamics assuming a radial expansion of the medium in the QGP phase.

5.2 PSEUDO-RAPIDITY SEPARATION IN $V_2\{2\}$

As indicated also before, $v_2\{2\}$ is sensitive to non-flow from two particle correlations. This non-flow arises from correlations of the products of a decayed Hyperon or the fragments of a jet involving a K^0_s or Λ in their final state. In such context, one naively expects that the non-flow component present in $v_2\{2\}$ varies with the relative abundance of different species, that is, a variation with centrality and transverse momentum is expected.

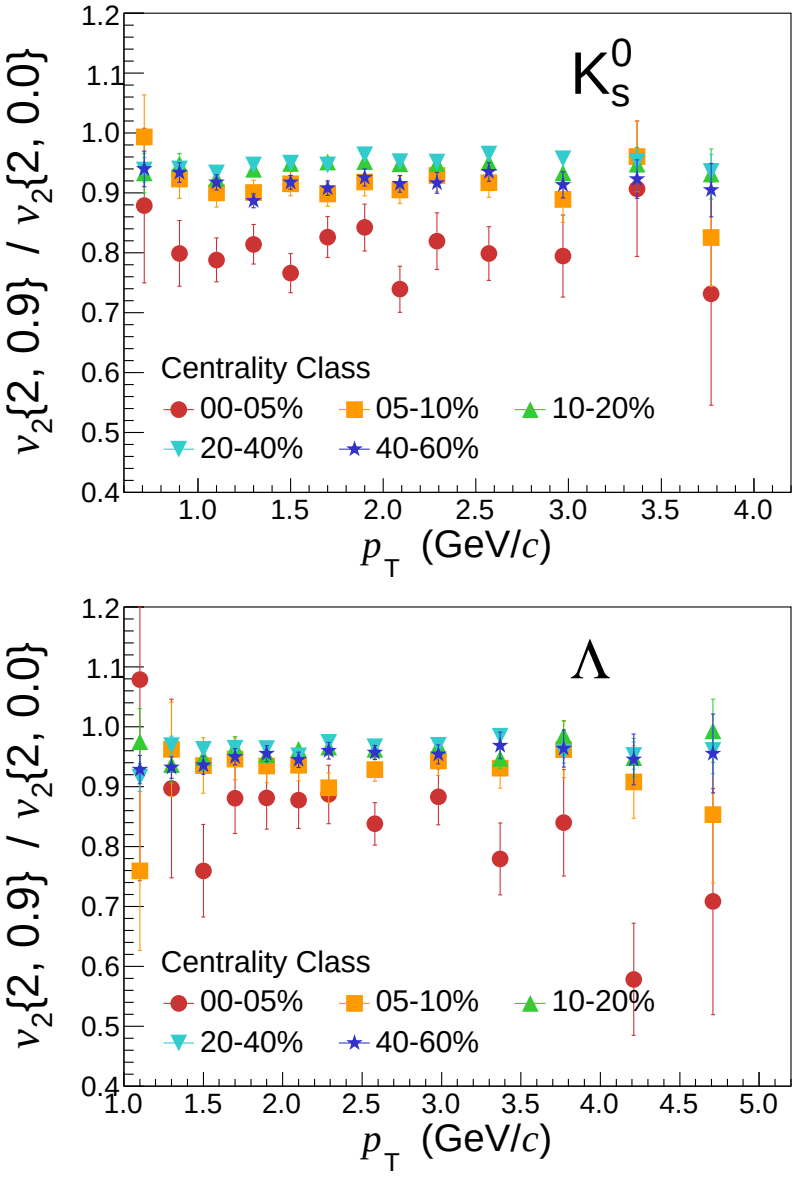

Figure 5.4 Ratio between $v_2\{2, 0.0\}$ and $v_2\{2, 0.9\}$ for K^0_s (top) and Λ (bottom) in several centrality classes.

A suppression of non-flow is enforced in the observable by the requiring a pseudo-rapidity separation between the particles being correlated. The observable $v_2\{2, 0.0\}$ correlates particles with rapidity in the range of $-0.8 < \eta < 0.0$ with particles with rapidity in the opposite range $0.0 < \eta < +0.8$, thus suppressing effectively most of the non-flow contribution. A stronger suppression is achieved with $v_2\{2, 0.9\}$ which correlates particles in the central rapidity range $-0.8 < \eta < +0.8$ with those at forward rapidity, $-3.7 < \eta < -1.7$ and $2.8 < \eta < 5.1$. The relative difference between these two observables is quantified by the ratio of $v_2\{2, 0.9\}$ over $v_2\{2, 0.0\}$. Figure 5.4 shows the ratio for the v_2 of K^0_s (top panel) and Λ (bottom panel) as function of p_T in several centrality classes.

A small value of the ratio corresponds to a strong residual non-flow component in $v_2\{2, 0.0\}$. Even though we have little knowledge of the actual mechanisms that generate non-flow in these large p_T ranges, the fact that this ratio shows little variation with transverse momentum is quite striking. Since $v_2\{2, 0.0\}$ and $v_2\{2, 0.9\}$ grow proportional to each other, it seems that the introduction of a stronger gap, namely $\Delta\eta > 0.9$, suppresses a component in the correlation that relates to the overall flow. Two effects could be responsible for this observation: 1) a reduction of the event by event fluctuations in our observables when a pseudo-rapidity gap is increased or 2) a rotation of the flow angle is present as we move forward in rapidity. These effects are currently being discussed [66] and investigated.

The ratios show also that the relative size of such component is quite considerable. Depending on centrality, it can account for between 5% to 20% of the v_2 even at low transverse momentum ($p_T < 2.0$ GeV/c) where collective effects are expected to dominate the particle production.

5.3 FLOW FLUCTUATIONS

Assuming that $v_2\{2, 0.9\}$ and $v_2\{4\}$ are free of non-flow, one can estimate the relative size of the flow fluctuations arising from eccentricity fluctuations in the initial geometry by combining both measurements into $\sigma_2^{BG}/\langle v_2 \rangle$ using equation 3.19. We are here concerned about the relative flow-fluctuation arising from Bessel-Gaussian fluctuations of the spatial eccentricity as studied in [11]. An estimate of fluctuations is provided in each centrality class using both K^0_s and Λ data independently.

In figure 5.5, I quantify the relative fluctuations $\sigma_2^{BG}/\langle v_2 \rangle$. The size of the v_2 fluctuations is in the range of 30% to 50% of the average v_2 and shows no significant p_T dependence. Moreover, the size of event by event fluctuations in the v_2 is equal within uncertainties for both K^0_s and Λ in each centrality class.

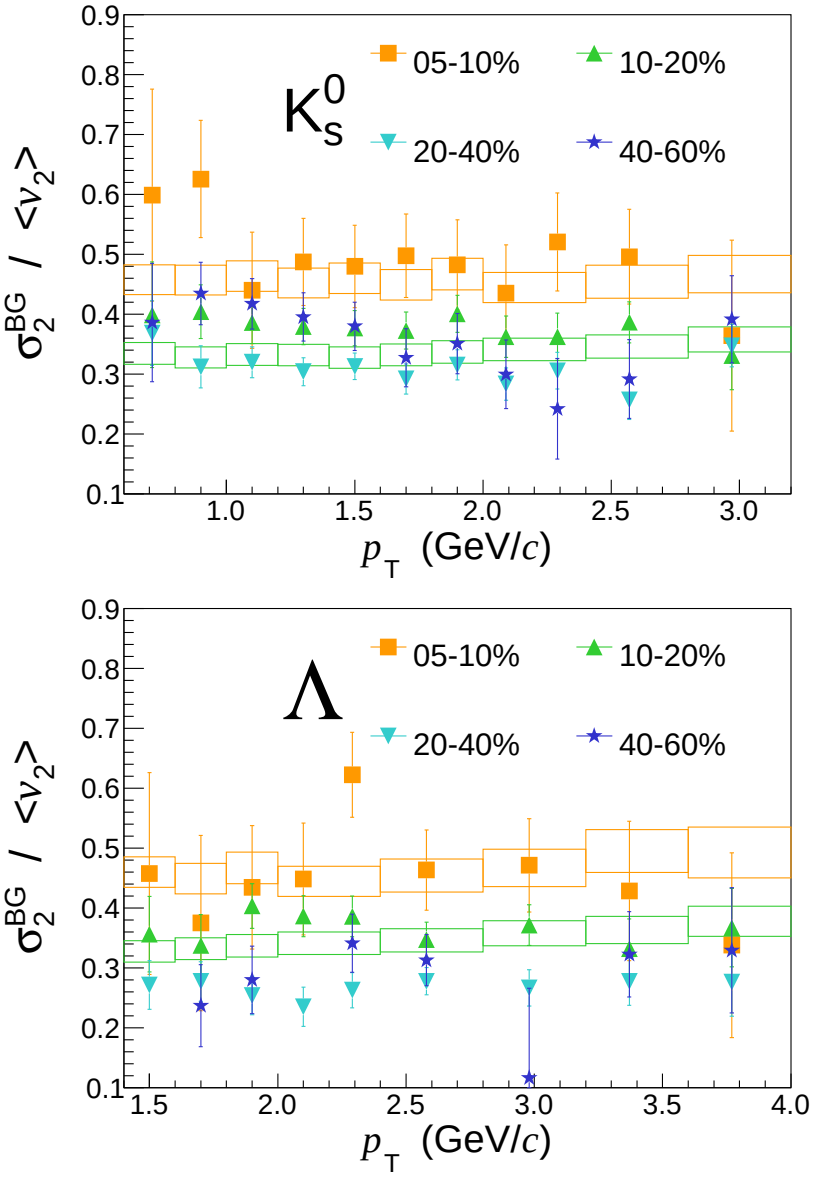

Figure 5.5 Estimate of relative flow fluctuations $\sigma_2^{BG} / \langle v_2 \rangle$ as computed from equation 3.19 for K^0_s (left) and Λ (right) in several centrality classes. The same observable computed for charged particles in centrality classes 05-10% and 10-20% extracted from [62] is shown with coloured boxes.

Figure 5.5 shows also a small variation with centrality class indicating that for the most central collisions the relative fluctuations are more pronounced. For those centralities, the size of the relative fluctuations becomes so large that the assumption on $\sigma/v_n \ll 1$ is no longer justified and higher order corrections should be included in the derivations of 3.17 and 3.18. The results are compared to those for all charged particles reported in [62] and provide evidence that this observable is independent of constituent quark composition or particle charge. Both are strong arguments in favour of an observable that depends solely on the initial state effects.

5.4 HYDRODYNAMIC V_2

It has been shown that the medium produced in heavy-ion collisions at RHIC exhibits a behaviour compatible with that of a strongly coupled plasma that flows like a liquid [67, 68]. In such context, the dynamics of the QGP phase can be described macroscopically by hydrodynamics. The motion of matter is governed by the pressure gradients formed in the medium. The anisotropy of the initial state is translated into the anisotropy of the momentum distribution of the particles after the evolution of the medium.

The most significant transport parameter for the build up of the flow coefficients v_n is the *specific shear viscosity* (η/s). In general terms the smaller the shear viscosity, the smaller the in-medium dissipation and the larger the development of v_n [69, 70]. It was shown that a small η/s coefficient characterises better the strongly coupled plasma created in heavy-ion collisions. Theoretical calculations set a lower bound in the value of η/s even in the limit of infinitely strong coupled matter at $\eta/s \geq 1/4\pi$ [71, 72]. The values for the medium found at RHIC and LHC energies are smaller than three times this limit.

Moreover since radial flow pushes matter radially with a common velocity, there is a distinctive mass hierarchy in the transverse momentum of the particles produced [11].

5.4.1 *The VISHNU model*

The VISHNU model [73] uses a causal viscous hydrodynamic description in order to characterise the evolution of the system in the QGP phase coupled to a microscopic hadronic transport algorithm to account for the dynamics after the phase transition.

The hydrodynamic model is called VISH2+1 [74], which stands for Viscous Israel-Stewart [75] Hydrodynamics in (2+1)-dimensions. The hydrodynamic

evolution is set by using the equation of state s95p-PCE [76], which establishes the relationship between pressure, energy and entropy density in the deconfined QGP phase based on Lattice QCD computations [77] at high temperatures and on the hadron resonance gas at low ones.

It was found in [73, 78] that η/s between 0.20 and 0.24 fits better the centrality evolution of $v_2\{4\}$ for charged particles, however the model presented here [79] was tuned to use a lower $\eta/s = 0.16$[2]. The initial eccentricity is obtained by the Colour-Glass-Condensate (MC-KLN [81]) model from where the initial entropy density profile is estimated. In this version of VISHNU, the initialisation time t_0 is set to 0.9 fm/c so that the p_T hadron multiplicity density and the spectra of charged hadrons below 2 GeV in the most central collisions are well reproduced [79].

The hadronic transport model is called UrQMD [82, 83], which stands for Ultra-relativistic Quantum Molecular Dynamics. Within this model the system evolves through a sequence of binary collisions and particles are decayed using vacuum cross sections. The transition from VISH2+1 to UrQMD occurs at a fixed *switching temperature* $T_{SW} = 165$ MeV, which has been established as the optimal temperature for both descriptions (micro and macro) to hold and it is close to the theorised critical temperature T_c of the phase transition. It was found in [84] that the elliptic flow and spectra are not sensitive to reductions in t_{SW} up to $\sim 30\%$. The coupling between the two phases requires the conversion from an isothermal freeze-out surface to the hadron spectra and it is extensively described in [84].

5.4.2 *Comparison with the VISHNU model*

Figures 5.6, 5.7, 5.8 and 5.9 shows the differential v_2 for K^0_s and Λ in several centrality classes compared with VISHNU computations. The p_T differential $v_2\{2, 0.9\}$ of pions and protons extracted from [26] is also shown for reference. The range of transverse momentum considered stops at 2.8 GeV/c. However it is expected that above 2 GeV/c other production mechanisms take over gradually and the hydrodynamic picture breaks down. It is worth noticing that VISHNU computes the $\langle v_2 \rangle$ and therefore should be contained within the band made by $v_2\{2, 0.9\}$ and $v_2\{4\}$ as discussed in chapter 3.

In every centrality class, the differential v_2 presents mass scaling, i.e. the heavier the particle, the lower its v_2. This feature is expected from the hydrodynamic expansion. The mass scaling in v_n can be affected by re-scattering af-

[2] Another important transport parameter is the relaxation time τ_π which was set to $0.5\tau^B_\pi$, where $\tau^B_\pi = 6(\eta/s)/T$ correspond to a classical weakly coupled massless Boltzman gas. However studies in [74] show that, in the limit where no viscous effects [80] δf are considered, this parameter has little influence in the anisotropic flow of the system.

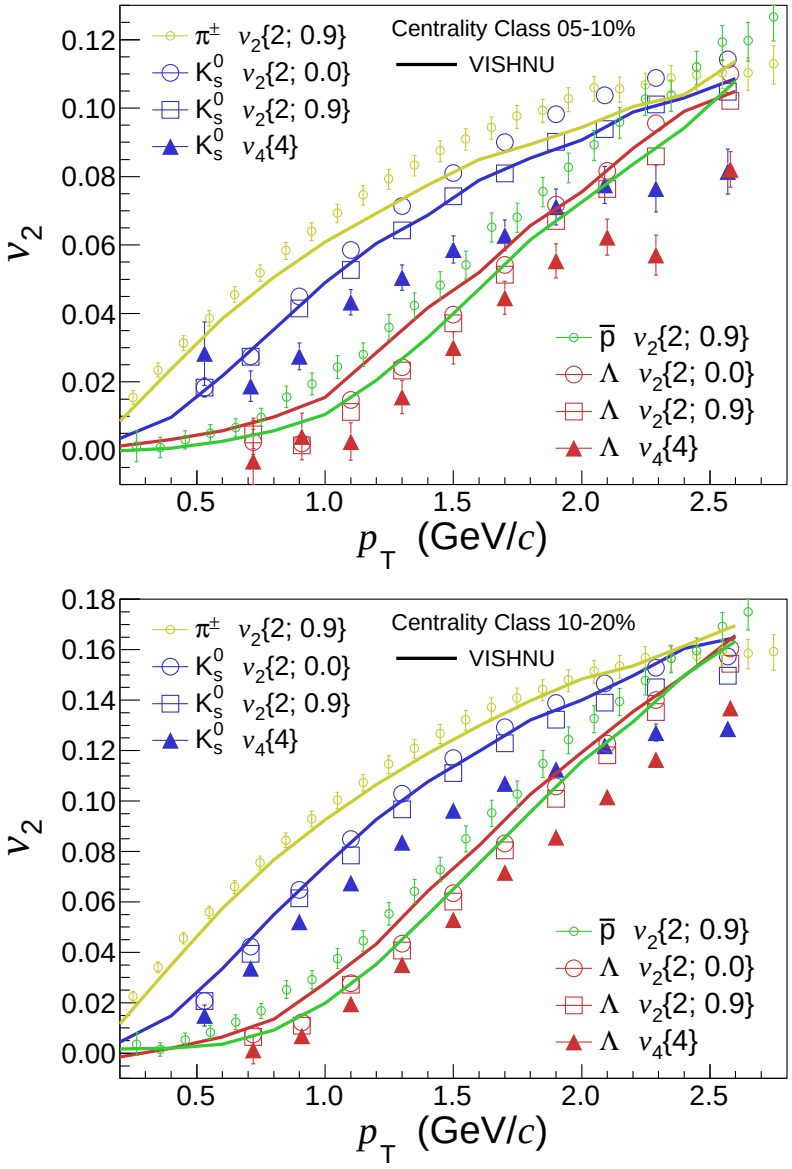

Figure 5.6 p_{T} differential v_2 of $\mathrm{K}^0_{\mathrm{s}}$ and Λ at low transverse momentum compared to the VISHNU model for centrality classes 05-10% and 10-20%. Three methods for the v_2 estimate are used. Each method has different sensitivity to non-flow and flow-fluctuations. The results for pion and proton $v_2\{2, 0.9\}$ extracted from [26] are also shown. The solid lines represent the values computed by VISHNU.

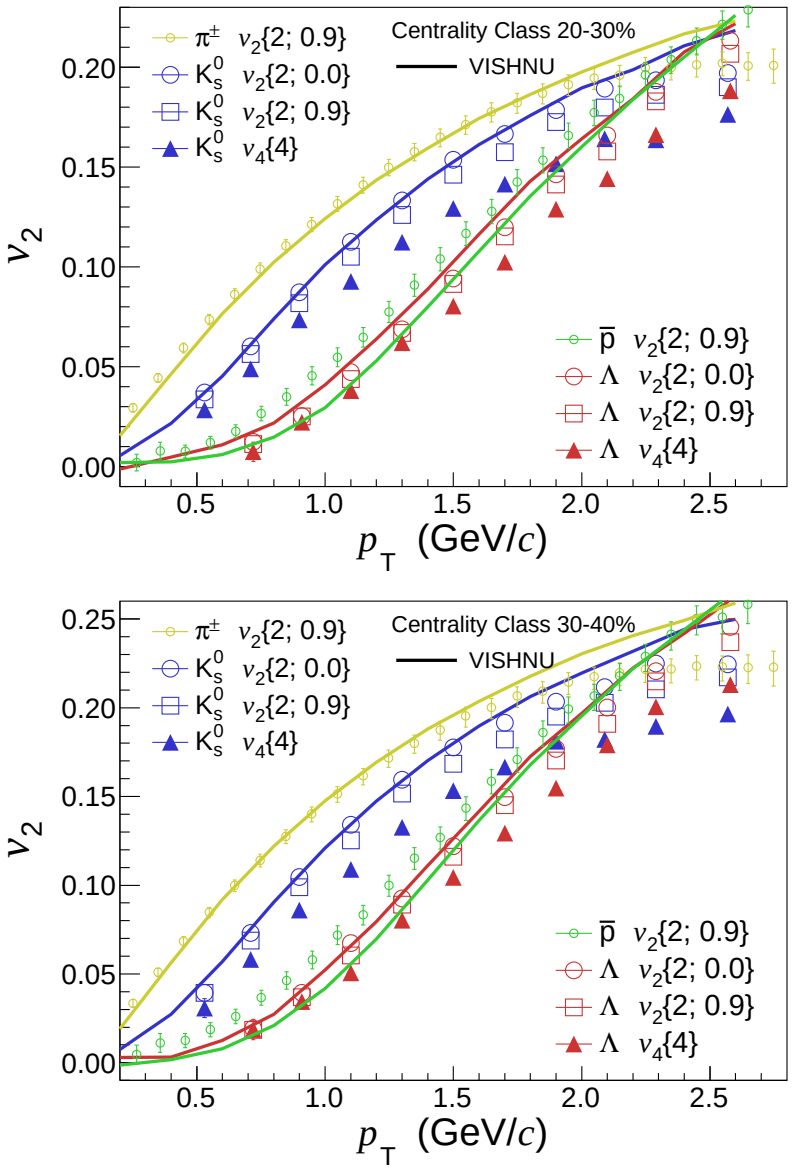

Figure 5.7 p_{T} differential v_2 of $\mathrm{K}^0_{\mathrm{s}}$ and Λ at low transverse momentum compared to the VISHNU model for centrality classes 20-30% and 30-40%. Three methods for the v_2 estimate are used. Each method has different sensitivity to non-flow and flow-fluctuations. The results for pion and proton $v_2\{2, 0.9\}$ extracted from [26] are also shown. The solid lines represent the values computed by VISHNU.

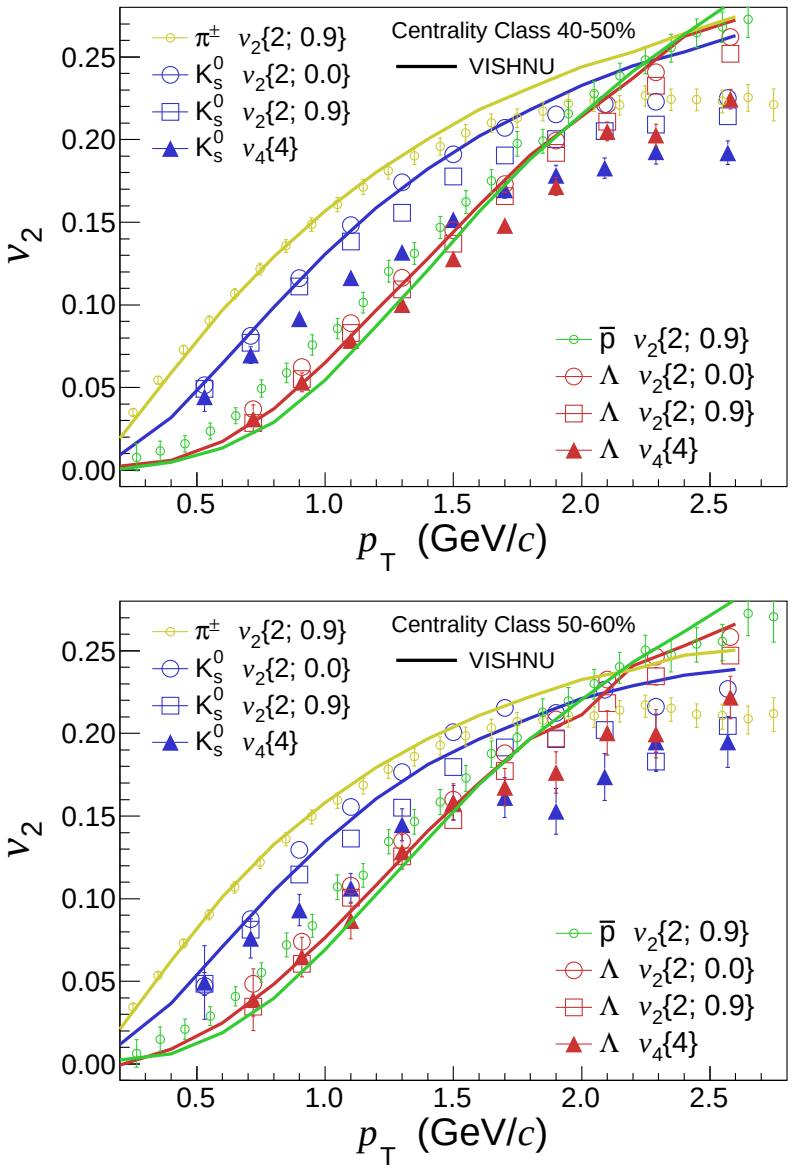

Figure 5.8 p_{T} differential v_2 of $\mathrm{K}^0_{\mathrm{s}}$ and Λ at low transverse momentum compared to the VISHNU model for centrality classes 40-50% and 50-60%. Three methods for the v_2 estimate are used. Each method has different sensitivity to non-flow and flow-fluctuations. The results for pion and proton $v_2\{2, 0.9\}$ extracted from [26] are also shown. The solid lines represent the values computed by VISHNU.

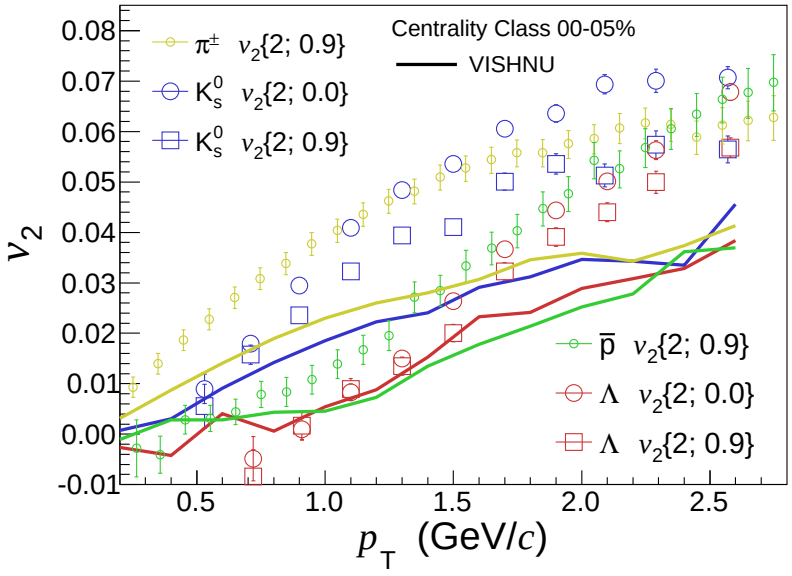

Figure 5.9 p_T differential v_2 of K^0_s and Λ at low transverse momentum compared to the VISHNU model for centrality class 00-05%. Two methods for the v_2 estimate are used. Each method has different sensitivity to non-flow and flow-fluctuations. The results for pion and proton $v_2\{2, 0.9\}$ extracted from [26] are also shown. The solid lines represent the values computed by VISHNU.

ter the chemical freeze-out which depends on the cross section of each species. VISHNU predicts that as a result of re-scattering in the hadronic phase the proton v_2 decreases much more than the v_2 of other species, changing effectively the mass ordering. This behaviour, however, is not found in data.

For centrality classes above the 05% percentile (b-g), this tune of VISHNU is compatible with our measurements for $\pi^{\pm}$ and K^0_s. However the computation lies on top or slightly above K^0_s $v_2\{2, 0.9\}$. For Λ v_2 in centrality classes from 05% to 20% (b,c) the VISHNU computations are well above the measurements, while getting closer for most peripheral centralities (d,e,f,g). The situation is the opposite for protons where VISHNU systematically underestimates the v_2 of protons.

The comparison suggests that the evolution in the hadronic phase plays a stronger role in the development of v_2 than modelled and/or the chosen value for the specific shear viscosity η/s was too small to properly describe the hydrodynamic expansion.

Moreover, for centrality class $00 - 05\%$ (a), the $v_2\{2, 0.9\}$ as function of transverse momentum is found to be persistently larger than the one pro-

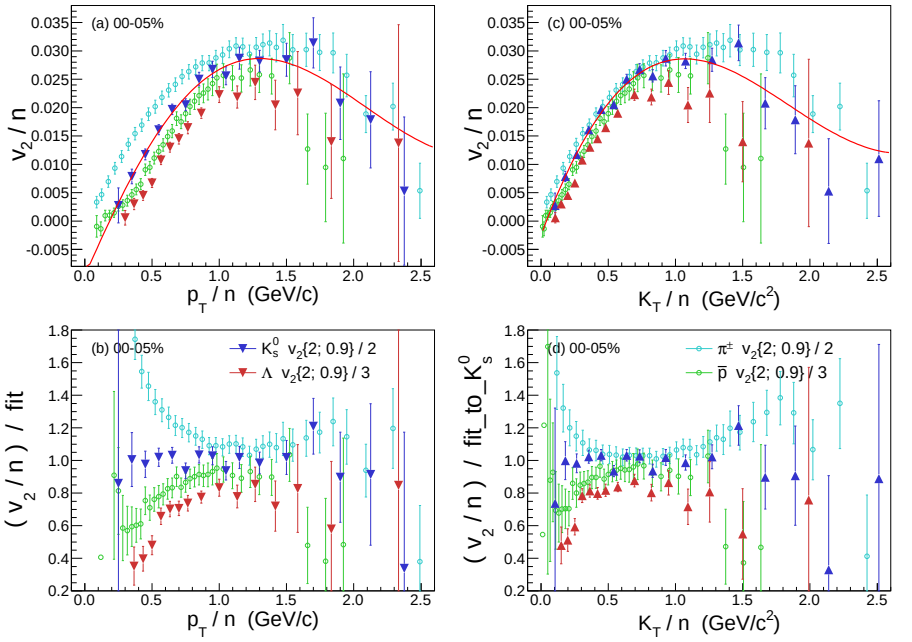

Figure 5.10 $v_2\{2, 0.9\}$ of K^0_s and Λ scaled to their number of constituent quarks in centrality class $00 - 05\%$.

duced by VISHNU. It is worth pointing out that the VISHNU model does not incorporate the multiplicity distribution that we have in data for every centrality class, which can play an important role in the determination of v_2 specially at most central collisions.

5.5 COALESCENCE OF CONSTITUENT QUARKS

At intermediate p_T, i.e. for $2 < p_T < 5$ GeV/c, the v_2 shows a particular behaviour. The v_2 reaches a plateau or saturation that seems to depends strongly the number of constituent quarks of each species as can be seen in figure 5.2. It is worth remarking that this plateau shows little dependence to the species' charge, or the flavour of its valence quarks. This phenomenon was also seen at RHIC energies, where hadronisation models based on quark coalescence or recombination were proposed as the main hadron formation mechanism [46, 85–87]. These models rely on the assumption that constituent quarks degrees of freedom are present before hadronisation occurs, therefore the fact that the data scale as the model predicts supports the formation of a deconfined state.

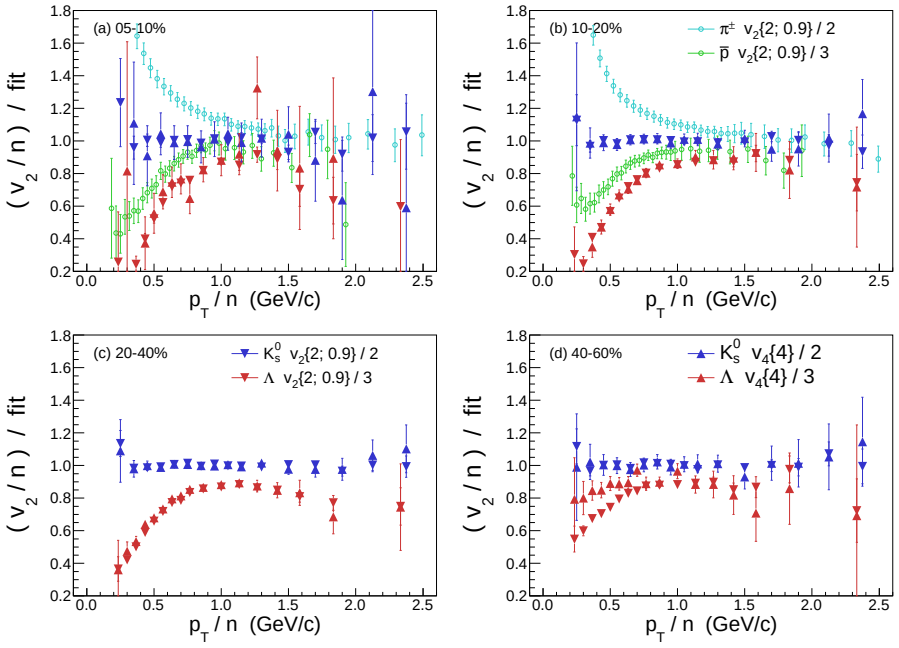

Figure 5.11 $v_2\{2, 0.9\}$ and $v_2\{4\}$ of K^0_s and Λ scaled to their number of constituent quarks as function of scaled transverse momentum for several centrality classes.

5.5.1 *Hadronization via Coalescence / Recombination*

Production via the quark coalescence mechanism is expected to be stronger in the transverse momentum range between ~ 2 to ~ 5 GeV/c, that is below the p_T where independent fragmentation dominates. However there is little insight on where and how rapid this transition occurs.

Quark coalescence models have successfully described hadron production at RHIC energies in the intermediate transverse momentum region [46, 85, 88]. Besides, results on v_2 for identified particles at those energies show a good agreement of meson and baryon v_2 when scaled to their number of constituent quarks [37, 41]. The results presented in the previous articles provided experimental arguments for the restoration of parton degrees of freedom in the expanding QCD matter created at RHIC.

5.5.2 *Parton v_2 assessment*

Figure 5.10(a) shows $v_2\{2, 0.9\}$ of $\pi^{\pm}$, K^0_s, protons and Λ in centrality class $00-05\%$ scaled by their respective number of valence quarks. Beyond $p_T/n_q > 1.0$ GeV/c, the scaled v_2 for the four species come close to each other. At lower

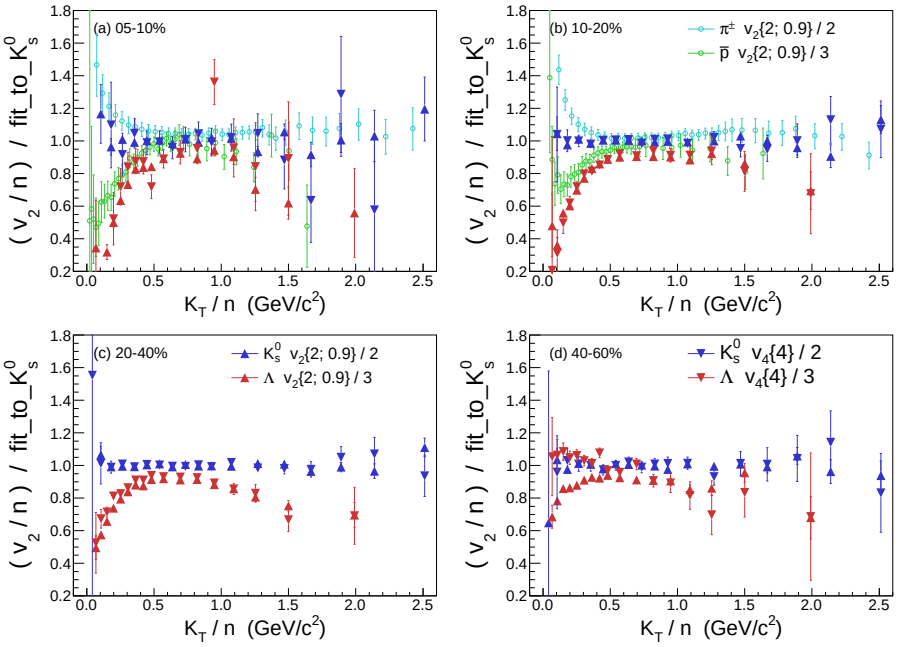

Figure 5.12 $v_2\{2, 0.9\}$ and $v_2\{4\}$ of $\pi^{\pm}$, protons, K^0_s and Λ scaled to their number of constituent quarks as function of scaled transverse kinetic energy for several centrality classes. $\pi^{\pm}$ and protons $v_2\{2, 0.9\}$ were extracted from [26].

scaled p_T the mass ordering from hydrodynamics breaks down the scaling. In order to extend the scaling to lower p_T, another scaling variable was proposed [46]: transverse kinetic energy. The transverse kinetic energy for each species can be obtained from $K_T = \sqrt{m^2 + p_T^2} - m$, where m is the rest mass of the species under consideration. Figure 5.10 (b) shows v_2/n as a function of the scaled transverse kinetic energy. Under this scaling, the data show a better agreement at low transverse momentum.

In order to quantify the accuracy of the scaling, the ratio between the scaled v_2 for all species to the scaled K^0_s v_2 was considered. A fifth order polynomial function was fitted to the scaled K^0_s v_2. The lower panels of figure 5.10 show the ratios of the scaled v_2 of each species to the fit. Above $p_T/n_q > 1.0$ GeV/c (or $K_t/n_q > 0.5$ GeV/c^2) the scaled $\pi^{\pm}$ v_2 and K^0_s v_2 are compatible within uncertainties, while Λ v_2 is systematically below K^0_s v_2 by about 20% showing little variation with transverse momentum. The v_2 of protons is also smaller than that of K^0_s, but the difference is not so large.

The situation is similar for all other centrality classes. Figure 5.11 shows the ratio of the scaled $v_2\{2, 0.9\}$ and $v_2\{4\}$ to their respective fit as a function of

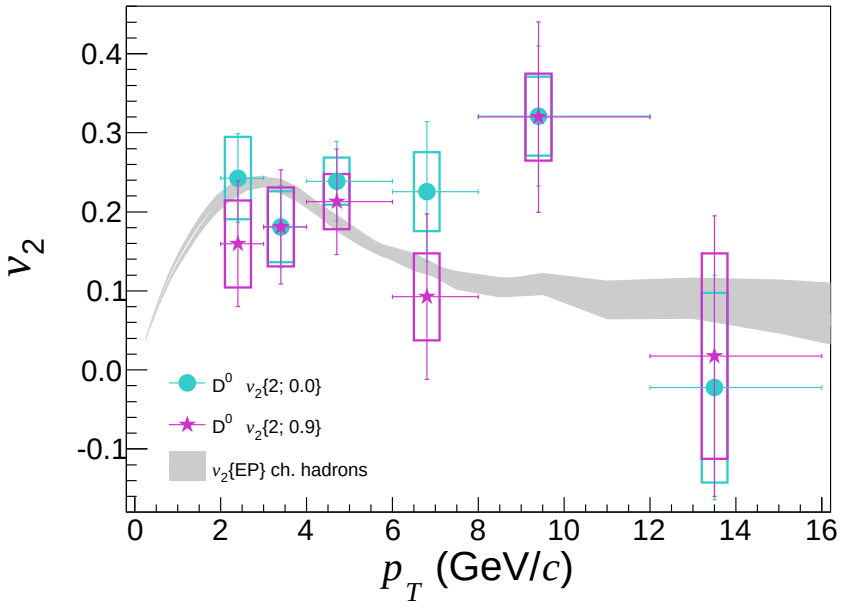

Figure 5.13 D^0 $v_2\{2\}$ and $v_2\{2, 0.9\}$ as a function of transverse momentum compared to charged hadrons.

scaled transverse momentum for several centrality classes. The ratios found for $v_2\{4\}$ are essentially the same as the respective ones for $v_2\{2, 0.9\}$. The ratios show a weak dependence on transverse momentum which becomes more evident in centrality class 20-40% reaching a maximum between 1.0 and 1.5 GeV/c of scaled transverse momentum. The relative difference between the scaled K^0_s v_2 and Λ v_2 is smaller than that found for the most central class. Effects from the hydrodynamical mass scaling are suppressed by using the scaled transverse kinetic energy as shown in figure 5.12.

5.6 D^0 DIFFERENTIAL V_2

Figure 5.13 shows the v_2 for D^0 mesons measured using two particle correlations with and without a $\Delta\eta > 0.9$ gap. The size of the azimuthal anisotropy found is remarkably high and comparable with that of charged hadrons. Such large anisotropy suggests that the charm quark loses so much energy in the medium that it is ultimately affected by collective effects either participating directly to the collective motion or acquiring an effective v_2 via hadronisation.

In contrast to light quarks that can be produced during the entire evolution of the medium, charm quarks are produced predominantly in initial hard

scattering processes and their annihilation rate is expected to be small [89]. Thus they experience the whole evolution of the system.

Several models for the transport of heavy quarks in the medium have computed the amount of v_2 expected at LHC energies. Almost all of them reproduced the anisotropy found at high p_T. At these ranges, the models use perturbative QCD to describe the path-dependence energy loss in the asymmetric fireball. However, at low p_T, these models have different strategies to describe the coupling of charm to the medium and many of them also describe the data quite well.

In figure 5.14 the D^0 v_2 is compared to the calculations of seven different models. These models have adopted distinct ways to describe the evolution of the medium, the transport of heavy quarks in it and the hadronisation mechanism at chemical freeze-out. Some of them include a description of the hadronic gas phase as well. All of them have reproduced quite well the R_{AA} and v_2 of heavy flavour electrons at RHIC energies.

The *WHDG model* [90–92] uses a perturbative QCD (pQCD) calculation of parton energy loss, including both radiative (DGLV [93]) and collisional processes. A realistic collision geometry based on the Glauber model is used for the initial state. WHDG does not describe the hydrodynamical expansion of the medium, i.e. the predicted anisotropy results only from path-length-dependent energy loss. Hadronisation is performed using fragmentation functions. The medium density is constrained on the basis of the π^0 RAA in central collisions at RHIC top energy and scaled to LHC energy according to the increase of the charged particle multiplicity. The model gives an almost constant $v_2 \sim 0.06$, which seems much smaller than the measured values in the range $2 < p_T < 6$ GeV/$c$and compatible with the measurements at higher transverse momentum.

The *MCsHQ+EPOS, Coll+Rad(LPM) model* [94] also uses pQCD computations for collisional and radiative energy loss mechanism for heavy quarks with a running strong coupling constant. The radiative energy loss includes the Landau-Pomeranchuk-Migdal correction [95]. The medium fluid dynamical expansion is based on the EPOS model [96, 97]. A component of recombination of heavy quarks with light-flavour quarks from the QGP is also incorporated in the model. This model yields a substantial anisotropy ($v_2 \sim$ 0.12 at low p_T and 0.08 at high p_T), which is close to that observed in data.

The *TAMU-elastic model* [98] is a heavy-flavour transport model based on elastic processes only. The heavy-quark transport coefficient is calculated within a non-perturbative approach, where the interactions proceed via resonance formation that transfers momentum from heavy quarks to the medium

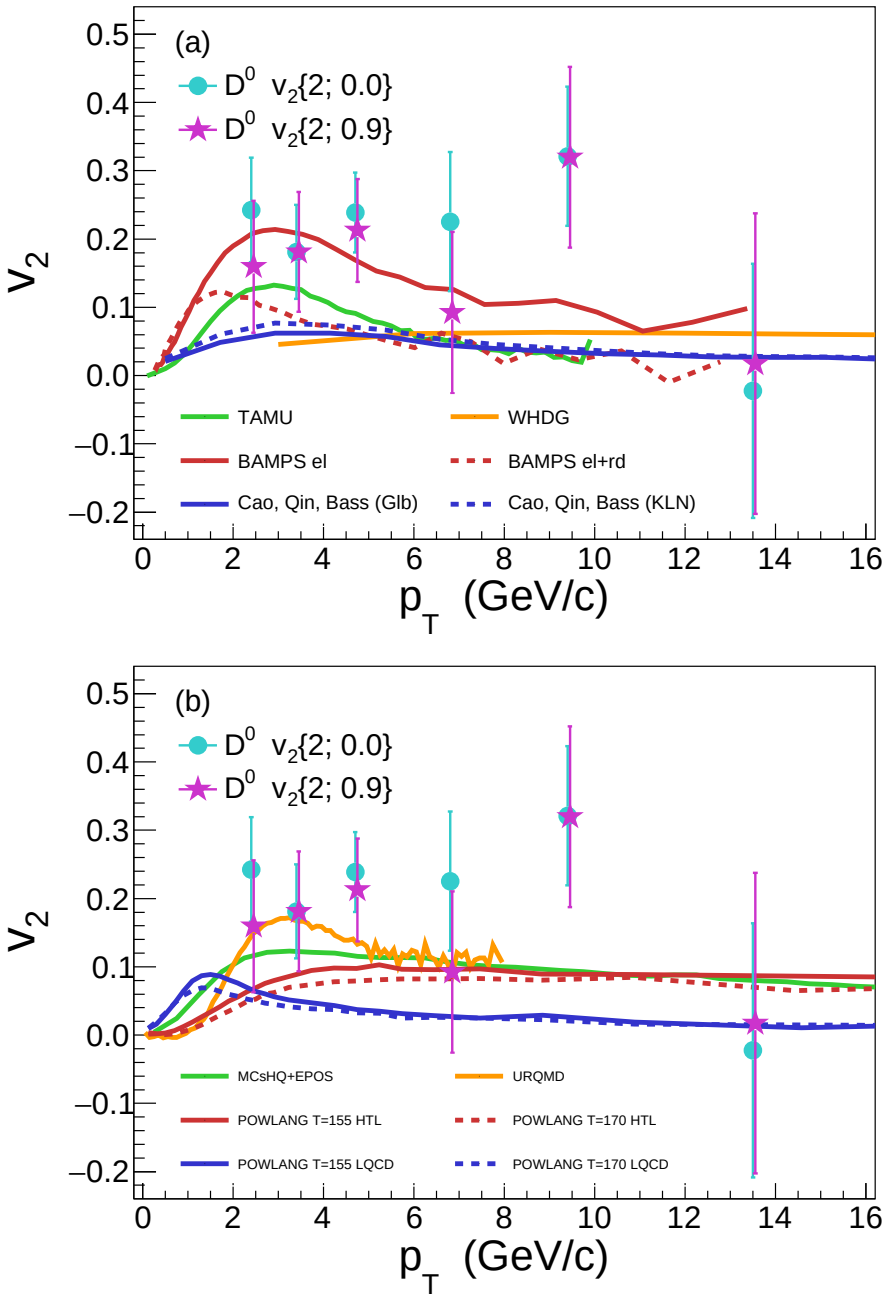

Figure 5.14 $v_2\{2\}$ and $v_2\{2,0.9\}$ of D^0 particles as function of p_T compared to calculations from several models. See text for details.

constituents. The model includes hydrodynamic medium evolution, constrained by light-flavour hadron spectra and elliptic flow data, and a component of recombination of heavy quarks with light-flavour quarks from the QGP. Diffusion of heavy-flavour hadrons in the hadronic phase is also included. The maximum anisotropy, v_2 of about 0.13 at $2 < p_{\mathrm{T}} < 4$ GeV/c, is close to that observed in the data. Towards larger transverse momentum, the model tends to underestimate v_2.

The *POWLANG model* [99, 100] is based on collisional processes treated within the framework of Langevin dynamics in an expanding deconfined medium described by relativistic viscous hydrodynamics. The transport coefficients entering into the relativistic Langevin equation are evaluated by matching the hard-thermal-loop calculation of soft collisions with a perturbative QCD calculation for hard scatterings. Hadronisation is implemented via fragmentation functions. The freeze out temperature was varied from 155 MeV to 175 MeV. The later produced a reduced v_2 at low p_{T} suggesting that the v_2 develops strongly in the deconfined phase.

The *BAMPS model* [101–103] is a partonic transport model based on the Boltzmann approach to multiparton scattering. Heavy quarks interact with the medium via collisional processes computed using a running value of the strong-coupling constant. Hadronisation is performed using fragmentation functions. The lack of radiative processes is accounted for by scaling the binary cross section with a correction factor, which is tuned to describe the heavy-flavour decay electron elliptic flow and nuclear modification factor at top RHIC energies. When applied to calculations for LHC energy, this correction factor results in an underestimation of the D-meson RAA for $p_{\mathrm{T}} > 5$ GeV/c and a large azimuthal anisotropy, with v_2 values up to 0.20, similar to those observed in the data.

A Langevin approach for the transport of heavy quarks is implemented in the *UrQMD model* [82, 83, 104, 105]. This model includes a realistic description of the medium evolution by combining hadronic transport and ideal hydrodynamics. The transport of heavy quarks is calculated on the basis of a resonance model with a decoupling temperature of 130 MeV. Hadronisation occurs via quark coalescence. The calculation parameters are tuned to reproduce the heavy-flavour measurements at top RHIC energies and are kept unchanged for calculations at LHC energies. The model describes very well the measured D^0 v_2.

The *Cao, Qin, Bass model* [106] is also based on the Langevin approach. In addition to quasielastic scatterings, radiative energy loss is incorporated by treating gluon radiation as an additional force term. The space-time evolution of the medium is modelled using a viscous hydrodynamic simulation. The

Model	QGP	Elastic	Radiative	Hadron.	HGP
WHDG	–	pQCD	DGLV	Frag.	no
MCsHQ+EPOS	EPOS	pQCD	LPM	Rec.	no
TAMU	Hydro	Matrix T	–	Rec.	yes
POWLANG	Hydro	pQCD+HTL	–	Frag.	no
BAMPS	–	Boltzman	–	Frag.	no
UrQMD	Hydro	Langevin	–	Coal.	yes
Cao, Qin, Bass	Hydro	Langevin	yes	Rec.	no

Table 5.1 Comparison of the main features included in the heavy flavour transport models used in figure 5.14. The second column corresponds to the description used for the QGP evolution. The third and fourth columns, to the approach used for the transport of heavy quarks in the medium due to elastic and radiative in-medium energy loss. The fifth is the hadronisation mechanism used. The sixth indicates whether a model for the interaction in the hadronic gas phase was included in the model.

hadronisation of heavy quarks has a contribution based on the recombination mechanism. The curves presented in figure 5.14were obtained with a very recent parametrisation for the nuclear shadowing of the parton distribution functions complementary to the model described in [45], The model, however, underestimates significantly the measured value of v_2.

Table 5.1 summarises the main properties of the models presented here. All models agree quite well in the characterisation of v_2 at high traverse momentum. A flat finite positive v_2 is expected as a result of azimuthally anisotropy energy loss which in data is found to produce a v_2 smaller than 0.1.

At low p_{T}, the models present very different predictions. In general, models which include a hydro-like expansion of the scattering centres (TAMU, POWLANG LQCD) or a hadronisation mechanism based on recombination with light-quarks (MCsHQ) or both (uRQMD) reproduce quite well the measured v_2, while models that lack any of those features underestimate the measurement below $ptmm < 6$ GeV/c. Some models also show little sensitivity to the initial state geometry description by presenting almost no variation between Glauber and KLN initial conditions.

It is particularly interesting to see how the Cao, Quin, Bass model underestimate the measurements and it is more compatible with the results of WHDG, event though the former includes a hydro description and hadronisation by recombination while the latter does not. The reason could be in the inclusion of radiative processes with seem to attenuate the final state anisotropy. The same phenomenon occurs in the BAMPS models when radiative corrections are taken into account.

Another interesting point is raised by the POWLANG model which shows very little sensitivity to the decoupling temperature and a larger one to the non-perturbative QCD approach used.

Summary

6

The azimuthal anisotropic parameter v_2 of K^0_s, Λ and D^0 particles measured in Pb–Pb collisions at $\sqrt{s_{NN}} = 2.76$ TeV were shown.

The D^0 meson v_2 - first measured at ALICE - provides experimental constraints to transport models of heavy quarks. The open charm v_2 measurements present a significantly large v_2 at transverse momentum $2.0 < p_T < 6.0$, most compatible with effects caused by an expanding medium. In this transverse momentum range, models that include heavy flavour transport indicate that the large anisotropy could be accounted for by a mechanism that transfers the properties of the expanding medium to the charm hadrons. Above $p_T > 6$ GeV/c, the azimuthal anisotropy is positive and small, although less significant than in the case of strange hadrons v_2. This effect could originate from a path-length dependence of the partonic energy loss.

For K^0_s and Λ particles - which extends the measurement v_2 for identified particles to a large p_T range, a more precise measurement was obtained using three different ways of measuring v_2. The measured differential v_2 reaches a higher value than at RHIC top energies $\sqrt{s_{NN}} = 200$ GeV, however the $v_2(p_T)$ features are quite similar between both systems. The v_2 for charged hadrons rises with transverse momentum for $p_T < 2$ GeV/c (4 GeV/c for Λ) and then develops a plateau falling off slowly beyond 6 GeV/c. At low p_T (< 1 GeV/c) the dependence of v_2 on particle mass is consistent with hydrodynamic calculations where local thermal equilibrium of partons has been assumed. The VISHNU model predicts quite well the azimuthal anisotropy found in data for most peripheral collisions. The data favour a rather small value of η/s; close to the limit established by the AdS/CFT prediction. On the other hand, the inversion of mass ordering for protons and Λ, expected from VISHNU, was not found in data suggesting that the build-up of v_2 during the hadronic phase in the model has to be revised. At intermediate p_T the differential v_2 for K^0_s particles reaches a saturation plateau much earlier than that for Λ particles. This feature was investigated in the context of number of constituent quark scaling. The results show that quark scaling holds only approximately, working better for mid central collisions.

The relative eccentricity fluctuations based on a Bessel-Gaussian model estimated by both K^0_s and Λ independently are the same to that found for charged hadrons.

The anisotropic coefficient $v_2\{2\}$ of both K^0_s and Λ shows a large suppression when increasing the pseudo-rapidity separation between the charge and neutral strange hadrons. The relative reduction is equal for both particles and slightly centrality dependent. The effect could be attributed to a reduction of the fluctuations for long range correlations or could even indicate a variation in the flow angle with pseudo-rapidity.

ALICE data sets

A

The run samples used for the present analysis are the following:

2010 data samples
137161, 137162, 137230, 137231, 137232, 137235, 137236, 137243, 137366, 137430, 137431, 137432, 137434, 137439, 137440, 137441, 137443, 137539, 137541, 137544, 137549, 137595, 137608, 137638, 137639, 137685, 137686, 137691, 137692, 137693, 137704, 137718, 137722, 137724, 137751, 137752, 137844, 137848, 138190, 138192, 138197, 138201, 138225, 138275, 138364, 138396, 138438, 138439, 138442, 138469, 138534, 138578, 138582, 138583, 138621, 138624, 138638, 138652, 138653, 138662, 138666, 138730, 138732, 138837, 138870, 138871, 138872, 139028, 139029, 139036, 139037, 139038, 139105, 139107, 139173, 139309, 139310, 139314, 139328, 139329, 139360, 139437, 139438, 139465, 139503, 139505, 139507, 139510

2011 data samples
167915, 167920, 167985, 167987, 167988, 168069, 168076, 168105, 168107, 168108, 168115, 168310, 168311, 168322, 168325, 168341, 168342, 168361, 168362, 168458, 168460, 168464, 168467, 168511, 168512, 168514, 168777, 168826, 168988, 168992, 169035, 169091, 169094, 169138, 169144, 169145, 169148, 169156, 169160, 169167, 169238, 169411, 169415, 169417, 169835, 169837, 169838, 169846, 169855, 169858, 169859, 169923, 170027, 170081, 170155, 170159, 170163, 170193, 170203, 170204, 170228, 170230, 170268, 170269, 170270, 170306, 170308, 170309

Calibration of the VZERO system

B

During the first runs of the 2010 data period, there were changes in the gain of the VZERO cells. This variation was corrected online for the sum of total multiplicity measured by the VZERO detector and used in the offline trigger, but it was not accounted for in the read-out of each specific cells for offline processing. As a consequence the rings of the VZERO detector for this period do not have a uniform response in azimuth. Figure B.1 shows the situation for the 2010 data sample compared to the 2011 data sample. The plot shows an inspection in time of the $\langle Q_2 \rangle$ components in x and y computed using RPs from the TPC (displaced by +0.04 for visualisation purposes) and the VZERO detector. A procedure for equalisation of cells within a ring was used before the extraction of the Q vectors from the VZERO.

The procedure requires a previous passage over data in order to store the total multiplicity per cell as function of time and centrality (c). Since the conditions of the VZERO response did not vary within each *run* (r), the time dependence is encoded into a run dependence in order to increase accuracy. There calibration values were stored per VZERO cell "i" as $S_{\mathrm{i}}(r,c)$ and are used in order to weigh the signal of each VZERO cell before the computation of the Q vector. The weight associated to each cell "i" is

$$w_{\mathrm{i}}\,(r,c) = \frac{\sum_{\mathrm{j}} S_{\mathrm{j}}(r,c)}{S_{\mathrm{i}}(r,c)}, \tag{B.1}$$

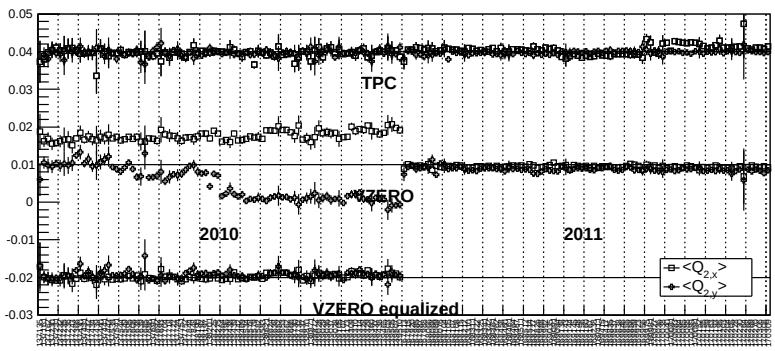

Figure B.1 Distribution of the mean Qy for TPC and VZERO before and after calibration. See text for details.

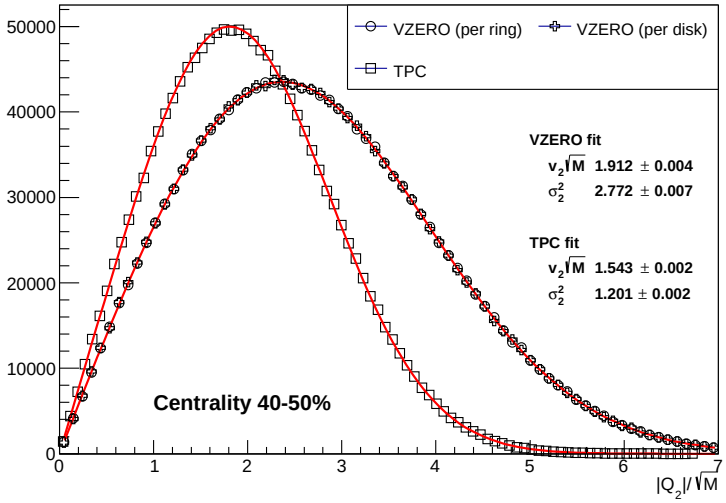

Figure B.2 Distribution of the Q vector normalized by the squared root of the multiplicity M (total signal in the case of VZERO) for events in centrality class 40-50%. See text for details.

where the sum $\sum_j$ runs over a collection of cells which include the cell "i". Two collections were tested: per-ring and per-disk.

Two Q vectors are computed: one for VZERO-A and another for VZERO-C. The difference between them is the relative weight that each ring has in the computation of the Q vector. The equalisation per ring gives weights to each of the four rings according to the total signal registered by that ring, while the equalisation per disk gives equal weight to all the rings. However, for the norm of the Q vector distribution, no significant difference between the two configurations was found.

Once the weights are obtained, the equalised signal of each VZERO cell is computed on-the-fly for each event. The equalised multiplicity of cell "i" is

$$s_i^{eq} \equiv w_i(c,r) * s_i, \tag{B.2}$$

where s_i is the signal originally registered by the VZERO cell "i". Figure B.1 shown the average components of the Q_2 vector computed with the equalised VZERO (displaced by -0.02 for visualisation purposes). As can be seen from this figure the bias in time due to anisotropic response is removed.

Figure B.2 shows the distribution of the $|Q_2| = |Q_2^{VZEA} + Q_2^{VZEC}|$ normalised by the squared root of their total signal for events in centrality class 40–50%, where the elliptic flow is maximal. Both calibration procedures (per

ring and per disk) leave us with the same distribution in the norm of Q. This points to the fact that the relative multiplicity recorded per ring has no effect in measuring the Q vector. The distribution has a Bessel-Gaussian shape as expected from a set sensitive to the flow, see chapter 3. The measurement using *central tracks* is also shown for comparison.

Probability density functions used in this thesis

C

Gauss

$$\mathbf{g}(X;\mu,\sigma) = \frac{1}{\sqrt{2\pi}\sigma}\exp\frac{(X-\mu)^2}{2\sigma^2} \tag{C.1}$$

Cauchy/Lorentz/Breit-Wigner

$$\mathbf{c}(X;\mu,\gamma) = \frac{1}{\pi}\left(\frac{\gamma}{(X-\mu)^2+\gamma^2}\right) \tag{C.2}$$

Voigt

$$\mathbf{v}(X;\gamma,\sigma) = \int_{-\infty}^{+\infty} \mathrm{d}x'\mathbf{c}(X-x';0,\gamma)\mathbf{g}(x';0,\sigma) \tag{C.3}$$

Double-Gauss

$$\mathbf{dg}(X;f,\mu,\sigma_1,\sigma_2) = f\mathbf{g}(X,\mu,\sigma_2) + (1-f)\,\mathbf{g}(X,\mu,\sigma_1) \tag{C.4}$$

Samenvatting

Dit proefschrift betreft de azimutale-anisotropieparameter v_2 voor K^0_s, Λ en D^0 deeltjes gemeten in Pb-Pb-botsingen bij $\sqrt{s_{NN}} = 2.76$ TeV.

De D^0 meson v_2, voor het eerst gemeten bij ALICE, begrenst transportmodellen voor zware quarks. De open charm v_2 meting laat een significante v_2 zien bij transversale impulsen $2.0 < p_T < 6.0$ GeV/c, hetgeen compatibel is met effecten van een expanderend medium. In dit transversale impulsbereik geven modellen die zware quark transport bevatten aan dat de grote anisotropie verklaard zou kunnen worden door een mechanisme dat de beweging van het expanderende medium overdraagt op de hadronen met een charmquark. Voor $p_T > 6$ GeV/c is de azimuthale anisotropie positief en klein en minder significant dan die van hadronen met een strangequark. Dit effect kan ontstaan door een padlengte-afhankelijkheid van het partonisch energieverlies.

Voor K^0_s en Λ deeltjes, waarbij de meting van v_2 voor geïdentificeerde deeltjes tot een groter p_T gebied is uitgebreid, is een nauwkeuriger meting verkregen door gebruik te maken van drie verschillende methoden. De gemeten differentiële v_2 bereikt een hogere waarde dan bij de hoogste RHIC energie $\sqrt{s_{NN}} = 200$ GeV, terwijl vorm van de $v_2(p_T)$ curve vrijwel gelijk is voor de twee systemen. De v_2 voor geladen hadronen stijgt voor transversale impulsen $p_T < 2$ GeV/c, bereikt een plateau en valt langzaam af tot voorbij 6 GeV/c. Bij lage impuls (< 1 GeV/c), is de afhankelijkheid van v_2 van de massa van de deeltjes consistent met hydrodynamica waarbij lokaal thermisch evenwicht van de partonen is aangenomen. Het VISHNU model voorspelt de azimuthale anisotropie gevonden in perifere botsingen redelijk goed. De data laten een voorkeur zien voor tamelijk kleine waarden van η/s; dicht bij de limiet die door Ads/CFT wordt voorspeld. Anderzijds wordt de omgekeerde massa-rangschikking, verwacht door VISHNU, niet gezien in de data, hetgeen suggereert dat de opbouw van v_2 gedurende de hadronische fase in dit model aangepast moet worden. Bij intermediaire p_T bereikt de differentiële v_2 voor K^0_s deeltjes veel vroeger een plateau dan voor Λ deeltjes. Dit fenomeen is onderzocht in het kader van het 'constituent quark scaling' model. De resultaten laten zien dat 'constituent quark scaling' slechts bij benadering werkt, het best bij niet-centrale botsingen.

De relatieve excentriciteitsfluctuaties gebaseerd op een Bessel-Gaus model, onafhankelijk geschat voor K^0_S en Λ, zijn gelijk aan die van geladen hadronen.

De anisotropiecoëfficient v_2 van zowel K^0_S als Λ wordt veel kleiner wanneer het rapiditeitinterval tussen de geladen deeltjes waarmee het reactievlak bepaalt wordt, en de neutrale vreemde hadronen, wordt vergroot. De reductie is hetzelfde voor beide deeltjes en hangt slechts zwak af van de centraliteit. Dit effect kan toegeschreven worden aan de vermindering van de fluctuaties of de lange-afstandcorrelaties of zou zelfs het gevolg kunnen zijn van verandering van de 'flow' hoek als functie van de rapiditeit.

References

[1] Gunther Dissertori et al. *Quantum Chromodynamics*. Oxford Science Publications, 2010 (cit. on p. 1).

[2] F. Halzen et al. *Quarks and Gluons: An Introductory Course in Modern Particle Physics*. Wiley, 1984 (cit. on p. 1).

[3] Particle Data Group. "The review of particle physics". In: *Physics Review D* 86 (2012), p. 010001 (cit. on pp. 2, 17, 41).

[4] C.T.H. Davies et al. "Update on Quarkonium Spectroscopy and α_{strong} from NRQCD". In: *Nucl. Phys. Proc. Suppl.* 47 (1996), pp. 409–416 (cit. on p. 2).

[5] A.X. El-Khadra. "XXXIst Recontres de Moriond". In: *arXiv: hep-ph/9608220* (1996) (cit. on p. 2).

[6] The CBM Collaboration. "Compress Baryonic Matter (CBM) Experiment at FAIR". In: *http://www.fair-center.eu/for-users/experiments/cbm/* (2014) (cit. on p. 3).

[7] E.M. Burbidge et al. "Synthesis of the Elements in Stars". In: *Review of Modern Physics* 29 (1957), p. 547 (cit. on p. 3).

[8] S.A. Bass et al. "Signatures of Quark-Gluon-Plasma formation in high energy heavy-ion collisions: A Critical review". In: *Journal of Physics G: Nuclear and Particle Physics* 25 (1999), pp. 1–57 (cit. on p. 4).

[9] Helmut Satz. "Colour Deconfinement in Nuclear Collisions". In: *Rept. Prog. Phys.* 63 (2000), p. 1511 (cit. on p. 4).

[10] The CMS collaboration. "Measurement of the elliptic anisotropy of charged particles produced in PbPb collisions at nucleon-nucleon center-of-mass energy = 2.76 TeV". In: *Physical Review C* 87 (2013), p. 014902 (cit. on p. 6).

[11] Sergei A. Voloshin. "Transverse radial expansion and directed flow". In: *Physical Review C* 55.4 (1996), R1630 (cit. on pp. 7, 61, 63).

[12] Jean-Yves Ollitrault. "Anisotropy as a signature of transverse collective flow". In: *Physical Review D* 46 (1 1992), pp. 229–245 (cit. on p. 7).

[13] "Quark Matter XXIV". In: *Procceddings*. 2014 (cit. on p. 7).

[14] Nicolas Borghini et al. "Flow analysis from multiparticle azimuthal correlations". In: *Physical Review C* 64 (5 2001), p. 054901 (cit. on pp. 8, 28, 30).

[15] The STAR Collaboration. "Charged and strange hadron elliptic flow in Cu+Cu collisions at 62.4 and 200 GeV". In: *Physical Review C* 81 (2010), p. 044902 (cit. on pp. 8, 27, 58).

[16] M. Kurosawa. "Higher harmonics flow measurement of charged hadrons and electrons in wide kinematic range with PHENIX VTX tracker". In: *Nuclear Physics A* 904-905.1-1092 (2013) (cit. on p. 9).

[17] The ALICE Collaboration. "The ALICE experiment at the CERN LHC". In: *Journal of Instrumentation* 3 (2008), S08002 (cit. on p. 13).

[18] The ALICE Collaboration. "Technical design report of the Trigger, Data Acquisition, High-Level Trigger and Contol System". In: *CERN/LHC 2003-062* (2004) (cit. on pp. 14, 23).

[19] Claus Grupen. *Particle Detectors*. Cambridge University Press, 2008 (cit. on p. 14).

[20] The ALICE Collaboration. "Technical Design Report of the Inner Tracking System". In: *CERN/LHC 99-12* (1999) (cit. on p. 14).

[21] The ALICE Collaboration. "Technical Design Report of the Time Projection Chamber". In: *CERN/LHC 2000-001* (2000) (cit. on pp. 16, 17, 36).

[22] The ALICE Collaboration. "ALICE: Physics Performance Report, Volume II". In: *Journal of Physics G: Nuclear and Particle Physics* 32 (2006), p. 1295 (cit. on pp. 16, 25, 36).

[23] The ALICE Collaboration. "ALICE: Physics Performance Report, Volume I". In: *Journal of Physics G: Nuclear and Particle Physics* 30 (2004), p. 1517 (cit. on p. 16).

[24] The ALICE Collaboration. "Technical Design Report of the Time Of Flight System". In: *CERN/LHC 2002-016* (2002) (cit. on p. 18).

[25] The ALICE Collaboration. "Technical Design Report of the Forward Detectors". In: *CERN/LHC 2004-025* (2004) (cit. on p. 18).

[26] B. Abelev et al. "Elliptic flow of identified hadrons in Pb-Pb collisions at $\sqrt{s_{NN}}$ = 2.76 TeV". In: *Journal of High Energy Physics* 2015.6, 190 (2015) (cit. on pp. 22, 58, 64–68, 71).

[27] C. E. Perez Lara. "ALICE Physics Week in Jyvaskyla 2011: D meson v2 in Pb-Pb with 2- and multi-particle methods". In: 2011 (cit. on p. 22).

[28] The ALICE Collaboration. "Centrality determination of Pb-Pb collisions at 2.76 TeV with ALICE". In: *Physical Review C* 88 (2013), p. 044909 (cit. on p. 23).

[29] J.-Y. Ollitrault. "Collective flow from azimuthal correlations". In: *Nuclear Physics A* 590 (1995), pp. 561 –564. ISSN: 0375-9474 (cit. on p. 23).

[30] Arthur M. Poskanzer et al. "Methods for analyzing anisotropic flow in relativistic nuclear collisions". In: *Physical Review C* 58 (1998), pp. 1671–1678 (cit. on p. 23).

[31] P. Danielewicz et al. "Transverse momentum analysis of collective motion in relativistic nuclear collisions". In: *Physics Letters B* 157 (1985), pp. 146 –150. ISSN: 0370-2693 (cit. on p. 23).

[32] Karl Pearson. "The problem of the random walk". In: *Nature* 72 (1905), pp. 294, 302 (cit. on p. 24).

[33] Sergei A. Voloshin et al. *Relativistic Heavy Ion Physics*. Vol. 23. Landolt-Bornstein. Springer-Verlag, 2008, pp. 5–54 (cit. on p. 24).

[34] The PHENIX Collaboration. "Azimuthal anisotropy of π^0 and η mmeson in Au+Au collisions at 200 GeV". In: *Physical Review C* 88 (2013), p. 064910 (cit. on pp. 27, 58).

[35] The PHENIX Collaboration. "Observation of diret-photon collective flow in Au+Au collisions at 200 GeV". In: *Physical Review Letters* 109 (2012), p. 122302 (cit. on pp. 27, 58).

[36] S. Afanasiev et al. "Elliptic Flow for ϕ Mesons and (Anti)deuterons in Au + Au Collisions at $\sqrt{s_{NN}} = 200$ GeV". In: *Phys. Rev. Lett.* 99 (5 2007), p. 052301 (cit. on pp. 27, 58).

[37] A. Adare et al. "Scaling Properties of Azimuthal Anisotropy in Au + Au and Cu + Cu Collisions at $\sqrt{s_{\mathrm{NN}}} = 200$ GeV". In: *Phys. Rev. Lett.* 98 (16 2007), p. 162301 (cit. on pp. 27, 58, 70).

[38] The PHENIX Collaboration. "Mearements of identified π^0 and inclusive photon second-harmonic parameter v_2 and implications for direct photon production in 200 GeV Au+Au". In: *Physical Review Letters* 96 (2006), p. 032302 (cit. on pp. 27, 58).

[39] The STAR Collaboration. "Elliptic flow of identified hadrons in Au+Au collisions at 7.7 – 62.4 GeV". In: *Physical Review C* 88 (2013), p. 014902 (cit. on pp. 27, 58).

[40] The STAR Collaboration. "Observation of an energy-dependent difference in elliptic flow between particles and antiparticles in relativistic heavy ion collisions". In: *Physical Review Letters* 110 (2013), p. 142301 (cit. on pp. 27, 58).

[41] The STAR Collaboration. "Centrality dependence of charged hadron and strange hadron elliptic flow from 200 GeV Au+Au collisions". In: *Physical Review C* 77 (2008), p. 054901 (cit. on pp. 27, 58, 70).

[42] The STAR Collaboration. "Partonic flow and ϕ meson production in Au+Au collisions at 200 GeV". In: *Physical Review Letters* 99 (2007), p. 112301 (cit. on pp. 27, 58).

[43] B. I. Abelev et al. "Mass, quark-number, and $\sqrt{s_{NN}}$ dependence of the second and fourth flow harmonics in ultrarelativistic nucleus-nucleus collisions". In: *Phys. Rev. C* 75 (5 2007), p. 054906 (cit. on pp. 27, 58).

[44] The STAR Collaboration. "Multistrange baryon elliptic flow in Au+Au collisions at 200 GeV". In: *Physical Review Letters* 95 (2005), p. 122301 (cit. on pp. 27, 58).

[45] J. Adams et al. "Azimuthal anisotropy in Au+Au collisions at $\sqrt{s_{NN}} =$ 200 GeV". In: *Phys. Rev. C* 72 (1 2005), p. 014904 (cit. on pp. 27, 58).

[46] J. Adams et al. "Particle-Type Dependence of Azimuthal Anisotropy and Nuclear Modification of Particle Production in Au + Au Collisions at $\sqrt{s_{NN}} = 200$ GeV". In: *Phys. Rev. Lett.* 92 (5 2004), p. 052302 (cit. on pp. 27, 58, 69–71).

[47] Matthew Luzum et al. "Eliminating experimental bias in anisotropic-flow measurements of high-energy nuclear collisions". In: *Physical Review C* 87 (4 2013), p. 044907 (cit. on pp. 27, 28, 30).

[48] The PHENIX Collaboration. "Measurements of high order flow hharmonic in Au+Au collisions at 200 GeV". In: *Physical Review Letters* 107 (2011), p. 252301 (cit. on p. 27).

[49] The ALICE collaboration. "Elliptic flow of charged particles in Pb-Pb collisions at 2.76 TeV". In: *Physical Review Letters* 105 (25 2010), p. 252302 (cit. on pp. 27, 32, 58).

[50] Nicolas Borghini et al. "New method for measuring azimuthal distributions in nucleus-nucleus collisions". In: *Physical Review C* 63 (2001), p. 054906 (cit. on pp. 27–30).

[51] Ante Bilandzic et al. "Event-plane flow analysis without non-flow effects". In: *Physical Review C* 83 (2011), p. 014909 (cit. on p. 28).

[52] Ante Bilandzic. "Flow with Q-cumulants". PhD thesis. Utrecht University, 2011 (cit. on pp. 28, 30, 31, 33).

[53] Ante Bilandzic et al. "Flow analysis with cumulants: Direct calculations". In: *Physical Review C* 83 (2011), p. 044913 (cit. on p. 30).

[54] Sergei A. Voloshing et al. "Elliptic flow in the gaussian model of eccentricity fluctuations". In: *Physics Letters B* 659 (2008), pp. 537–541 (cit. on p. 31).

[55] J Podolanski et al. "Analysis of V-events". In: *Philosophical Magazine Series 7* 45 (1954), p. 13 (cit. on p. 38).

[56] *HIJING Monte Carlo Model* (cit. on p. 41).

[57] *Geant*. URL: `http://geant4.cern.ch/` (cit. on p. 41).

[58] The ALICE collaboration. "Multi-strange baryon production at mid-rapidity in Pb–Pb collisions at $\sqrt{s_{NN}} = 2.76$ TeV". In: *Physics Letters B* 728 (2014), pp. 216–227 (cit. on p. 53).

[59] The ALICE collaboration. "Centrality dependence of π, K, and p production in Pb–Pb collisions at $\sqrt{S_{NN}} = 2.76$ TeV". In: *Physical Review C* 88 (2013), p. 044910 (cit. on p. 53).

[60] The ALICE collaboration. "K^0_s and Λ Production in Pb–Pb Collisions at $\sqrt{S_{NN}} = 2.76$ TeV". In: *Physical Review Letters* 111 (2013), p. 222301 (cit. on p. 53).

[61] David J. Lange. "The EvtGen particle decay simulation package". In: *Nuclear Instruments and Methods in Physics Research Section A: Accelerators, Spectrometers, Detectors and Associated Equipment* 462 (2001), pp. 152 –155 (cit. on p. 55).

[62] The ALICE Collaboration. "Anisotropic flow of charged hadrons, pions and (anti-)protons measured at high transverse momentum in Pb–Pb collisions at LHC". In: *Physics Letters B* 719.1â"3 (2013), pp. 18 –28. ISSN: 0370-2693 (cit. on pp. 58, 62, 63).

[63] S. S. Adler et al. "Elliptic Flow of Identified Hadrons in Au + Au Collisions at $\sqrt{s_{NN}} = 200$ GeV". In: *Phys. Rev. Lett.* 91 (18 2003), p. 182301 (cit. on p. 58).

[64] The PHENIX Collaboration. "Azimuthal anisotropy of PIo production in Au+Au collisions at 200 GeV". In: *Physical Review Letters* 105 (2010), p. 142301 (cit. on p. 58).

[65] A. Adare et al. "Deviation from quark number scaling of the anisotropy parameter v_2 of pions, kaons, and protons in Au + Au collisions at $\sqrt{s_{NN}} = 200$ GeV". In: *Phys. Rev. C* 85 (6 2012), p. 064914 (cit. on p. 58).

[66] Ulrich Heinz et al. "Collective Flow and Viscosity in Relativistic Heavy-Ion Collisions". In: *Annual Review of Nuclear and Particle Science* 63.1 (2013), pp. 123–151 (cit. on p. 61).

[67] Miklos Gyulassy et al. "New forms of QCD matter discovered at RHIC". In: *Nucl.Phys.* A750 (2005), pp. 30–63 (cit. on p. 63).

[68] Edward V. Shuryak. "What RHIC experiments and theory tell us about properties of quark-gluon plasma?" In: *Nucl.Phys.* A750 (2005), pp. 64–83 (cit. on p. 63).

[69] Huichao Song et al. "200 A GeV Au+Au collisions serve a nearly perfect quark-gluon liquid". In: *Physical Review Letters* 106 (2011), p. 192301 (cit. on p. 63).

[70] Huichao Song et al. "Hadron spectra and elliptic flow for 200 A GeV Au+Au collisions from viscous hydrodynamics coupled to a Boltzmann cascade". In: *Physical Review C* 83 (2011), p. 054910 (cit. on p. 63).

[71] G Policastro et al. In: *Physical Review Letters* 87 (2005), p. 081601 (cit. on p. 63).

[72] P.K. Kovtun et al. In: *Physical Review Letters* 94 (2005), p. 111601 (cit. on p. 63).

[73] Huichao Song et al. "Elliptic flow in 200 GeV Au+Au collisions and 2.76 TeV Pb+Pb collisions¿ Insights from viscous hydrodznamics + hadron cascade hybrid model". In: *Physical Review C* 83 (2011), p. 054912 (cit. on pp. 63, 64).

[74] Huichao Song et al. "Causal viscous hydrodynamics in 2+1 dimensions for relativistic heavy-ion collisions". In: *Physical Review C* 77 (2008), p. 064901 (cit. on pp. 63, 64).

[75] W. Israel et al. "Transient relativistic thermodynamics and kinetic theory". In: *Annals of Physics* 118 (1979), p. 341 (cit. on p. 63).

[76] Pasi Huovinen et al. "QCD equation of state and hadron resonance gas". In: *Nuclear Physics A* 837.1-2 (2010), pp. 26–53 (cit. on p. 64).

[77] A. Bazavov et al. "Equation of state and QCD transition at finite temperature". In: *Physical Review D* 80.1 (2009), p. 014504 (cit. on p. 64).

[78] Huichao Song et al. In: *Physical Review C* 87 (2013), p. 019902 (cit. on p. 64).

[79] Huichao Song et al. "Spectra and elliptic flow for identified hadrons in 2.76 A TeV Pb-Pb collisions". In: *Physical Review C* 89 (2014), p. 034919 (cit. on p. 64).

[80] Derek Teaney. "Effect of shear viscosity on spectra, elliptic flow, and Hanbury Brown–Twiss radii". In: *Physical Review C* 68 (2003), p. 034913 (cit. on p. 64).

[81] Drescher H.J. et al. "Effect of fluctuation on the initial exxentricity from the Color Glass Condensate in heavy ion collisions". In: *Physical Review C* 75 (2007), p. 034905 (cit. on p. 64).

[82] S.A. Bass et al. "Microscopic models for ultrarelativistic heavy ion collisions". In: *Prog.Part.Nucl.Phys.* 41 (1998), pp. 255–369 (cit. on pp. 64, 75).

[83] M. Bleicher et al. "Relativistic hadron hadron collisions in the ultrarelativistic quantum molecular dynamics model". In: *J.Phys.* G25 (1999), pp. 1859–1896 (cit. on pp. 64, 75).

[84] Huichao Song et al. "Viscous QCD matter in a hydbrid hydrodynamic+Boltzmann approach". In: *Physical Review C* 83 (2011), p. 024912 (cit. on p. 64).

[85] D. Molnar et al. In: *Physical Review Letters* 91 (2003), p. 092301 (cit. on pp. 69, 70).

[86] R.J. Fries et al. In: *Physical Review Letters* 90 (2003), p. 202303 (cit. on p. 69).

[87] C. Hwa Rodolph C.and Yang. In: *Physics Review C* 67 (2003), p. 064902 (cit. on p. 69).

[88] S. S. Adler et al. "Scaling Properties of Proton and Antiproton Production in $\sqrt{s_{NN}} = 200$ GeV Au + Au Collisions". In: *Phys. Rev. Lett.* 91 (17 2003), p. 172301 (cit. on p. 70).

[89] P Braun-Munzinger. "Quarkonium production in ultra-relativistic nuclear collisions: suppression versus enhancement". In: *Journal of Physics G: Nuclear and Particle Physics* 34.8 (2007), S471 (cit. on p. 73).

[90] S Wicks et al. "Elastic, inelastic and path length fluctuations in jet tomography". In: *Nuclear Physics A* 784 (2007), pp. 426–442 (cit. on p. 73).

[91] W.A. Horowitz et al. "The surprising transparent sQGP at LHC". In: *Nuclear Physics A* 872 (2011), pp. 265–285 (cit. on p. 73).

[92] W.A. Horowitz. "Testing pQCD and AdS/CFT energy loss at RHIC and LHC". In: *AIP Proceedings* 1441 (2011), p. 889 (cit. on p. 73).

[93] M. Djorddjevic et al. "Heavy quark radiative energy loss in QCD matter". In: *Nuclear Physics A* 733 (2004), pp. 265–298 (cit. on p. 73).

[94] M. Nehrgang et al. "Influence of hadronic bound states above T_c on heavy-quark observables in Pb + Pb collisions at the CERN Large Hadron Collider". In: *Physical Review C* 89 (2014), p. 014905 (cit. on p. 73).

[95] R. Baier et al. "Energy loss in perturbative QCD". In: *Annual Review of Nuclear and Particle Sience* 50 (2000), pp. 37–69 (cit. on p. 73).

[96] K. Werner et al. "Event-by-event simulation of the three-dimensional hydrodynamic evolution from flux tube initial conditions in ultrarelativistic heavy ion collisions". In: *Physical Review C* 82 (2010), p. 044904 (cit. on p. 73).

[97] W. Werner et al. "Jets, bulk matter and their interaction in heavy ion collisions at several TeV". In: *Physical Review C* 85 (2012), p. 064907 (cit. on p. 73).

[98] M. He et al. "Heavy Flavour at the Large Hadron Collider in a Strong Coupling Approach". In: *Physics Letters B* 735 (2014), pp. 445–450 (cit. on p. 73).

[99] M Monteno et al. "Heavy Flavor dynamics in nucleus-nucleus collisions: from RHIC to the LHC". In: *Journal of Physics G: Nuclear and Particle Physics* 38 (2011), p. 114144 (cit. on p. 75).

[100] W.M. Alberico et al. "Heavy-flavour spectra in high-energy nucleus-nucleus collisions". In: *The European Physical Journal C* 71 (2011), p. 1666 (cit. on p. 75).

[101] J. Uphoff et al. "Elliptic flow and energy loss of heavy quarks in ultrarelativistic heavy ion collisions". In: *Physical Review C* 84 (2011), p. 024908 (cit. on p. 75).

[102] O. Fochler et al. "Jet quenching and elliptic flow at the RHIC and the LHC within a pQCD-based partonic transport model". In: *Journal of Physics G: Nuclear and Particle Physics* 38 (2011), p. 124152 (cit. on p. 75).

[103] J. Uphoff et al. "Open heavy flavor in Pb + Pb collisions at $\sqrt{s} = 2.76$ TeV within a transport model". In: *Physics Letters B* 717 (2012), pp. 430–435 (cit. on p. 75).

[104] Thomas Lang et al. "Heavy quark transport in heavy ion collisions at RHIC and LHC within the UrQMD transport model". In: *arXiv:1211.6912* (2012) (cit. on p. 75).

[105] Thomas Lang et al. "Heavy quark transport at RHIC and LHC". In: *Journal of Physics: Conference Series* 426 (2013), p. 012032 (cit. on p. 75).

[106] Shenshan Cao et al. “Heavy-quark dynamics and hadronization in ultrarelativistic heavy-ion collisions: Collisional versus radiative energy loss”. In: *Physical Review C* 88 (2013), p. 044907 (cit. on p. 75).